SHOCK DETACHMENT PROCESS ON CONES IN HYPERVELOCITY FLOWS

Thesis by

Ivett A. Leyva

In Partial Fulfillment of the Requirements

for the Degree of

Doctor of Philosophy

California Institute of Technology

Pasadena, California

1999

(Submitted May 28, 1999)

Acknowledgements

First and foremost I would like to thank my advisor, Prof. Hans Hornung, for taking me as his student. He has always been available to answer my questions, teach me experimental and theoretical fluid mechanics, and help me on a personal level as well.

My thanks also go to past and current T5 members without whom this project would not have been possible. They are Philippe Adam, Jean-Paul Davis, Patrick Lemieux, Adam Rasheed, and Bahram Valiferdowsi. I am also indebted to the machine shop staff who built my original models and patiently re-machined them numerous times.

I would also like to thank the members of my committee, Profs. Fred Culick, Dan Meiron, Joe Sheperd, and Brad Sturtevant who read over my thesis.

Special thanks go to Joe Olejniczak from NASA Ames who provided the nonequilibrium numerical code and endless assistance.

Finally I would like to thank my mother for her unconditional love and Antonio for sharing this period of our lives.

Abstract

The shock detachment process on cones in hypervelocity flows is one of the most sensitive flows to relaxation effects. The critical angle for shock detachment under frozen conditions can be very different from the critical angle under chemical and thermal equilibrium. The rate of increase of the detachment distance with cone angle is also affected by the relaxation rate.

The purpose of this study is to explain the effects of nonequilibrium on the shock detachment distance and its growth rate on cones in hypervelocity flows. The study consists of an experimental and a computational program. The experimental part has been carried out at Caltech's hypervelocity reflected shock tunnel (T5). Six different free-stream conditions have been chosen, four using N_2 as the test gas and two using CO_2. About 170 shots were performed on 24 cones. The cones range in diameter from 2 cm to 16 cm with half-angles varying from 55° to 75°. The experimental data obtained are holographic interferograms of every shot, and surface temperature and pressure measurements for the bigger cones. Extensive numerical simulations were made for the N_2 flows and some were also made for the CO_2 flows. The code employed is a Navier-Stokes solver that can account for thermal and chemical nonequilibrium in axisymmetric flows.

The experimental and computational data obtained for the shock detachment distance confirms a previous theoretical model that predicts the detachment distance will grow more slowly for relaxing flows than for frozen or equilibrium flows. This difference is explained in terms of the behavior of the sonic line inside the shock layer. Different growth rates result when the detachment distance is controlled by the diameter of the cone (frozen and equilibrium cases) than when it is controlled by the extent of the relaxation zone inside the shock layer (nonequilibrium flows). The experimental data are also complemented with computational data to observe the behavior of the detachment distance from the frozen to equilibrium limits for a given cone half-angle and free-stream condition. As deduced by a previous simple scaling argument, the ratio of the detachment distance to the diameter of the cone is constant in the two extremes and rapidly switches from one value to the other for cone diameters of about 2 cm to 16 cm. The experimental interferograms are also compared with numerical ones in terms of the detachment distance, the number of fringes in the shock layer, and the shape of the fringes.

The heat flux traces obtained from the temperature measurements show different behaviors for the attached and detached cases, but these effects can be related to the conditions at the edge of and inside the boundary layer and to the Reynolds number of the flow rather than to nonequilibrium effects. The pressure measurements were insensitive to the degree of nonequilibrium.

Contents

List of Figures

List of Tables

Nomenclature

Roman characters

C	Chapman-Rubesin parameter
c_i	mass fraction of species i
C_f	skin friction coefficient
C_p	pressure coefficient
D_{11}	self-diffusion coefficient
dia	diaphragm
d	cone diameter (m)
e	total specific energy (per unit mass of gas mixture) including kinetic, internal, and chemical energies
e_r	specific internal energy from rotational modes (per unit mass of gas mixture)
e_v	specific internal energy from vibrational modes
e_{vr}	average vibrational energy per particle of species r
g_r	degeneracy of mode r
h	specific enthalpy
h_s°	chemical enthalpy of formation for species s
I	intensity of interferograms
k	thermal conductivity
k_b	backward (recombination) reaction rate
k_f	forward (dissociation) reaction rate
L	length of the cone hypothenuse
l	relaxation length (m)
L	length of interest in a given problem

M third body that assist in a chemical reaction

n refractive index

p_4 diaphragm burst pressure

P_{rs} probability of species r transferring vibrational energy to species s

$\dot{q}_j$ heat flux in j-direction due to conduction of translational and rotational internal energy

$\dot{q}_{v_j}$ heat flux in the j-direction due to conduction of vibrational internal energy

Q_{T-v} source term for internal energy exchange from translational to vibrational modes

Q_{v-v_s} source term for internal energy exchange in vibrational modes between species s and other species

R gas constant for a given species

T translational-rotational temperature

t time

t_{fire} time when laser fires (ms)

u mixture or species mass averaged velocity, typically in x-direction

v mixture or species mass averaged velocity, typically in y-direction

v_s diffusion velocity of species s

w mixture or species mass averaged velocity, typically in z-direction

w_s chemical production rate of species s in kg/m^3·s

X distance along the hypothenuse of the cone

Z_{rs} number of s–r collisions per unit time and volume

Greek characters

α thermal diffusivity; mass fraction of dissociating gas

δ displacement thickness (m)

δ_{ij} Kronecker delta used with index summing notation

Δ detachment distance (m)

η grid-aligned coordinate in the body-normal direction; transformed normal coordinate in boundary-layer theory; temperature exponent in Arrhenius reaction rate expressions

γ ratio of specific heats

θ cone half-angle (degrees)

θ_f critical detachment angle for frozen flow

θ_e critical detachment angle for equilibrium flow

θ_v characteristic temperature for molecular vibration

κ Gladstone-Dale constants

λ wavelength of laser used in interferograms

μ viscosity

ξ grid-aligned coordinate in the streamwise (body-parallel) direction

Ω reaction rate parameter

ρ density of the gas

τ shear stress (Pa); time that it takes the flow over the cone to reach steady conditions

τ_{ij} shear stress tensor for two-dimensional flow

τ_s characteristic time for vibrational relaxation

ϕ streamline deflection (degrees); phase shift between no-flow and flow pictures for interferograms

Subscripts

∞ free-stream conditions

0 stagnation conditions

a average

amb ambient

e equilibrium flow

f frozen flow

i, j directional indices in either Cartesian coordinates or grid coordinates

m index for third-body species in reaction; total number of diatomic species

N north station

n total number of species

r pertaining to rotational internal energy modes; secondary species index

S south station

s species index

v pertaining to vibrational internal energy modes

Acronyms

2R secondary reservoir

CFD computational fluid dynamics

CT compression tube

DT dump tank

GALCIT Graduate Aeronautical Laboratories California Institute of Technology

ST shock tube

TS test section

(This page was intentionally left blank.)

Chapter 1 Introduction

There are at least two ways in which one can justify the study of the shock detachment process in hypervelocity flows over cones. One justification lies in the design of hypersonic vehicles, such as that shown in figure 1.1. One of the first steps in designing such vehicles is to simplify their complex shape into simpler and more basic shapes (see artistic impression shown in figure 1.2) and understand the flow around each of these basic shapes. As shown in the same figure, the cone is one of these fundamental shapes, and so in order to fabricate vehicles that travel at hypervelocity conditions, one needs to have a thorough understanding of the physics of hypervelocity flows over cones. As is well known from basic fluid mechanics, for certain combinations of free-stream conditions and cone half-angles, the shock wave that forms in front of a cone in supersonic flow will detach. One then wants to know if for the planned flight conditions the shocks on any cones in the vehicle will be attached or detached and what to expect in terms of heat loads and forces, in the two cases.

Figure 1.1: Artistic conception of supersonic transport by McDonnell Douglas Aircraft Corp.. Taken from Anderson (1989)

The second justification is that shock detachment in general is a fundamental problem in fluid mechanics. One wants to know when detachment happens, which are the most important parameters governing the detachment process, and how can one predict the detachment distance and the flow properties in the shock layer once the shock is detached. Most of the research done to under-

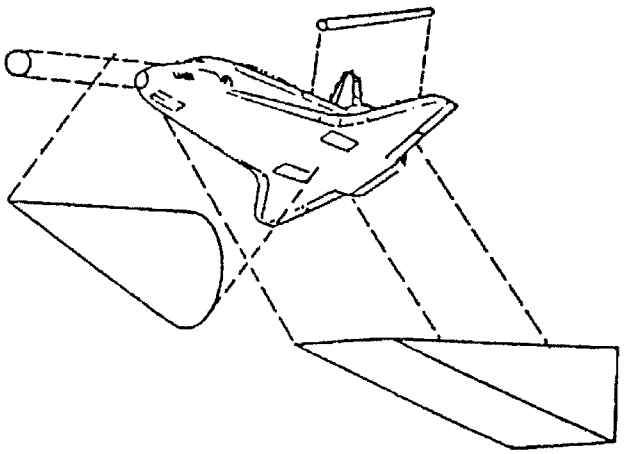

Figure 1.2: Reduction of complex supersonic vehicles to simpler shapes

stand shock detachment has been in the area of perfect-gas flows (here referred to as frozen flows, since chemistry and vibrational nonequilibrium are left out of the problem). However, for certain conditions of practical interest such as vehicles travelling faster than 3 km/s, one has to include vibrational and chemical nonequilibrium. The shock detachment in blunt-body flows has been studied extensively, in frozen as well as hypervelocity conditions (see *e. g.*, Wen (1994)). A lot of research has also been done on the shock detachment process in 2-D flows, *i. e.*, wedge flows. The detachment process in nonequilibrium flows over wedges was studied by Hornung and Smith (1979). For the case of cone flows, the detachment process is more complicated, because the flow properties after the shock are not uniform and some simple scaling arguments that could be used for sphere and wedge flows can not be applied to cone flows. Hornung and Houwing (1980) presented a theoretical and experimental study of hypervelocity flows over cones. The experimental results of this work, however, are not very convincing, because of inadequate resolution of their interferograms. The aim of the work described here is therefore to perform a more complete study of nonequilibrium hypervelocity flow over cones in order to produce conclusive results. To achieve this goal, a much greater range of conditions is covered, the experiments are coupled with a computational investigation, and holographic interferometry is complemented by surface measurements of heat flux and pressure. Both in the previous and present study, all cone flows considered are at zero angle of attack.

1.1 Frozen, nonequilibrium, and equilibrium flows

Since we are going to refer extensively to these three classes of flows throughout this thesis, let's define each class before proceeding any further. For this study, we take the shock to be a boundary of negligible thickness between two states in translational and rotational equilibrium. After crossing the shock, the gas undergoes chemical reactions and vibrational relaxation. For any given streamline, the region of non-equilibrium can be characterized by several relaxation lengths. The chemical relaxation length can be defined as the length, after crossing the shock, up to when the composition of the gas remains constant. The vibrational relaxation length can be defined as the length that it takes for the flow to reach thermal equilibrium, *i.e.* , the translational and any vibrational temperature come to an equal value. Although the relaxation length for each process is generally different, for the purposes of the theoretical considerations we only take one relaxation length that includes both processes. For frozen flows, the relaxation length is bigger than any resolvable length in the problem and for all practical purposes the flow has a "frozen" composition throughout the shock layer. In this case, the vibrational modes are also "frozen" and any vibrational temperature is the same before and after the shock. In nonequilibrium flows, the relaxation length is fully resolvable. In the case of the non-equilibrium numerical calculations to be described later, one can resolve both the chemical and vibrational relaxation lengths along a given streamline. Finally, in the limit of equilibrium flows, the relaxation length is much smaller than any resolvable length in the problem and the flows achieves thermal and chemical equilibrium as it crosses the shock.

1.2 Supersonic, inviscid, frozen flow over a cone

It is convenient to introduce the topic of shock detachment with a comparison of flow over a cone with the more familiar case of wedge flow. It is important to note some fundamental differences between wedge flows (2-D) and cone flows (axisymmetric flow). Consider the case of an attached shock wave in both cases (see figure 1.3). The fist thing one notices is that the shock angle is smaller for the case of cone flow. This is because, for a given cone or wedge half-angle, the shock is weaker in the case of cone flow due to the lateral divergence provided by the third spatial dimension present in conical flows ("three-dimensional relieving effect"). A weaker shock also translates into lower pressure, temperature, and density immediately behind the shock (see Anderson (1990)). One can also see from the figure that in the case of wedge flow, the flow is deflected only once as it crosses the shock wave. After this, the flow direction is constant and parallel to the wedge surface. On the other hand, in the case of a cone, the flow undergoes an initial deflection as it passes through the shock but continues to deflect until the flow direction becomes parallel to the cone surface. This continuous deflection, accompanied by changes in flow properties, makes the flow over a cone

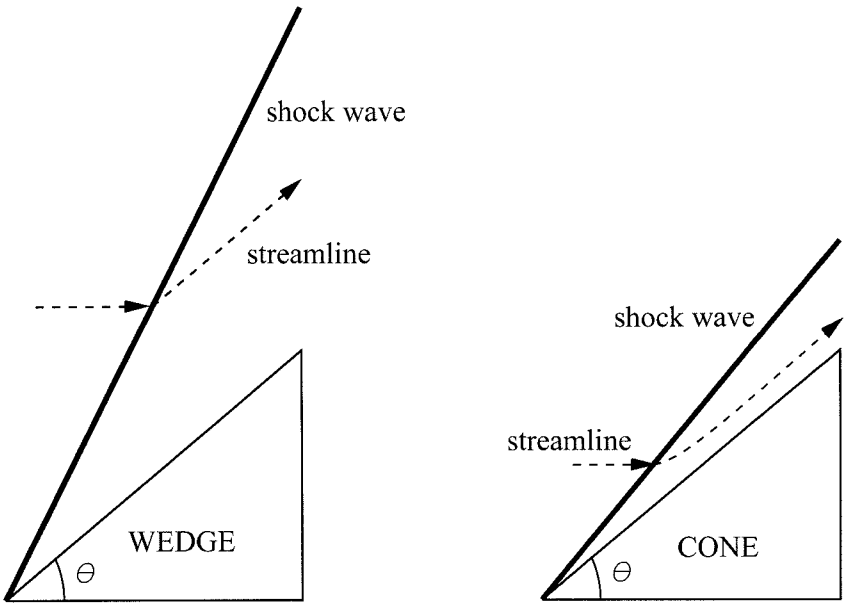

Figure 1.3: Differences in streamline deflection after shock between cone and wedge frozen flows

more complicated than that over a wedge for the same free-stream conditions. Also, for the same free-stream conditions, namely the same M_∞ and γ for frozen flows, the critical angle at which the shock detaches is greater for a cone than for a wedge (see figure 1.4 taken from Anderson (1990)). Another consequence of the "three-dimensional relieving effect" is that for the same half-angle, the critical Mach number at which a shock detaches from a cone is lower than that for a wedge (see figure 1.5 taken from Staff (1948)).

The first study of supersonic flow over a cone is that by Busemann (1929). He studies a semi-infinite cone and assumes conical flow, that is, all flow properties (such as velocity and pressure) are constant along rays that pass through the cone vertex. Since the flow is symmetrical about the x-axis of the cone, the flow properties are actually constant on cones with the same vertex as the original cone (each conical surface having different values). Conical flow results from the absence of a length scale (inviscid perfect-gas flow over a semi-infinite cone). Conical flow solutions are also valid for finite cones as long as the surface Mach number is greater than one. When the flow becomes subsonic inside the shock layer, the size of the cone can be communicated back to the tip and the flow is no longer conical. Busemann's solution is graphically constructed in the hodograph plane (u and v are the independent variables instead of x and y). Important points that can be concluded from his study are, firstly, that conical solutions only exist for attached shocks and secondly that there can be cases for given cone half-angles and free-stream Mach numbers where there can be an isentropic compression from supersonic to subsonic conditions inside the shock layer. This is one of

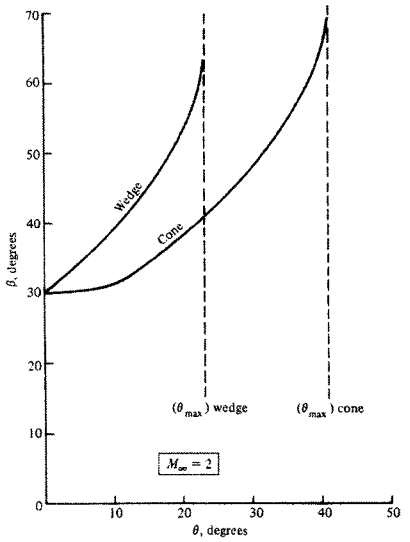

Figure 1.4: Critical detachment angle for cone and wedge flows

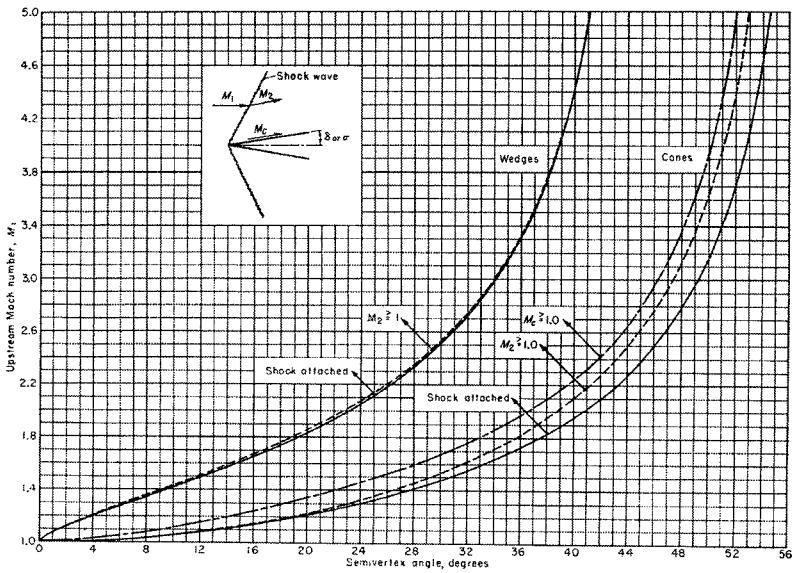

Figure 1.5: Critical angles for detachment in cone and wedge flows for different free-stream Mach numbers and cone/wedge half-angles

the few instances where a shock-free compression from supersonic to subsonic conditions has been experimentally verified (Solomon, 1954) and will be discussed in more detail in sections 2.1 and 5.1.

The solution for the axially symmetric equations of motion for semi-infinite cones can be obtained mathematically. Taylor and Maccoll (1933) and Maccoll (1937) present such numerical solutions as well as experimental results to verify the theory. The conical flow is assumed to be steady, isentropic,

and irrotational after the shock. These solutions permit only straight shocks since curved shocks produce different jumps in entropy at different locations along the shock and this would violate the condition of isentropic flow downstream of the shock. The famous Taylor and Maccoll graphical solutions for frozen attached flow over cones are presented in figure 1.6 taken from Staff (1948). From these curves, one can see that there exists a critical cone half-angle, for a given M_∞ and γ, above which the shock will detach and no more solutions are available. In the lower vicinity of this critical half-angle, the solutions predict a mixed supersonic/subsonic flow in the shock layer. The flow is supersonic after crossing the shock but becomes subsonic close to the surface of the cone. The sonic line in this case is a ray in the flowfield. From figure 1.6 also note that for a given cone half-angle and γ, there is a critical M_∞ below which the shock is detached. Finally, note that even for $M_\infty = \infty$ there is a critical angle after which the shock is always detached. For the case of $\gamma = 1.4$ this critical cone half-angle is $\theta = 57.5°$.

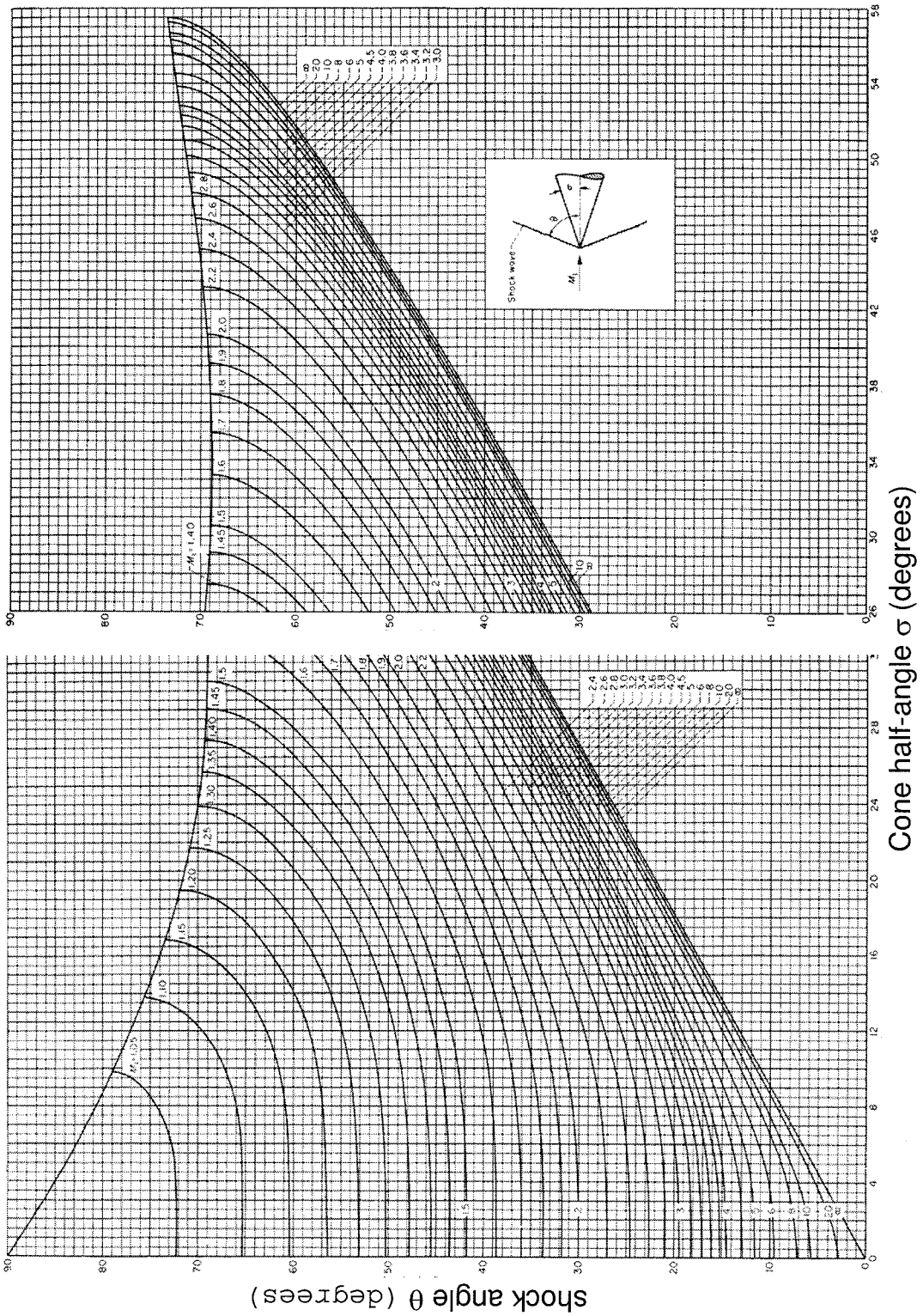

Figure 1.6: Taylor and Maccoll solutions for frozen supersonic flow over a cone

1.3 Previous literature

1.3.1 Frozen Flows

In the next decade after publication of the last three papers cited, many attempts were made to find empirical or exact formulas for the shape and/or location of the detached shock wave for the frozen flow around a cone. Heberle *et al.* (1949) make an experimental study for $M_\infty = 1.17 - 1.81$. They are interested in the pressure distribution and pressure drag of the fore part of cones and spheres. They fit the experimental data to an empirical formula for the detachment distance which works best for cases where the shock is fully detached. Moeckel (1949) derives an approximate equation for predicting the detachment distance based on the continuity equation. He assumes the shock to be an hyperbola and the sonic line to be straight with its angle determined from the free-stream Mach number. He finds good agreement between the predictions and available experimental data. Moeckel later does his own experiments (Moeckel, 1950) for a range of $M_\infty = 1.8 - 2.9$ and finds good agreement for the predicted detachment distance. A more detailed study of the shock shape for the case $M_\infty = 1.9$ finds that the shock can be well approximated by an hyperbola. Johnston (1952) does an extensive experimental study on cones at $M_\infty = 2.48$ to understand the behavior of the subsonic region behind the shock as the detachment process progresses. He observes that the subsonic region finds a stable position relative to the cone shoulder soon after detachment occurs. He also distinguishes three different regimes for cone flow: the attached regime with purely supersonic flow, the attached case with a mixed subsonic and supersonic flow, and the detached regime. Johnston gives different arguments to conclude that the sonic line meets the cone at the corner. He also measures the surface pressure and finds that the pressure drag increases throughout the detachment process. Finally, he notices that for the case of no favorable pressure gradient, the effect of the corner is "felt" a distance of about 15 times the boundary layer displacement thickness upstream of the actual corner.

Drougge (1948) is one of the first to tackle numerically the problem of mixed supersonic and subsonic regions in cone flows with detached shocks. His study is restricted to the range $M_\infty \leq 2.08$ and he complements the numerical analysis with experimental results. He solves the equations of motion in the subsonic region by relaxation methods assuming the shape and location of both the shock and sonic line since they are needed to determine the boundaries of the subsonic region. The process is iterative. The shape of the shock is obtained from Schlieren pictures. Yoshihara (1952) extends this work to the supersonic region by the use of the method of characteristics. This method is of successive approximation until the subsonic and supersonic solution are compatible. The method proves successful in converging to definite solutions and Yoshihara is also able to compute pressure coefficients along the cone surface.

In 1954 Solomon (Solomon, 1954) publishes a paper in which he summarizes the results obtained

until then and presents some experimental results of his own. This study is confined to transonic flow and relies on interferograms as the experimental data. Solomon confirms experimentally the existence of shock-free compressions from supersonic to subsonic conditions predicted by Busemann (1929). By doing so, he also finds experimentally the shape of the sonic line for different conditions, which turns out to be convex up and not concave up as some authors had previously assumed (for example Drougge (1948), Yoshihara (1952)). He divides the flow into different regimes and studies carefully the behavior of the sonic line and Mach contours in general. Finally, he notices that the for a given angle γ, the shock detaches at a lower Mach number than that predicted by Taylor and Maccoll (1933) but cannot explain why. The next chapter will present some arguments to explain this delay in detachment.

It is not until the late 1960's that the research in this area gets rekindled. Ward and Pugh (1968) obtain experimental data on the detachment distance for different cone angles at $M_\infty = 3.04$. They find that the non-dimensional detachment distance (non-dimensionalized by the cone base diameter) grows linearly with cone angle. They observe this behavior for both blunt and sharp cones. For the latter case, they measure the detachment distance from the shock to the projected intersection of any two rays along the surface of cone. Based on their own data and that obtained by Kaattari (1963) they conclude that the same behavior could be expected for other Mach numbers as long as the flow is frozen. We will use this result in chapter 2 to lay down the theoretical model for the present study.

1.3.2 Nonequilibrium flows for the attached case

Up to this point all the research cited has been only concerned with frozen flows. The first study in non-equilibrium cone flows is due to Spurk (1966). He presents experimental Mach-Zehnder interferograms for oxygen flows over cones obtained for one free-stream condition in an expansion tube. From the interferograms, he finds the shock shape and density contours. Spurk only considers attached cases where the flow is supersonic throughout and uses the method of characteristics for the computations. He compares the experimental data with the computational results for frozen, nonequilibrium and equilibrium flows. Spurk finds good agreement between the computed and experimental density contours and shock shape. For all these cases, he assumes the flow to be in vibrational equilibrium in the computations. He relaxes this last condition in his later paper Spurk (1970) where he takes into account coupling between vibration and dissociation. This study is also restricted to attached cases where the characteristics computations apply. Spurk compares the coupling model of Marrone and Treanor (1963) and Treanor and Marrone (1962) with the experimental data and finds qualitative agreement but appreciable differences in the shock geometry and density distributions.

1.3.3 Nonequilibrium flows for the detached case

Hornung and Smith (1979) study the effects of nonequilibrium on the detachment distance on wedges in hypervelocity flows. They conclude that the detachment distance is controlled by the distance from the leading edge of the model to the sonic line. A subsonic layer starts growing behind the shock as the wedge half-angle is increased beyond the frozen critical detachment angle. In the case of nonequilibrium flows, the sonic line may be embedded within the relaxation layer and one expects a smooth growth of the detachment distance as the angle is increased. For frozen flows, the length scale determining the detachment distance is the total height of the wedge as it is for equilibrium flows and one expects an abrupt jump in the detachment distance around the critical detachment angle. The experimental data show a slower growth, compared to the frozen case, of the detachment distance with wedge half-angle as predicted. The frozen case, however shows a continuous growth of the detachment distance and this discrepancy is attributed to end effects that can affect the flow in the same way as nonequilibrium effects (see figure 1.7).

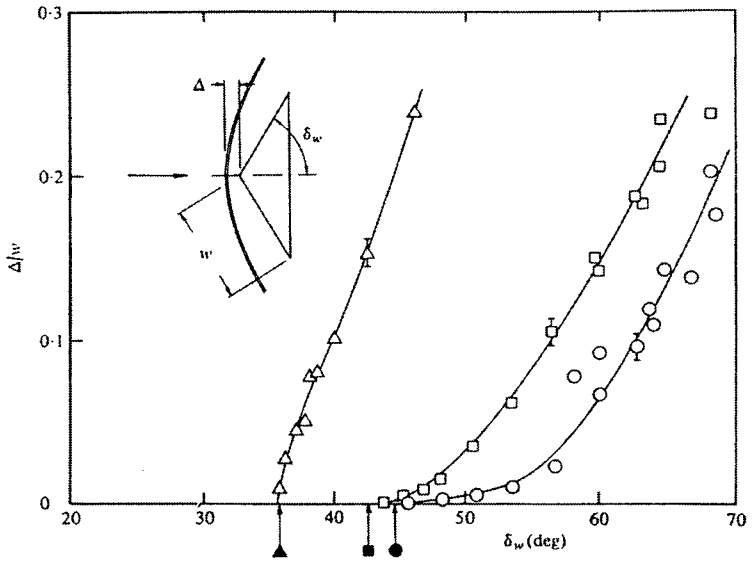

Figure 1.7: Experimental results for the detachment distance growth for different degrees of nonequilibrium in wedge flows. The hollow triangles represent runs in Ar (perfect gas). The hollow squares represent runs in dissociating N_2 and the hollow circles runs in dissociating CO_2. The filled symbols are computed values for the frozen detachment angles in the corresponding gases.

To avoid end effects, Hornung and Houwing (1980) decide to change from a 2-D model to an axisymmetric model, a cone, and study the effects of nonequilibrium on the detachment distance in a more controlled manner. The next chapter will explain in more detail their paper and how the present research expands their work.

1.4 Scope of the current work

Based on the earlier results of Hornung and Houwing (1980), the present study finds conclusive results on determining the effects of nonequilibrium on the detachment distance and characterizing its behavior from the frozen to the equilibrium limits. This study also includes heat flux and surface pressure measurements to determine if these variables are sensitive indicators of the degree of nonequilibrium. The study consists of about 170 shots performed in the Caltech Hypervelocity reflected shock tunnel (T5) and extensive numerical simulations which are able to account for chemical and vibrational nonequilibrium as well as viscous effects for axisymmetric flows. We have tested 24 models from diameters of 2 cm to 16 cm and angles from 55° to 75°. The cones with $d = 8\,\text{cm}$ are equipped with 7–8 thermocouples and the largest cones with 13–15 thermocouples and 5 pressure transducers. Holographic interferograms are taken of each shot and they are compared with their numerical counterparts. Each cone has been tested at six different free-stream conditions, four use N_2 as the test gas and two use CO_2. Once the numerical data are validated with the experimental results, we can use the extra field information provided by the simulations to better understand hypervelocity flows over cones for attached and detached cases.

Chapter 2 presents the theoretical model of Hornung and Houwing (1980) and relevant information about the boundary layer behavior of the present experiments and the heat flux expected. Chapter 3 describes the experimental facility where this work was done, the free-stream conditions chosen, and the models and instrumentation used as well as the data reduction methods. The numerical method and computational interferograms are explained in detail in chapter 4. Chapter 5 deals with the field experimental results such as interferograms and the data obtained from them, including the detachment distance. This chapter compares experimental and numerical results. Chapter 6 is concerned with the surface experimental results such as heat flux and pressure measurements. Experimental and numerical results are compared as well. The conclusions of the present study are listed in chapter 7.

Chapter 2 Theoretical considerations

The first part of this chapter discusses the inviscid model presented by Hornung and Houwing (1980). In order to present a complete view, most of their theory is repeated here. Since the real flow in all cases is viscous, and for the smallest cones ($d = 2\,\mathrm{cm}$) this might be significant in the experimental results, the second part of the chapter is concerned with deriving estimates for the boundary layer thickness and the momentum thickness. The expected dependency of the non-dimensional heat flux on Reynolds number is also discussed.

2.1 Inviscid model

2.1.1 Speed deflection diagrams

A useful way to illustrate the flow over cones from the frozen to the equilibrium limits is to use speed-deflection (V–ϕ) diagrams (see figure 2.1) where V is the flow speed and ϕ is the deflection angle, measured from the x-axis, of a streamline after it crosses the shock (not to be confused with the shock angle). The biggest value of V corresponds to zero deflection angle and it is the free-stream speed, V_∞. The lowest values of V for each curve represents the value that would be achieved after a normal shock. Together, f_s and f_c represent all possible attached solutions for frozen flow, starting with free-stream velocity V_∞, a given γ and M_∞. Curve f_s represents the conditions immediately behind the shock and it is obtained from plane oblique shock theory. Since the conditions after the shock are not uniform (like in wedge flow) and the streamline keeps deflecting until it reaches the cone half-angle asymptotically, we need another curve to describe the conditions at the cone surface. Curve f_c is such a curve. Curves e_s and e_c are the equivalent of f_s and f_c but for the equilibrium case. The maximum value of ϕ in curves f_c and e_c are the maximum values of cone half-angles for which attached shock solutions exist for the frozen and equilibrium cases respectively. As stated in textbooks, (see for example Vincenti and Kruger (1975)) for the same free-stream conditions the ratio of the density after the shock to the free-stream density is higher for an equilibrium flow than for a frozen flow. This is because the density ratio across a shock is increased by endothermic reactions such as dissociation. This results in a smaller shock layer thickness for the equilibrium case which explains why the critical detachment angle for frozen flows is smaller than for equilibrium flows for the same free-stream conditions. This difference in critical angles is the difference between the points ϕ_f and ϕ_e in figure 2.1 which correspond to cone half-angles θ_f and θ_e.

There is an apparent paradox in this figure; for cones with half-angles between θ_e and θ_f the

shock will be detached if we have frozen flow but attached if the flow is in equilibrium. This paradox is solved if the detachment distance in this interval is scaled by the relaxation length l and will be discussed in more detail in the following sections.

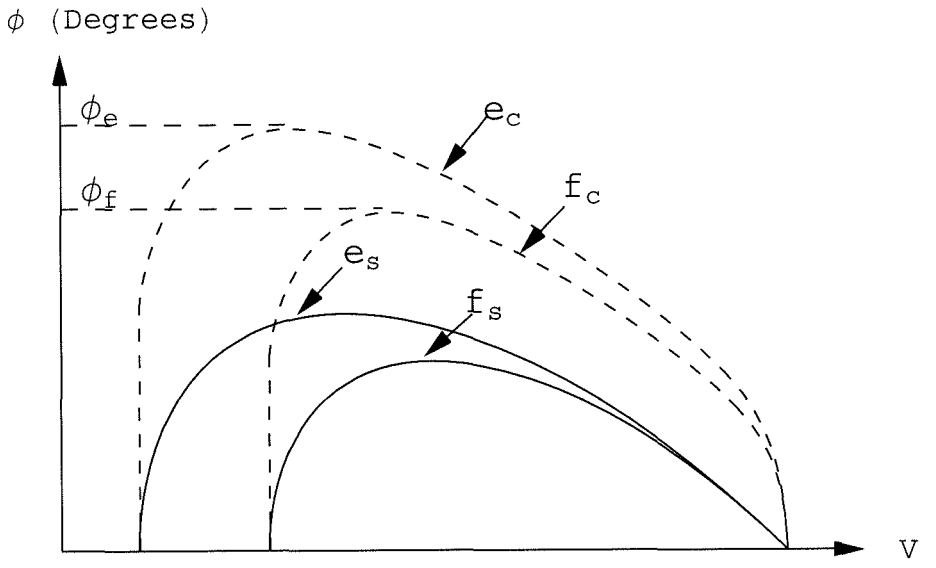

Figure 2.1: Speed-deflection diagram for cone flow

2.1.2 Frozen flows

Now consider the case of inviscid frozen flow in more detail. Assume that the free-stream conditions and the cone half-angle are such that the flow after the shock is supersonic throughout. For this case, the shock is straight and attached, and the conical solutions of Taylor and Maccoll (1933) apply. As the cone half-angle is increased, a point is reached where the flow becomes subsonic at the surface. At this point, the conical solutions of Taylor and Maccoll (1933) not longer apply since the perturbation of the flow due to the corner can be transmitted upstream through the subsonic region; thus, destroying the conical nature of the flow. The flow conditions when the flow is subsonic near the surface look like those depicted in figure 2.2.

A subsonic region is embedded in an otherwise supersonic field. This case is in fact an example of the shock-free compressions from supersonic to subsonic flow that Busemann postulated in his pioneering paper Busemann (1929). As the cone half-angle keeps increasing the subsonic region grows to fill the shock layer. The two arrows in figure 2.2 show the directions of growth of the sonic line. In order for the shock to detach, the subsonic region has to grow until the sonic line meets the shock on the upstream end and the corner in the downstream end (see figure 2.3). It is only then that the size of the cone can be communicated to the cone tip and the detachment distance

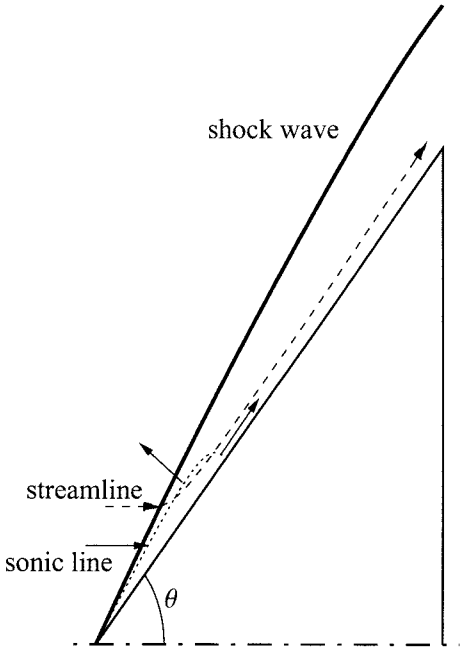

Figure 2.2: Frozen flow with attached shock and embedded subsonic region. The flow along the streamline marked in the diagram becomes subsonic and then supersonic again as it travels through the shock layer. The two arrows in the sonic line mark its directions of growth.

has a length scale upon which to depend, *i. e.*, the cone diameter (d). Solomon (1954), observed that the detachment critical angle for finite cones was bigger than the detachment angle predicted from conical flow (Taylor and Maccoll, 1933) for semi-infinite cones. He could not explain why. The explanation lies in the growth of the subsonic region and the behavior of the sonic line described above. When the shock is fully detached, the flow field looks like that depicted in figure 2.4. The point where the sonic line intersects the shock wave is the sonic point of oblique shock theory.

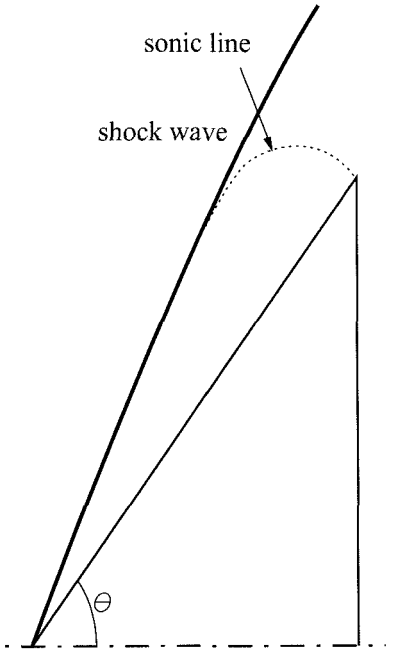

Figure 2.3: Incipient detachment in frozen flow. The sonic line has reached the corner of the cone in the downstream end and the shock in the upstream end.

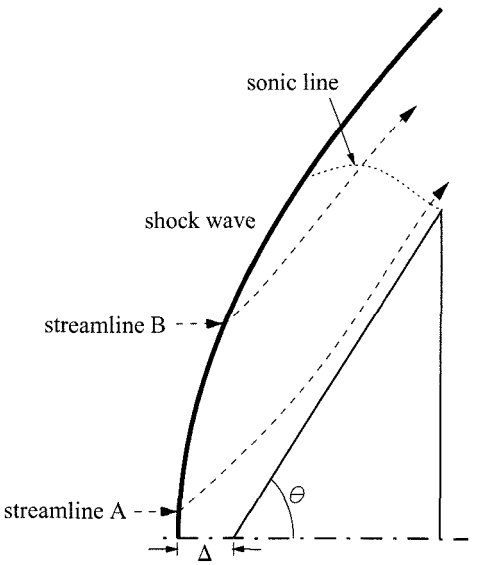

Figure 2.4: Fully detached frozen or equilibrium flow.

2.1.3 Nonequilibrium flows

Now consider nonequilibrium flows. Again, start with an attached-shock case where the flow is supersonic throughout. This situation is depicted in figure 2.5. As may be seen, nonequilibrium flows have an additional length scale, the relaxation length (l). As the cone half-angle increases, a point is reached at which a subsonic region starts growing behind the shock as depicted in figure 2.6. At first, the subsonic region is entirely contained in the relaxation region and the growth of the sonic line is determined by the relaxation processes. In this case, there will be some streamlines along which the flow becomes subsonic immediately after the shock but becomes supersonic again within the relaxation zone (see curve denoted as "streamline" in figure 2.6). Hornung and Smith (1979) studied in detail the effects of relaxation on the extent of the subsonic region within the relaxation zone. They concluded that within the relaxation zone, the frozen speed of sound decreases more rapidly than the flow speed along a streamline. This means that depending on the initial values of both variables (determined by the cone half-angle for the same free-stream conditions) we can have cases of supersonic only, subsonic-supersonic, or subsonic only flow within the relaxation zone for a given streamline.

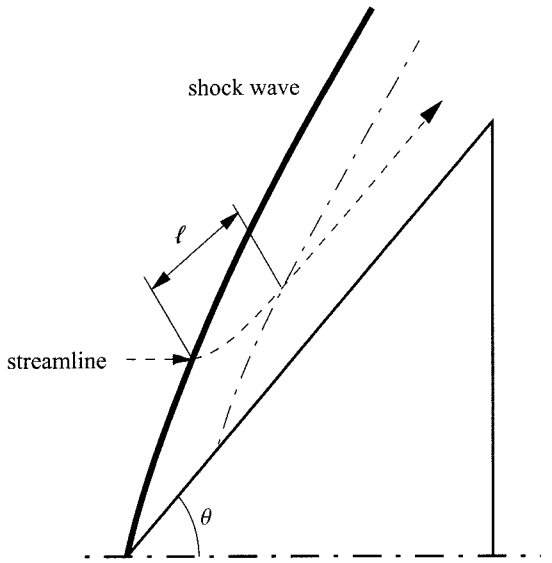

Figure 2.5: Nonequilibrium flow with attached shock. Conditions are supersonic throughout the shock layer. Nonequilibrium flows introduce a new length scale into the problem, the relaxation length l.

As we keep increasing the cone half-angle the subsonic region keeps growing and when we reach the critical value of θ_f the shock starts to detach, but the detachment distance is be governed by l and not by d as was the case for frozen flows. This happens when the sonic line reaches the end of the relaxation zone. Figure 2.7 illustrates this case, where the detachment distance is infinitesimal.

For this case, the flow in the stagnation streamline is completely subsonic within the relaxation zone. The range of cone half-angles for which the detachment distance depends on l is from θ_f to θ_e which are represented by ϕ_f and ϕ_e respectively in figure 2.1. For this range of angles, the shock is detached if the flow is frozen but attached if the flow is in equilibrium. When the cone half-angle is such that the sonic line has reached the end of the cone (θ_e), the growth of the detachment distance is governed by d from this angle on. Also, for cone half-angles larger than θ_e, the shock will be detached regardless of the degree of nonequilibrium of the flow. The fully detached case looks very similar to that depicted in figure 2.4. We expect the growth of the detachment distance with increasing θ to be slower when it is governed by the relaxation length than when it is governed by the size of the cone due to the effects of nonequilibrium as described above.

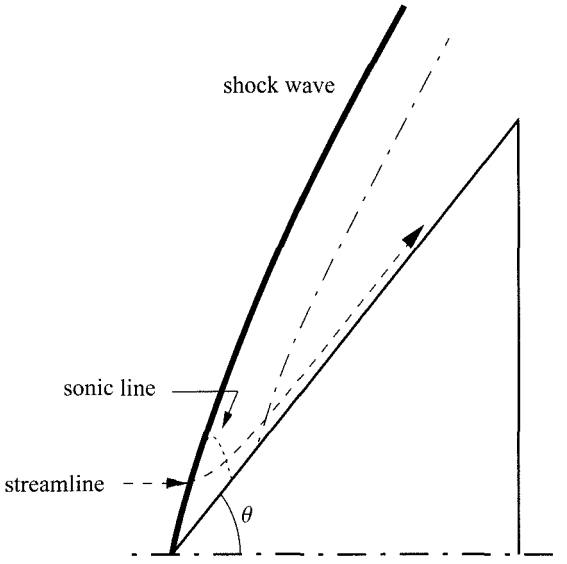

Figure 2.6: Attached case for nonequilibrium flow with subsonic region embedded in the shock layer.

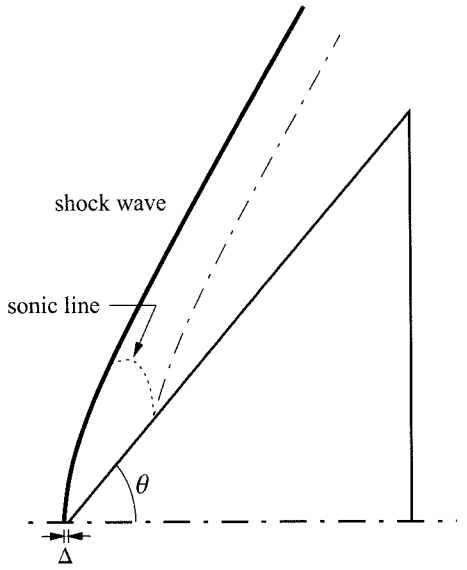

Figure 2.7: Incipient detachment for nonequilibrium flow. The sonic line has reached the end of the relaxation length. The detachment distance is infinitesimal.

2.1.4 Equilibrium flows

Equilibrium flows are very similar to frozen flows in that there is only one important length scale in the problem, namely the size of the cone. Therefore, $\Delta = O(d)$ for a given cone half-angle. That is, as we approach the equilibrium limit (or the frozen limit), the value of Δ/d reaches a constant value which depends on the cone half-angle and the initial conditions. We will test this assertion numerically in section 5.5. The sequence of events described before for the transition between attached and detached shocks for frozen flows applies also to the equilibrium case.

2.1.5 Expected behavior of the detachment distance growth for different values of l/d and cone half-angle

As can be concluded from above, a good indicator of the degree of nonequilibrium of the flow is the ratio l/d. If this ratio tends to infinity then the flow approaches the frozen limit. If, on the other hand, l/d approaches zero the flow approaches the equilibrium limit. Non-dimensionalizing the detachment distance by the diameter of the cone (Δ/d) should yield a functional form like,

$$\frac{\Delta}{d} = \frac{\Delta}{d}\left(\frac{l}{d}, \theta\right), \tag{2.1}$$

where it is clear that the detachment distance is a function of l/d and also of the cone half-angle. When l is about the same size as d both parameters are important in determining the behavior of the detachment distance. In the range of angles just above the frozen detachment angle, l scales

the detachment distance, and as the angle is further increased, d takes over. In this study, we vary the ratio l/d by varying the diameter of the cones being tested in one given free-stream condition. The smaller the cone diameter the closer the flow gets to the frozen limit. It is safe to assume that l is constant for a given free-stream condition since the cone half-angles used for testing are around incipient detachment. The ratio can also be changed by changing l which implies changing the free-stream condition or the gas altogether. The former method is preferred since for each free-stream condition we conserve the functional forms of equation 2.1 and the values of θ_e and θ_f in figure 2.1.

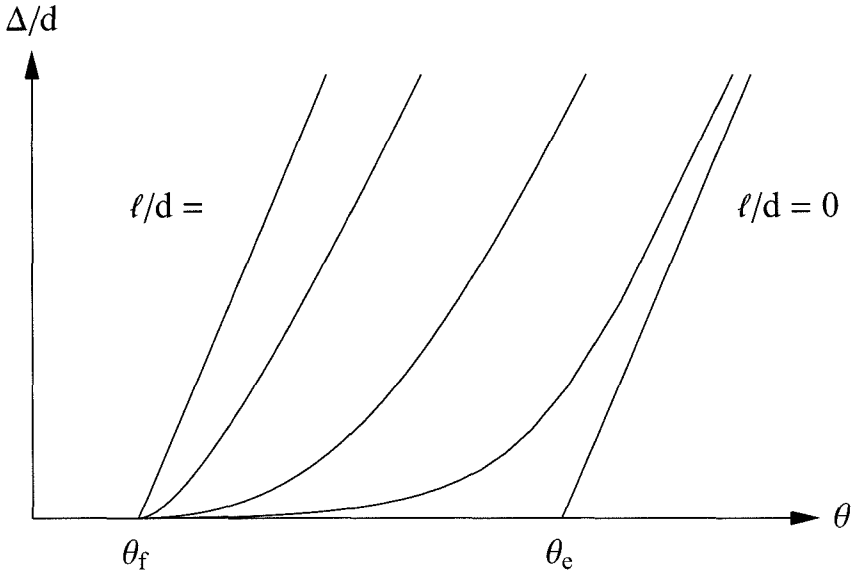

Figure 2.8: Shock detachment growth for different degrees of nonequilibrium

The ideas presented above are summarized in figure 2.8. The linear growth of the detachment distance with cone half-angle for the frozen case ($l/d = \infty$) has been demonstrated experimentally by Ward and Pugh (1968) and Hornung and Houwing (1980), and computationally with the two independent CFD codes used in this work, see chapter 5. Since the equilibrium limit ($l/d = 0$) is similar to the frozen one in that there is only one length scale upon which the detachment distance can depend, we also expect a linear growth of the detachment distance with cone half-angle, as seen in the line labelled ($l/d = 0$). This assumption has been confirmed computationally in the present study (see section 5.5). The curves between the frozen and equilibrium limits correspond to nonequilibrium flows. Notice how all these curves start from the same point, θ_f. As soon, as the cone half-angle exceeds θ_f the shock begins to detach in accordance to the solution of the paradox mentioned in 2.1.1. For these cases the growth of the detachment distance is slower than for the frozen and equilibrium cases in the range of angles between θ_f and θ_e. In this range the growth of

the detachment distance is governed by l. As the cone half-angle exceeds θ_e the detachment distance growth asymptotes the linear behavior of the frozen and equilibrium limits. Notice that for the range of angles between θ_f and θ_e the shock has started to detach for frozen and nonequilibrium flows but it is still attached for equilibrium flows. It is the same phenomenon as that pointed out in figure 2.1

2.2 Viscous effects

It is convenient to start a discussion of boundary layers with the theory of a flat-plate in nonreacting flows. The last assumption is necessary for self-similar boundary layer solutions to exist. Reacting boundary layer equations do not have self-similar solutions and must be solved with finite difference methods. In the spirit of obtaining estimates for the boundary layer and the momentum thickness this analysis is limited to frozen boundary layers. The case of most interest here is that for attached shocks where the conditions outside the boundary layer are uniform and the Mach number is about one at the edge of the boundary layer. To better model compressible boundary layers with hot or cold walls, like the present case where the model wall temperature is about 7% of the edge temperature, the reference conditions (denoted by the superscript *) are used when evaluating expressions for the boundary layer thickness, momentum thickness and non-dimensional heat flux (White, 1991). The reference temperature was derived by Dorrance (1962) to be,

$$\frac{T^*}{T_e} = \frac{1}{2} + \frac{\gamma - 1}{12} r M_e^2 + \frac{1}{2}\frac{T_w}{T_e}, \tag{2.2}$$

where r is the recovery factor and the subscript e refers to conditions at the edge of the boundary layer. From Mallinson *et al.* (1996), the boundary layer thickness is,

$$\frac{\delta}{x} \simeq 1.719\sqrt{\frac{C^*}{Re_x}}\left(1.866 + \frac{T_w}{T_e} + .192 r(\gamma - 1)M_e^2\right), \tag{2.3}$$

where $C = \rho\mu/\rho_e\mu_e$ is the Chapman-Rubesin parameter, $Pr = \mu C_p/k$ is the Prandtl number. The recovery factor is introduced to account approximately for $Pr \neq 1$. For laminar flows $r = \sqrt{Pr}$ while for turbulent flows $r \approx \sqrt[3]{Pr}$. The Reynolds number, Re will be defined later in this section. In deriving expression 2.3, it is assumed that $C = 1$, $Pr = 1$, and C_p= constant in the energy equation. In the momentum equation, C^* replaces C ($C^* \neq 1$) to account for the cold wall. This can be done because the temperature profile is insensitive to the viscosity law for $Pr \sim 1$ (see Stewartson (1964)). The edge and reference conditions (apart from T^* which is given by equation 2.2) can be obtained from the CFD results.

The displacement thickness is given by,

$$\delta^* \simeq 1.721\sqrt{\frac{C^*}{Re_x}}\left(\frac{T_w}{T_e} + .193\sqrt{Pr}(\gamma - 1)M_e^2\right), \tag{2.4}$$

and the axisymmetric nature of the flow is taken into account by applying a Mangler transformation which results in

$$\delta^*_{cone} = \sqrt{3}\,\delta^*_{plate}\,. \tag{2.5}$$

To study the heat flux traces obtained in the present study, the first step is to non-dimensionalize them so that the results become more portable when comparing them with previous results or theoretical models. The Reynolds number serves to non-dimensionalize the distance along the surface of the cone and is given by,

$$Re_x = \frac{\rho_{eq} u_{eq} x}{\mu_{eq}}\,, \tag{2.6}$$

where the flow properties are evaluated in the stagnation streamline after the shock when the vibrational and translational temperature are in equilibrium. For compressible boundary layers, the heat flux is non-dimensionalized into the Stanton number (St) as follows,

$$St = \frac{\dot{q}}{\rho_\infty u_\infty \left(h_o - \frac{1}{2}u_\infty^2(1-r) - C_p T_w\right)}\,, \tag{2.7}$$

where the flow conditions are evaluated on the stagnation streamline immediately before the shock. For the present study, the only cases where compressibility effects are important are the attached shock cases. However, even in those cases $Pr \sim 1$ and so the second term in the denominator can be neglected. Also, the enthalpy at the wall, given by $C_p T_w$ can be neglected when compared with h_o. The resulting expression for St is then,

$$St = \frac{\dot{q}}{\rho_\infty u_\infty h_o}\,. \tag{2.8}$$

In order to relate St and Re one resorts to the Reynolds analogy which relates the skin friction coefficient (C_f) to Pr and St for boundary layers at high speed. The analogy applies to both laminar and turbulent flows (White, 1991) and the factor 1/2 is for flows with no pressure gradients,

$$St \approx \frac{1}{2} C_f Pr^{-2/3}\,, \tag{2.9}$$

where the skin friction coefficient is defined as,

$$C_f(x) = \frac{\tau_w(x)}{\frac{1}{2}\rho_e u_e^2}\,, \tag{2.10}$$

and τ_w is the shear stress at the wall. Starting with the Blasius solution for an incompressible two-dimensional boundary layer with no pressure gradient and introducing the Chapman-Rubesin parameter evaluated at the reference conditions to take into account both compressibility effects and the cold wall, we have,

$$C_f(x) \approx \frac{.664}{\sqrt{Re_x}}\sqrt{C^*}. \tag{2.11}$$

For laminar flows, the Mangler transformation can also be applied in this case to give,

$$C_{f,cone}(x) = \sqrt{3}C_{f,plate}. \tag{2.12}$$

Putting all the above expression together the final expression for the Stanton number as a function of the Reynolds number is,

$$St \approx \frac{.664\sqrt{3}\sqrt{C^*}}{2Pr^{2/3}\sqrt{Re}}, \tag{2.13}$$

or,

$$St \approx \frac{A}{\sqrt{Re}}, \tag{2.14}$$

where $\frac{\sqrt{C^*}}{Pr^{2/3}}$ is considered to be approximately constant. This expression is only valid for the attached cases where the pressure gradient is zero. For the rest of the cases, it serves only as a bound for the heat flux.

Chapter 3 Experimental setup

This chapter describes the experimental facility and the choice of test conditions, as well as the models, instrumentation and flow visualization used in this project.

3.1 GALCIT free-piston reflected-shock tunnel — T5

T5 was completed in 1990 and about 2000 runs have been performed in it. It is a reflected-shock tunnel that uses piston compression to heat the driver gas, like its predecessors T1 through T4 in Australia. A schematic diagram of the facility is shown in figure 3.1.

The tunnel consists of six major parts, the secondary reservoir (2R), the compression tube (CT), the shock tube (ST), the throat-nozzle region (T-N), the test section (TS), and the dump tank (DT). The objective of the facility is to create stagnation conditions with high enough pressure and enthalpy that when expanded steadily through a nozzle one can obtain the desired test conditions of high velocity, pressure, and density necessary to simulate hypervelocity flows. To achieve this, a piston weighing 120 kg is accelerated (using compressed air) into the CT which initially contains a mixture of helium and argon, at room temperature and pressure. This driver gas is adiabatically compressed until the pressure is high enough to burst the primary diaphragm. The compression ratio and mixture ratio are chosen to give the desired speed of sound in the driver gas. The piston continues to move after the diaphragm breaks, and thus maintains approximately constant pressure for the duration of the test time. By careful choice of pressures and mixture ratio, the piston is safely stopped by buffers at the end of the CT. The motion of the piston also causes the whole facility, except for the TS and DT, to recoil. The transient stresses in the facility can be reduced by reducing the recoil. For this reason an inertial mass of about 14 tons is added to the end of the CT limiting the recoil to about 11 cm. When the main diaphragm breaks, a shock is created that travels through the ST accelerating and heating the test gas. The shock reflects off the end wall of the ST and it vaporizes the mylar diaphragm separating the ST from T-N. As the shock travels in the opposite direction through the test gas, it brings it to rest or stagnation conditions. The gas then expands steadily through the nozzle and the gas at the exit of the nozzle constitutes the test gas. The T-N, TS and ST are initially under vacuum. For more details on the operation of T5 see Hornung and Belanger (1990)

The variables that are recorded to monitor the operation of the facility are the initial CT pressure, the initial 2R pressure and temperature, the initial ST pressure and temperature, the stagnation and burst pressures, the shock speed, and the recoil distances of the CT and the 2R. The burst and

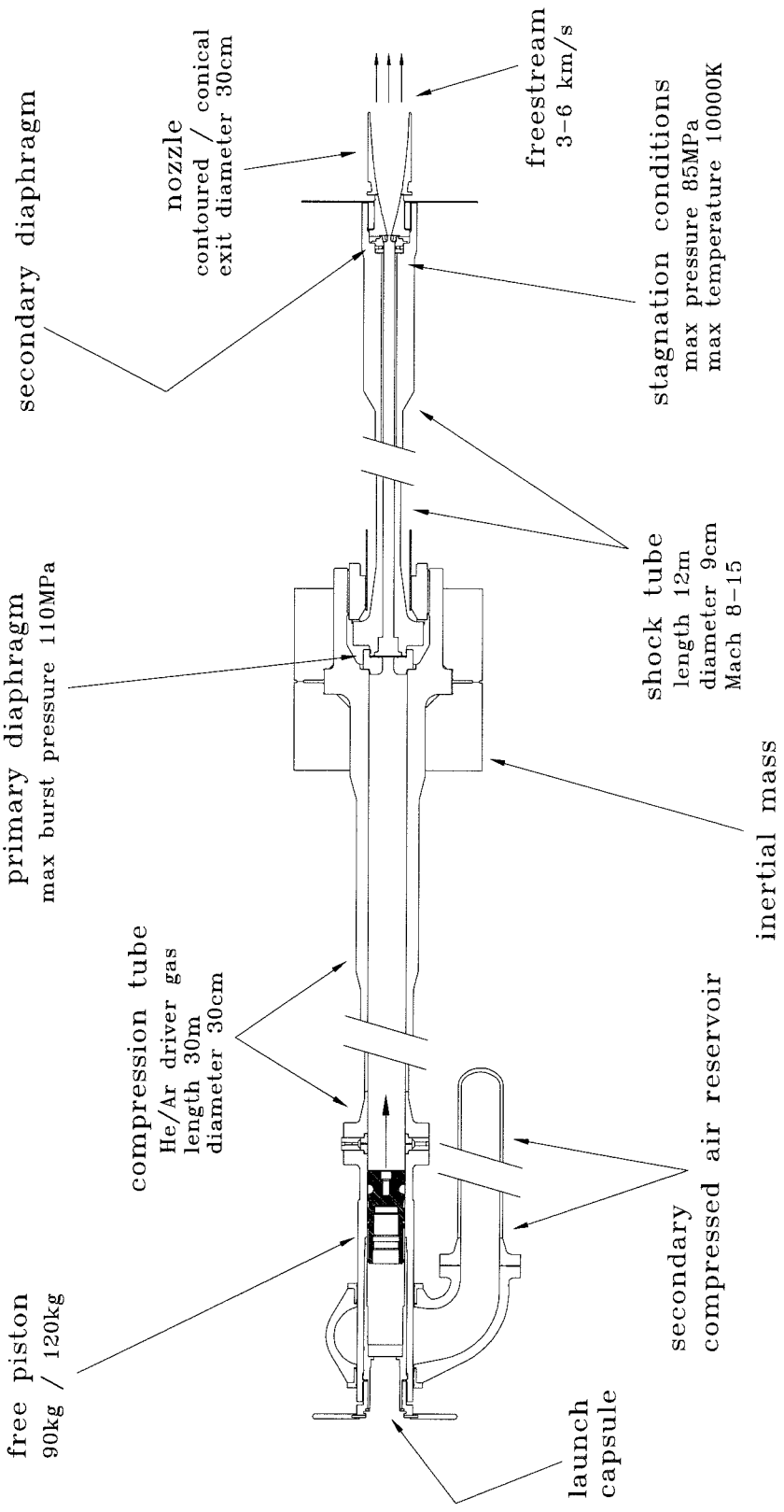

Figure 3.1: Sketch of T5 hypervelocity shock tunnel from Davis (1998).

stagnation pressures are each measured with two piezoelectric transducers (PCB Piezotronics Inc., model no. 119M44). The stagnation pressure P_o is measured 4.8 cm from the end wall of the ST and the burst pressure p_4, is measured 1.4 cm upstream of the main diaphragm. The shock speed u_s, is calculated by recording the time interval between the signal rise of two pressure transducers with known axial separation along the shock tube. The transducers are similar to the ones used for measuring P_o and p_4. The recoils are recorded using linear voltage displacement transducers (LVDT).

The data acquisition system (DAS) for T5 consists of three CAMAC-standard crates from DSP technology, with 60 A/D digitizers, 50 amplifiers, and a trigger generator. The digitizers have a 12-bit resolution on ± 5 V and a maximum sampling rate of 1 MHz. One crate with eight digitizer channels (divided in four pairs) is devoted to record the T5 operation, as described before. The sampling frequency and trigger time for each pair can be set independently from each other. The rest of the digitizers are used to monitor model instrumentation. The triggering for the system is two-step, the first signal coming from an accelerometer located near the upstream end of the CT at about 200 ms before shock reflection. This signal is needed to control the laser used for flow visualization. The second signal comes from P_o and sets the time $t = 0$ for recording the test-section data. For these experiments the sampling rate for each model instrument was 200 kHz with a recording length of 4 kbs from which 2/8 was devoted to pre-trigger data. The system is controlled from a SUN Sparc station with software that was built in-house.

3.2 Flow visualization

Holographic interferometry is chosen for this project, because it provides the field information needed for a quantitative comparison with computed flow fields. The holographic interferometer used was designed and built by Sanderson and is described in detail in Sanderson (1995), see figure 3.2. The apparatus is a double pulse interferometer. The first pulse is taken a few minutes before a shot and the second one is taken during the flow test time. Each pulse is divided into two beams, one going through the test section and the other being a reference beam. They have the same path length and meet at the holographic film (Kodak SO-253) at a 5° angle where they record their interference pattern as a hologram. The two test section beams are simultaneously reconstructed with white light. The film used for reconstruction is either 35 mm Kodak TPAN film or 35 mm Kodak b&w ASA 100 film.

The shock detachment distance is measured directly from the interferograms. The detachment distance and the number and shape of fringes are compared with computational interferograms. These are obtained with the numerical code written by Olejniczak (1997) which will be discussed in more detail below and in the next chapter.

Because the holographic interferogram is generated by recording the difference between a flow-record and a no-flow-record, additional changes in phase shift that might appear from optics imperfections do not show in the final interference pattern, and the optical windows can be of lesser quality than those required with other techniques Smeets (1990). The windows used for this test were made out of BK–7 material. A disadvantage of the particular instrument used for this project is the small diameter of the field of view, 7 cm.

The fringes that appear in the free-stream are the result of mechanical vibrations of different components of the system such as the camera mounting setup, the laser beam, mirrors and beam splitters, and the floor itself during the time interval between the two pulses. These free-stream fringes are taken into account in the comparisons with computations and will be discussed in more detail in section 4.2.3.

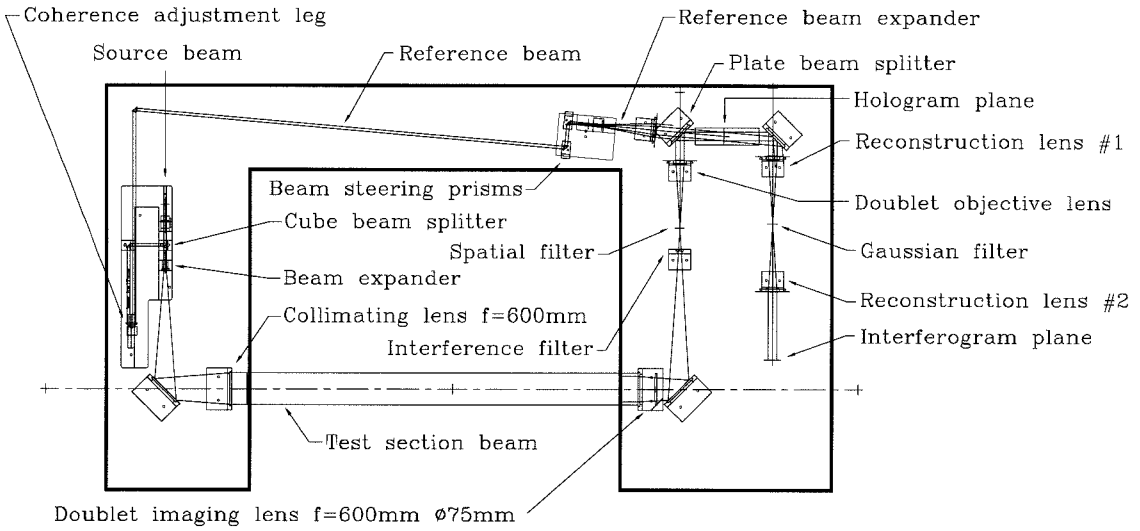

Figure 3.2: Sketch of holographic interferometer from Sanderson (1995).

3.3 Free-stream conditions

As was shown in chapter 1, the separation between the detachment angle of frozen and of equilibrium flows depends on the amount of energy that goes into dissociation. For a given gas this depends on the specific reservoir enthalpy h_o. Therefore one way to vary the separation between the critical detachment angles is simply to have free-stream conditions with different h_o. Another way to obtain even larger differences is to change the test gas. For this project, N_2 and CO_2 are chosen as test gases based on the success of this choice by Hornung and Smith (1979). One can also control how close a given flow is to the frozen or equilibrium limit by changing the model size and the free-stream density.

Condition	N_2 1	N_2 2	N_2 3	N_2 4	CO_2 2	CO_2 3
Filling conditions						
P_{2R}(psig)	1175	1100	435	611	550	1425
P_{CT} (KPa)	116	116	58.0	82.2	74.0	124
% He	97	85	95	84	84	86
P_{ST} (KPa)	40	90	23	60	40	60
Measured quantities						
u_s (km/s)	4.24	3.28	4.14	3.04	2.78	3.14
p_4 (MPa)	50.2	51.7	49.1	46.2	43.1	63.4
P_o (MPa)	53.6 ± 1.5	53.9 ± 2.8	20.3 ± 1.3	28.2 ± 1.5	24.5 ± 1.2	64.7 ± 1.8
Computed quantity						
h_o (MJ/kg)	18.2 ± 0.7	10.3 ± 0.9	16.3 ± 1.1	9.20 ± .38	6.62 ± 0.39	9.13 ± .46

Table 3.1: Initial T5 filling conditions and relevant measured and computed parameters.

The present project comprises five series of experiments, with a total of 177 shots. The free-stream conditions are selected to span from conditions close to chemical equilibrium to conditions close to frozen flow. There are six conditions in total, four with N_2 and two with CO_2 as test gases. The conditions with N_2 have both high/low stagnation pressure with high/low stagnation enthalpy, to study separately the effect of each variable when the other remains the same. For CO_2 there are two conditions only, one with both low stagnation enthalpy and stagnation pressure and one with both high stagnation enthalpy and stagnation pressure.

For these experiments, the free-stream conditions are characterized by the values of P_o and h_o with constant nozzle area ratio. Changing the area ratio could provide additional control over the density. For this particular case, however, we could attain a wide range of conditions with different degrees of chemical non-equilibrium by varying only the two parameters mentioned above. The nozzle throat used throughout the experiments has a diameter of 3 cm, giving a nozzle exit area ratio of 100. The nozzle used is conical with a 7° half-angle.

The value of h_o and T_o are obtained using either the ESTC code, equilibrium shock tube calculation, by McIntosh (1970) or STANJAN written by Reynolds (1986). The inputs for these programs are the filling pressure and temperature in the shock tube (P_1 and T_1), the composition of the gas, P_o and u_s. ESTC uses a harmonic oscillator approximation to calculate thermodynamic properties below 5000 K and curve fits above this temperature. STANJAN uses JANAF curve fits to calculate the thermodynamic properties of the gases. For the conditions with high h_o the gas is highly dissociated in the reservoir. Table 3.1 shows the six free-stream conditions used in this project with the filling conditions used, the shock speed, and the reservoir conditions. The values given for h_o and P_o represent the mean and the standard deviation obtained by averaging the values of all the shots performed for a given free-stream condition. In the case of P_o where there are two indepen-

Condition	N_2 1	N_2 2	N_2 3	N_2 4	CO_2 2	CO_2 3
T_∞ (K)	2200	1100	1700	868	1470	1840
T_{v_∞} (K)	3340	2740	3500	2780	1470	1840
ρ_∞ (kg/m^3)	.0305	.0458	.0132	.0273	.0457	.106
u_∞ (km/s)	5.27	4.23	4.97	3.90	2.91	3.11
p_∞ (kPa)	26.6	19.0	8.91	8.94	13.9	38.6
$[N2]$ (kg/kg)	.975	.998	.964	.998		
$[CO_2]$ (kg/kg)					.813	.893
$[CO]$ (kg/kg)					.119	.068
$[O_2]$ (kg/kg)					.067	.038
$[C]$ (kg/kg)					7.42e-15	1.00e-10
$[O]$ (kg/kg)					.001	.001
M_∞	5.20	6.02	5.54	6.26	4.46	4.34
d_{ep} (cm)	14.1	14.1	13.0	13.8	13.6	14.9

Table 3.2: Calculated free-stream conditions.

dent readings for every shot, the average value of both readings is used when calculating the global average.

The free-stream conditions at the exit plane of the nozzle and downstream are calculated using any one of three programs: NENZF, SURF or a full Navier-Stokes solver (Olejniczak, 1997). NENZF is a quasi-one-dimensional nonequilibrium code for nozzle flows written by Lordi *et al.* (1966). It is used as a first approximation for all the shots and as the final calculation for the condition CO_2 3 for which the other programs failed to converge. SURF, an axisymmetric inviscid nonequilibrium code written by Rein (1989) is used to obtain the equilibrium solution downstream of the nozzle throat, about 2-5 mm, where the flow is supersonic. This solution serves as the input for Olejniczak's code which also accounts for thermochemical nonequilibrium. The latter code assumes a laminar boundary layer on the nozzle wall to approximate the boundary layer displacement effect. The flow in the actual nozzle is expected to be transitional or turbulent. Table 3.2 shows the free-stream conditions calculated for all the tunnel conditions used. The variable d_{ep} is the average distance from the nozzle exit plane to the tip of the models.

3.4 Models and instrumentation

For these experiments 24 cones were built with 4 different base diameters and 6 different half-angles. The set of angles for the cones with $d = 8$ cm is different from that of the rest of the cones because they were designed earlier, and it was later decided to make the smallest cone half-angle closer to the minimum half-angle needed to obtain a detached shock in frozen flows. The cones are made of 303

stainless steel to better match the product $\sqrt{\rho c k}$ of the materials used in building the thermocouples. The match serves to minimize local nonuniformities in the wall temperature which could disturb the boundary layer. Stainless steel is also chosen for its corrosion resistance. Figure 3.3 shows two models in the test section, $d = 2\,\text{cm}$ with $\theta = 75°$ and $d = 4\,\text{cm}$ with $\theta = 56°$ respectively. The sting holder used for these experiments was designed by Lemieux (1999). The larger cones ($d = 8\,\text{cm}$ and $d = 16\,\text{cm}$) are instrumented with thermocouples and the largest cones ($d = 16\,\text{cm}$) also have 5 pressure transducers each. There were only 10 pressure transducers available which were shared by all the largest cones. The complete lists with the locations of the instruments for each cone are found in appendix A. The positions of the thermocouples and pressure transducers are a compromise between cost of machining and span of the entire flow field. Since the flow field is axisymmetric, one could put all the instruments on the same cone generator; however, to minimize the instrument damage at a given time by debris, the sensors are distributed over the entire surface of the cone.

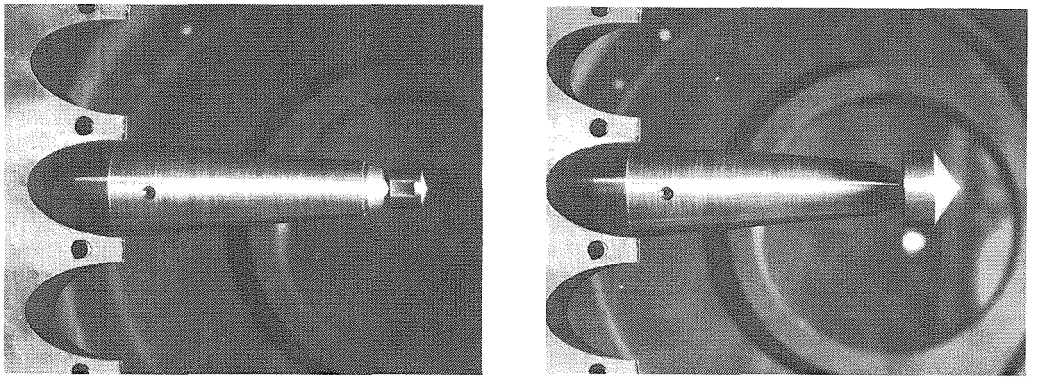

$d = 2\,\text{cm}$ and $\theta = 75°$ $\quad$ $d = 4\,\text{cm}$ and $\theta = 56°$

Figure 3.3: Test models installed in test section of T5.

A schematic diagram of the arrangement of the models with respect to the nozzle exit plane is shown in figure 3.4. The tip of all models was on the nozzle centerline to within $\pm.08$ cm in the vertical and horizontal directions. The angle of attack and yaw were no more than .02°. The distance d_{ep} depended on the recoil for the different conditions and the error for these measurements is about $\pm$ 2%. The instrumentation cables were protected from the high temperatures and pressures by placing them inside the sting first, and then inside a flexible air-tight conduit. The models were inspected under a microscope after every shot to check the sharpness of the tip, the roughness of the surface, and any damage to thermocouples or pressure transducers. The radius of curvature of the tip of any cone was $\leq$ 0.8mm. Defective instruments were replaced and the smaller cones ($d = 2\,\text{cm}$ and $d = 4\,\text{cm}$) were remachined after every 4–5 shots to keep the tip sharp. All the $d = 8\,\text{cm}$ cones were remachined before the last campaign of experiments. The models were also sanded, with very fine sand paper, at specific places if they had been hit by debris and had small

grooves. The remaining grooves were then filled flush with the model with epoxy.

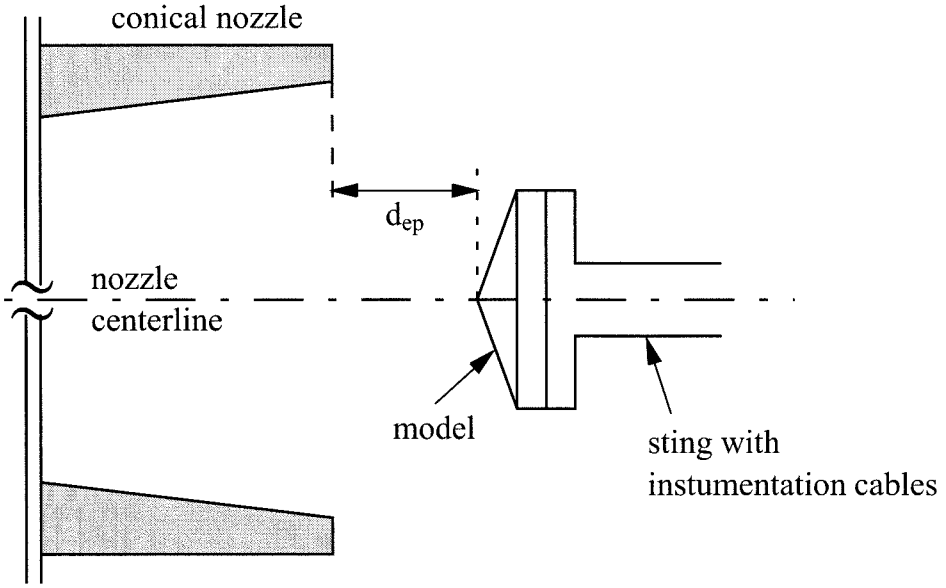

Figure 3.4: Schematic diagram of a typical model in test section

3.5 Temperature and heat flux measurements

The temperature measurements are made using in-house built thermocouples following the low-noise design by Sanderson (1995). These coaxial type E thermocouples have a chromel inner electrode and a constantan outer electrode and have a response time of about 1 μs. These thermocouples have a diameter of 2.4 mm and are mounted flush with the model. Loctite 271 is used to secure the thermocouples in the models. The EMF generated between the two electrodes is amplified according to the free-stream condition being used, with gains ranging from 200 to 1000. These amplifiers have a cut-off frequency of 100 kHz. The sampling rate for the temperature measurements is 200 kHz over 20.5 ms with 2/8 of this data being pre-trigger data. Since one is only interested in the change in temperature during a test, the initial voltage in the pre-trigger segment of the data is subtracted from the rest of the data to give only differentials in voltage (ΔV). The initial temperature used to convert ΔV to temperature differentials (ΔT) is room temperature (T_{amb}) since the reference junction for each thermocouple is at the connector inside the model and the temperature at this location does not change during a shot. The relation between ΔV and ΔT is obtained from NIST ASTM (1993). Also, care is taken to add the EMF corresponding to T_{amb} to the total EMF recorded since the above tables assume T_{ref}=0°.

The temperature traces are converted to heat flux ($\dot{q}$) traces using spectral deconvolution. This

technique assumes one-dimensional unsteady heat transfer in a semi-infinite solid, which for small temperature gradients and constant thermal properties is given by the familiar heat equation,

$$\frac{\partial^2 T}{\partial y^2} = \frac{1}{\alpha}\frac{\partial T}{\partial t}, \tag{3.1}$$

subject to the following boundary conditions (BC's):

$$T(y,0) = T_i, \qquad T(0,t) = T_i + \Delta T(t), \tag{3.2}$$

$$\left.\frac{\partial T(t)}{\partial y}\right|_{y\to\infty} = 0, \qquad \left.\frac{\partial T(t)}{\partial y}\right|_{y=0} = \dot{q}(t), \tag{3.3}$$

where y is the coordinate normal to the surface and α, the thermal diffusivity, is given by $\alpha = k/\rho c$ where k is the thermal conductivity and c is the specific heat of the material. Since the heat equation is linear, the solution is given by:

$$\Delta T(y,t) = \int_0^t g(y, t-t')\,\dot{q}(t')\,dt' \tag{3.4}$$

where $g(y,t)$, the unit impulse response function is given by,

$$g(y,t) = \sqrt{\frac{\alpha}{\pi k^2 t}}\exp\frac{-y^2}{4\alpha t}; \qquad t > 0. \tag{3.5}$$

The system can now be solved for $\dot{q}(t)$ using fast Fourier transform algorithms (see Press *et al.* (1992)). These algorithms are well suited for noisy experimental data and provide a mean square optimal estimate for $\dot{q}(t)$. For further details on the application of this technique to the temperature traces see Davis (1998). The processing of the temperature traces for this study follows that of the above author. For the present project, a filter cutoff at f_c=20 kHz is used to process thermocouple data. Also $\Delta V(t)$ and $g(y,t)$ are padded with zeros to four times the original length to ensure causality of the data. A similar study to that made by Davis (1998) to compare different techniques for obtaining $\dot{q}(t)$ was undertaken, but in this case, the values of $\dot{q}(t)$ were 4–6 times larger due to the different nature of the flow field around cones. The conclusion was the same, that is, to obtain most accurate $\dot{q}(t)$ traces, one has to evaluate α and k at the average temperature between the initial temperature and the temperature at $(t_{min} + t_{max})/2.$, where t_{min} and t_{max} are the start and end times of the test window. The test time length chosen for this study was 100 μs with the time when the laser is fired t_{fire}, included in the range.

3.6 Pressure measurements

The pressure transducers used for this study are Kulite semiconductor transducers (XCQ-080-500A) chosen for their small size and ease of use. Diagrams showing details of the transducer mountings and the mounting holders are shown in appendix A. The mounting holders are secured to the model with RTV-type silicone sealant and the transducers are fixed into their individual mountings with Loctite 271. Once in their mountings, the pressure transducers are interchangeable for all models. The gages were inspected after every shot to check for clogged holes in the sensitive part and for soot beyond the sensitive area which would indicate a loose transducer which would result in a lower pressure reading. Also, slow rising signals were obtained when the pressure transducers were very tight and not enough gas was in contact with the sensitive area during the test time. In most cases, these signals had to be disregarded since by the time the signal attained a value comparable to their neighboring gages, the test time was over.

The conversion from voltage traces to pressure time histories is much simpler than that to $\dot{q}(t)$ time histories. All one needs is to know the conversion factor from voltage to pressure for each transducers and apply it to the voltage traces. For each gage, there are four leads, two going to a power supply and the other two being for the output signal. All the transducers are connected in parallel to a regulated 10 $\pm$.04 V power supply and they have a common ground.

3.7 Limits of test time

Ideally, the test time for a shock tunnel is ended when the driver gas interface reaches the model. On this topic, one of the most relevant studies to this project is that of Sudani (see Sudani and Hornung (1997); Sudani *et al.* (1998)) on driver gas contamination. He found that for overtailored conditions with $h_o > 12.5\,\mathrm{MJ/kg}$, the test time starts being shorter than that given by the conservative estimate of Davies and Wilson (1969). For higher stagnation enthalpy values, the test time can be practically reduced to zero. On the other hand, the test time can be increased if the tunnel is driven in undertailored mode. Sudani deduced an upper limit for the available test time as a function of h_o for different operational modes. Whether a condition is tailored, undertailored, or overtailored can be checked by inspecting the shape of the P_o traces. Based on these results, some of the shots performed before this information was available had to be repeated and care was taken to attain undertailored conditions for all the remaining high h_o free-stream conditions. The driver gas contamination is not an issue for lower h_o conditions.

Another issue for determining the available test time is to know the time that it takes for the nozzle flow to reach a steady state and then the time that it takes for the flow over the cone to be established and steady. The first time interval has been estimated (see Davis (1998)) to be about

0.4 ms. The second interval has been conservatively estimated to be $\tau = 20L/u_\infty$, where τ is the time needed for steady flow, L is a length of interest, in this case the hypothenuse of the cone, and u_∞ is the free-stream flow velocity. Taking the largest cones and the smallest u_∞ of all conditions, τ is about 0.4 ms, which gives a conservative lower bound for the starting of the test time of about 0.8ms. All pictures are taken after this time. The upper bound of the test time is taken from the estimates of Davies and Wilson (1969) and Sudani and Hornung (1997). The variable named t_{DW} in the appendix D is the estimate from Davies and Wilson (1969) for the useful test time for a given shot.

Chapter 4 Numerical approach

Numerical simulation of the experimental data constitutes an important part of the present project. From the experimental runs, one can only measure a very limited number of variables, like surface pressure and heat flux. The holographic interferograms are mostly a qualitative description of the flow. Therefore, one needs to complement the experimental study with numerical simulations which provide many other physical properties of the flow field, such as density, speed, temperature, and composition. One can validate the numerical method with experimental data and if agreement is found, the numerical method can be applied to conditions not available experimentally. If the two data sets disagree one can learn by finding sources of error either on the numerical or on the experimental methods.

The present chapter briefly describes the main numerical code used. The equations to be solved are listed along with the equations of state and the transport and source terms models used in the code. The boundary conditions are also discussed. Finally the generation of the grid and the initialization of the calculations are described. Comparisons of the computational results with experimental data for both inviscid and viscous flows will be given in chapters 5 and 6.

4.1 Description of numerical method

The present code was obtained from Olejniczak and it is explained in detail in Olejniczak (1997) and Candler (1988). This code is referred to in this document as the nonequilibrium code. It solves the equations of motion for thermochemical nonequilibrium continuum flow for both the viscous (Navier-Stokes equations) and inviscid (Euler equations) cases. It can be used for 2-D or axisymmetric flows. The source terms for chemical reactions and vibrational relaxation processes are derived from microscopic considerations. The rotational energy mode is assumed to be in equilibrium with the translational mode (since it only takes a few collision to reach the new equilibrium mode) and therefore there is only one translational-rotational temperature (which will be referred to as T). A separate vibrational energy equation is solved for each diatomic species and the code uses a separate vibrational temperature (T_{vib}) to characterize the vibrational energy. Ionization and electronic excitation are neglected for this study. The code uses a finite-volume approximation to solve the equations. For the spatial differencing it uses a flux-splitting method from Candler and MacCormack (1991) based on the Steger and Warming approach. This method captures shocks well but it is modified in the boundary layer to avoid excess numerical dissipation. The code advances in time using the implicit and iterative Gauss-Seidel line relaxation method. When a solution does

not change in more than 50 iterations, a steady solution has been achieved and this constitutes the final solution. The code is not time accurate but it is second order accurate in the streamwise and spanwise directions. All calculations done here are for laminar flows. A CRAY J-90 was used for all computations and a typical run with a grid of 100×200 points, would need about 4000 iterations and about 8 hours.

For more than a decade, this code has been succesfully used to model hypervelocity flows. Some examples of the code validation with experimental data can be found in Candler (1988) and Wen and Hornung (1995). For the present study, before performing any experiments, the code was validated against the analytical solutions of Taylor and Maccoll (1933) for frozen flows with attached shocks. The discrepancies with the theoretical results were about 0.2% in the shock angle and about 2% in both the surface Mach number and surface pressure.

4.1.1 Governing equations

The equations of motion solved are summarized below, where the coordinates in this case are x and y corresponding to j=1,2:

- Mass conservation equation for each species, s,

$$\frac{\partial \rho_s}{\partial t} + \frac{\partial}{\partial x_j}\left(\rho_s(u_j + v_{s_j})\right) = w_s \,, \tag{4.1}$$

  where w_s is the production rate for species s due to chemical reactions, u_j is the mixture mass-averaged velocity in the j-direction, and v_{s_j} is the species diffusion velocity in the j-direction, defined as $v_{s_j} = u_{s_j} - u_j$, where u_{s_j} is the species mass-averaged velocity in the j-direction.

- Mass-averaged momentum equations,

$$\frac{\partial}{\partial t}\left(\rho u_i\right) + \frac{\partial}{\partial x_j}\left(\rho u_i u_j + p\delta_{ij}\right) = -\frac{\partial \tau_{ij}}{\partial x_j} \,, \tag{4.2}$$

  where τ_{ij} is the shear stress tensor.

- Vibrational energy equation for each diatomic species,

$$\frac{\partial}{\partial t}\left(\rho_s e_{v_s}\right) + \frac{\partial}{\partial x_j}\left(\rho_s e_{v_s}(u_j + v_{s_j})\right) = -\frac{\partial \dot{q}_{v s_j}}{\partial x_j} + e_{v_s} w_s + Q_{T-v_s} + Q_{v-v_s} \,, \tag{4.3}$$

  where e_{v_s} is the vibrational energy per unit mass of the species s and $\dot{q}_{v s_j}$ is the contribution to heat conduction from the vibrational energy. The last three terms represent source terms; $e_{v_s} w_s$ represents the loss or gain of vibrational energy due to chemical reactions, Q_{T-v_s} arises from the transfer of energy between the translational and vibrational modes, and Q_{v-v_s} represents

the exchange of vibrational energy between the species s and other species. The last term is only relevant for the CO_2 case since for N_2 flows, there is only one diatomic species.

- Total energy equation,

$$\frac{\partial}{\partial t}(\rho e) + \frac{\partial}{\partial x_j}(u_j(\rho e + p)) = -\frac{\partial}{\partial x_j}(\tau_{ij} u_i) - \frac{\partial}{\partial x_j}(\dot{q}_j + \dot{q}_{v_j}) - \frac{\partial}{\partial x_j}\sum_s \rho_s h_s v_{s_j}, \quad (4.4)$$

where $\dot{q}_j$ is the contribution to heat conduction from the translational-rotational energy and h_s is the enthalpy of species s.

The pressure is determined by assuming a mixture of ideal gases,

$$p = \sum_s \rho_s R_s T, \quad (4.5)$$

where R_s is the gas constant for each species, and the enthalpy is given by,

$$h_s = h_s^\circ + e_{tr_s} + p_s/\rho_s + e_{v_s} + e_{r_s}, \quad (4.6)$$

where h_s° is the formation enthalpy, and e_{tr_s} and e_{r_s} are the translational and rotational contributions to the total internal energy respectively. The vibrational energy per mode r is determined by assuming a harmonic oscillator,

$$e_{v_{s,r}} = g_r \frac{R_s \theta_{v_{s,r}}}{\exp\left(\theta_{v_{s,r}}/T_v\right) - 1}, \quad (4.7)$$

where $\theta_{v_{s,r}}$ is a characteristic temperature for molecular vibration and g_r is the degeneracy of the mode r. The total vibrational energy for a species s is the sum of the energy in each mode. For the case of nitrogen flows, there is only one mode of vibrational energy but for CO_2 flows there are three modes and one has a double degeneracy. See appendix B for more details.

The translational-rotational temperature is determined from the total energy expression as follows,

$$\sum_s^n \rho_s c_{v_s} T = \rho e - \frac{1}{2}\rho u_j u_j - \sum_s^m \rho_s e_{v_s} - \sum_s^n \rho_s h_s^\circ, \quad (4.8)$$

where m is the total number of diatomic species present and n is the total number of species considered. The shear stress tensor and heat conduction vectors are given by,

$$\tau_{ij} = -\mu\left(\frac{\partial u_i}{\partial x_j} + \frac{\partial u_j}{\partial x_i}\right) + \frac{2}{3}\mu\frac{\partial u_k}{\partial x_k}\delta_{ij}, \quad (4.9)$$

$$\dot{q}_j = -k\frac{\partial T}{\partial x_j}, \quad \text{and} \quad \dot{q}_{v_j} = -\sum_s \rho_s D_{11_s}\frac{\partial e_{v_s}}{\partial x_j}, \quad (4.10)$$

where μ is the viscosity of the gas mixture, k is the thermal conductivity and D_{11} is the self-diffusion coefficient. The viscosity for each species is calculated using Blottner *et al.* (1971) results. Both the mixture viscosity and thermal conductivity are obtained by using Gupta *et al.* (1990) mixing rule. The self-diffusion coefficients are derived from kinetic theory. For more details on the calculation of the transport coefficients refer to Olejniczak (1997). The constants used in these computations are listed in appendix B.

4.1.2 Source terms

The rate of exchange of energy between the translational and vibrational modes is given by

$$Q_{T-v_s} = \rho_s \frac{e^*_{v_s}(T) - e_{v_s}}{\tau_s}, \tag{4.11}$$

where τ_s is a characteristic relaxation time given by Lee (1985). The rate of exchange of vibrational energy between two species, r and s, is given by,

$$Q_{v-v_{sr}} = P_{sr} Z_{sr} e_{vr}, \tag{4.12}$$

where P_{sr} is the probability of species r transferring vibrational energy to species s, Z_{sr} is the number of s–r collisions per unit time and volume, and e_{vr} is the average vibrational energy per particle of species r. Z_{sr} is determined from kinetic theory (see Vincenti and Kruger (1975)) and P_{sr} is assumed to be constant and equal to .01 which is a valid assumption for $T > 2000K$. The total energy exchange between species s and the other species can be represented as

$$Q_{v-v_s} = \sum_{r \neq s}^{m} Q_{v-v_{sr}} - Q_{v-v_{rs}}. \tag{4.13}$$

For further details in the energy exchange mechanism see Candler (1988). The chemical reactions considered for the nitrogen flows are:

$$\mathrm{N_2 + M} \rightleftarrows \mathrm{2N + M}, \tag{4.14}$$

where M is a third body to assist in the reaction and can be either $\mathrm{N_2}$ or N. On the other hand, the reactions used to describe the flows of CO_2 are:

$$CO_2 + \mathrm{M} \rightleftarrows \mathrm{CO + O + M}, \tag{4.15}$$

$$CO + \mathrm{M} \rightleftarrows \mathrm{C + O + M}, \tag{4.16}$$

$$O_2 + \mathrm{M} \rightleftarrows 2\mathrm{O} + \mathrm{M}\,, \tag{4.17}$$

$$CO_2 + \mathrm{O} \rightleftarrows \mathrm{O}_2 + \mathrm{CO}\,, \tag{4.18}$$

$$CO + \mathrm{O} \rightleftarrows \mathrm{O}_2 + \mathrm{C}\,, \tag{4.19}$$

where M can be different species for the first three reactions as listed in appendix B.

The forward and backward reaction rates, k_{f_M} and k_{b_M}, vary according to the M used in the reaction. The source terms appearing in the mass conservation equations and in the vibrational energy equations are given in terms of these rates. For example, to compute the source term for O_2 we need to compute some reaction rates ($\mathcal{R}$) first,

$$\mathcal{R}_3 = \sum_M \left[-k_{f3_M} \frac{\rho_M}{\mathcal{M}_M} \frac{\rho_{O_2}}{\mathcal{M}_{O_2}} + k_{b3_M} \frac{\rho_M}{\mathcal{M}_M} \left(\frac{\rho_\mathrm{O}}{\mathcal{M}_\mathrm{O}} \right)^2 \right] , \tag{4.20}$$

$$\mathcal{R}_4 = -k_{f4} \frac{\rho_O}{\mathcal{M}_O} \frac{\rho_{CO_2}}{\mathcal{M}_{CO_2}} + k_{b4} \frac{\rho_{CO}}{\mathcal{M}_{CO}} \frac{\rho_{\mathrm{O}_2}}{\mathcal{M}_{\mathrm{O}_2}} , \tag{4.21}$$

$$\mathcal{R}_5 = -k_{f5} \frac{\rho_O}{\mathcal{M}_O} \frac{\rho_{CO}}{\mathcal{M}_{CO}} + k_{b5} \frac{\rho_C}{\mathcal{M}_C} \frac{\rho_{\mathrm{O}_2}}{\mathcal{M}_{\mathrm{O}_2}} , \tag{4.22}$$

where the subindex of $\mathcal{R}$ denotes the number of the reaction and $\mathcal{M}_s$ is the molecular weight of species s. These rates are combined to give the final source term,

$$w_{\mathrm{O}_2} = \mathcal{M}_{O_2} \left(\mathcal{R}_3 - \mathcal{R}_4 - \mathcal{R}_5 \right) . \tag{4.23}$$

The reaction rates are given in Arrhenius form and a modified temperature is used to account for vibration-dissociation coupling (Park (1987)),

$$k_{f_M} = c_{f_M} \left(\sqrt{T T_v} \right)^{\eta_M} \exp\left(-\theta_{d_M} / \sqrt{T T_v} \right) , \tag{4.24}$$

where the constants c_f, η, and θ_d are obtained experimentally by Park (1985). Several sets of constants were tried out but the set given in this reference best fits the experimental results. The constants are listed in appendix B. The forward and backward reaction rates for a given reaction are related to each other through the equilibrium constant, K_{eq}, for the same reaction,

$$K_{eq}(T) = \frac{k_{f_M}(T)}{k_{b_M}(T)} . \tag{4.25}$$

The equilibrium constants are found by curve fits with data from Gupta *et al.* (1990). The backward reaction rate depends only on the translational temperature of the impacting heavy particle and thus K_{eq} and k_{f_M} are evaluated at T.

Note that for the special cases when the code is used to do inviscid calculations, the transport coefficients μ, k, and D_{11} are set to zero. When the code is used for frozen calculations the chemical composition has to remain constant and this is achieved by setting w_s, Q_{T-v_s}, and $Q_{v-v_{sr}}$ to zero.

4.1.3 Boundary conditions

The free-stream conditions for these experiments are calculated using the same code form Olejniczak (1997) for a nozzle flow as described in the next section. The resulting input conditions are conical and supersonic. The outflow boundary is also supersonic, except inside the boundary layer, and a zero-gradient exit condition is applied. The wall is assumed to be isothermal at the average value of the maximum temperature registered in thermocouples during the test time for the given condition and the initial ambient temperature. The wall is also assumed to be non-catalytic, that is, the normal gradient of each species mass concentration at the wall is zero. For the inviscid cases, both the wall and the line of symmetry (nozzle axis) have the same boundary conditions, zero normal pressure gradient and zero normal fluxes of mass, momentum, and energy. In the case of viscous runs, the conditions at the wall are: no-slip velocity condition and zero normal pressure gradient. Also, at the wall, the vibrational temperature is assumed to be in equilibrium with the translational temperature.

4.2 Cone computations

4.2.1 Initialization of computations

The initial conditions for the cone computations are obtained using the code from Olejniczak (1997) but modified to compute conical nozzle flows. The computational domain extends beyond the actual exit plane of the nozzle to cover the location of the grid used for the cone calculations. The computations are viscous with grid points clustered toward the wall. The clustering is not enough to resolve wall fluxes adequately but the viscous computations serve to account for the boundary layer displacement effect. Grid points are also clustered toward both the nozzle centerline and the upstream end of the grid to better resolve the flow in these regions. The upstream and downstream ends of the grid have supersonic inflow and outflow boundary conditions respectively, and the nozzle centerline has a symmetry boundary condition. The boundary conditions for the upstream end of the grid are obtained from SURF (see section 3.3). This program computes an equilibrium solution from the reservoir conditions up to a given point past the throat where the flow is supersonic. The

flow direction at the upstream end of the grid is computed using the angle from the point in question to a point source assuming purely conical flow. The point source is located by extending the conical wall and centerline boundaries of the nozzle grid backwards until they intersect. The accuracy of the nozzle calculations has been discussed by Davis (1998) and he has also given some error bounds for the free-stream conditions calculated (see appendix C).

The data from the symmetry line (nozzle centerline) beyond the nozzle exit plane is used to find second degree polynomial fits for variables needed as input for the cone calculations: speed, vibrational and translational temperature, and density. The independent variable for these fits is the distance to the point source. The coefficients of these fits are input to the cone calculations and the initial conditions at any grid point are calculated by using the distance from the grid point to the point source as the independent variable. The two components of the velocity are computed using the angle from the point source to the grid point in question and assuming a purely conical flow.

4.2.2 Computational grid

Although 24 different grids were used for the different cones, all of them are similar to the one shown in figure 4.1. Almost all the grids for cones with $d = 8\,\text{cm}$ or smaller had 200 points in the direction perpendicular to the body surface (η-direction) and 100 points in the direction along the body (ξ-direction). These numbers were chosen after performing a grid study in which the number of points varied from 80 to 300 in the η-direction and from 100 to 200 in the ξ-direction. For some of the cases with cone half-angles of 56° and 60° it was necessary to use grids of 200×200 points to better resolve the attached shock. For the cones with $d = 16\,\text{cm}$ the grids had 200×200 points. All grids had some stretching toward the wall but the grids used for viscous calculations had a minimum spacing close to the wall in the η-direction of about 0.4×10^{-6} m. The small spacing is needed to resolve more accurately the heat fluxes. None of the grids used for this study had refinement near the shock. The width of the shock in the stagnation streamline, taken as the length that it takes for the density to reach 95% of its final value after the jump across the shock, varied from about 1×10^{-5} m to about 1×10^{-4} m.

4.2.3 Computational interferograms

From the computational results one can also obtain holographic interferograms since the intensity which is recorded in the interferogram can be related to the computed density field. The refractive index for equilibrium or non-equilibrium reacting gases, n, is related to the flow density as follows:

$$n = 1 + \sum_i \kappa_i \rho_i \,, \tag{4.26}$$

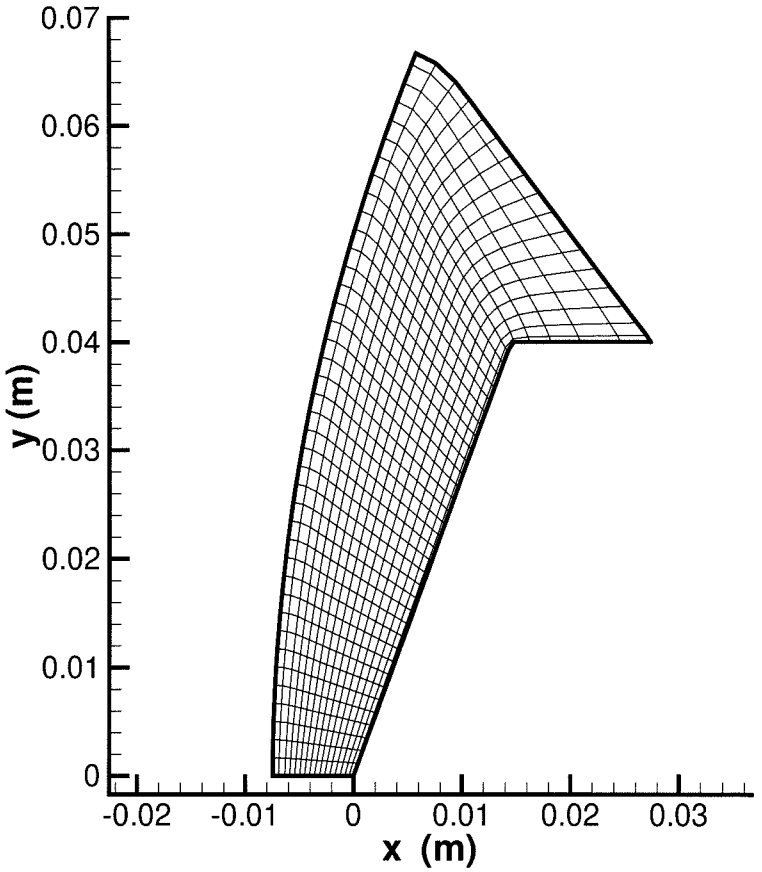

Figure 4.1: Typical computational grid used for the cone flows studied. Only every other fifth point is shown in each direction for better clarity of the diagram.

where κ_i are the Gladstone-Dale constants listed in appendix B. In turn, the phase shift from the no-flow picture to the flow picture is related to the refractive index like,

$$\phi = \frac{2\pi}{\lambda} \int_0^L (n - n_{ref}) dl \,, \tag{4.27}$$

where λ is the wavelength of the laser used to take the interferograms and it is in this case 532 nm for the NdYag laser used. The integration is done along the line of sight of the laser. It is assumed that the line of sight is a straight line perpendicular to the image plane. The diffraction along the model is assumed to be negligible. The free-stream fringes mentioned in section 3.2 introduce an additional phase angle which is computed by measuring the spacing between the fringes, their angle with respect to the cone, and where they intersect the cone. Each set of a dark and light fringe

represents a phase shift of 2π. This phase angle (ϕ_{FS}) is added to the angle computed above. The intensity of the interferograms (I) is computed from the phase shift as follows,

$$I = 4cos^2(\frac{\phi + \phi_{FS}}{2}) . \tag{4.28}$$

Since the grid used for the computations is only 2D, the axisymmetric flow field needed to compute the interferograms is obtained by rotating the grid by 90 degrees around the x-axis. The laser beam path is integrated along the z-axis.

4.2.4 Amrita

While most of the computations presented in this thesis were performed using the above described code, some calculations to be described in section 5.1 were performed using Amrita. Amrita is a complex software system designed by James Quirk (for a detailed explanation of the system see Quirk (1998)) to automate numerical investigations. At the time of this printing, Amrita could only be used for frozen flows. The free-stream conditions used as input for the Amrita calculations are plane and not conical like in the case of the nonequilibrium computations. Amrita takes as input the free-stream Mach number and an effective γ to characterize the gas. One of the key advantages of Amrita is that it can use adaptive mesh refinement which resolves shocks better than traditional fixed grids. You also have the flexibility to choose the solver you want to employ for a particular case and the grid you want to use. For the cases run here, a flux-limited, operator split, Roe solver was used. The grids used had 120×200 points and two tiers of a factor of three were performed for the refinement. This gives and effective 1080×1800 number of cells.

Chapter 5 Field results: interferograms and detachment distance

In this chapter the behavior of the sonic line from incipient to full detachment, obtained from numerical simulations, is compared with the theoretical considerations of chapter 2. Several numerical contour plots of key field variables, such as Mach number and density, are presented. The experimental interferograms and their numerical counterparts are discussed next. The rest of the chapter presents experimental and numerical data for non-dimensional detachment distance and its dependence on the cone half-angle. These plots are compared with the theoretical model of chapter 2. Numerical calculations, from the frozen to the equilibrium limits, performed to complement the experimental data are also discussed.

5.1 Sonic line behavior from attached to detached conditions

Figures 5.1 through 5.2 show the evolution of the sonic line, and the subsonic region contained within it, for frozen flows from attached conditions to full detachment. Refer to section 2.1 for the theoretical model of the growth of the sonic line. The present figures were computed using Amrita (see section 4.2.4) with free-stream conditions comparable to condition N_2 4. The computations are inviscid in all cases. In these figures the white lines represent regions where M-1 changes sign. At some of these conditions the shock layer Mach number differs so little from 1 that the "sonic line" does not always appear as a single smooth curve.

When the flow is supersonic throughout the shock layer, the sonic line is inside the boundary layer. (This case will be discussed in more detail in section 6.2 where it will be related to the heat flux near the corner of the cone). As the cone half-angle increases, in this case to $\theta = 52.9°$ (see figure 5.1-A), a subsonic layer appears, starting from the tip, as seen by the small white region close to the cone apex. In the next figure we start to see the sonic line growing along the length of the cone and to a lesser degree toward the shock. The growth in both directions of the sonic line was noted in section 2.1.2. An increase of 0.2° in the angle to $\theta = 53.4°$ (figure 5.1-C) produces a dramatic change in the sonic line. Now the subsonic region covers most of the shock layer from the tip to the corner expansion. However, as long as the sonic line does not reach the corner, the information about the size of the cone cannot be transmitted back to its tip. This translates into an attached shock as seen for the case with $\theta = 53.8°$. The first two cases in figure 5.2 correspond to incipient detachment. The sonic line has reached both the shock and the corner of the cone. These

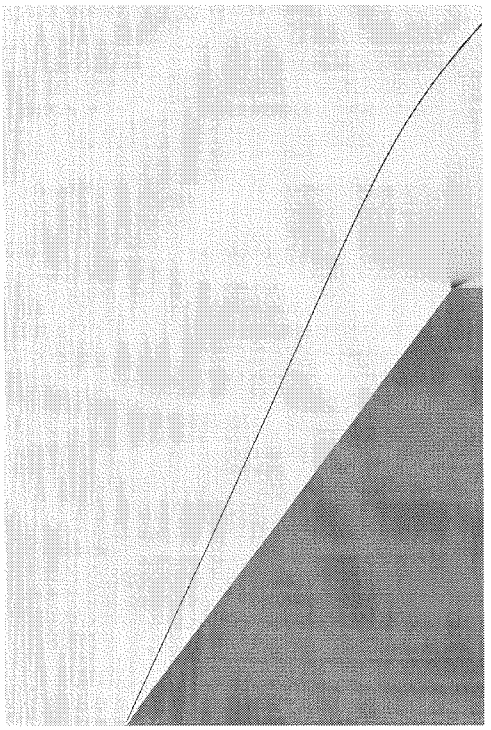

A. $\theta = 52.9°$ $M = 5.89$ $\gamma = 1.4$

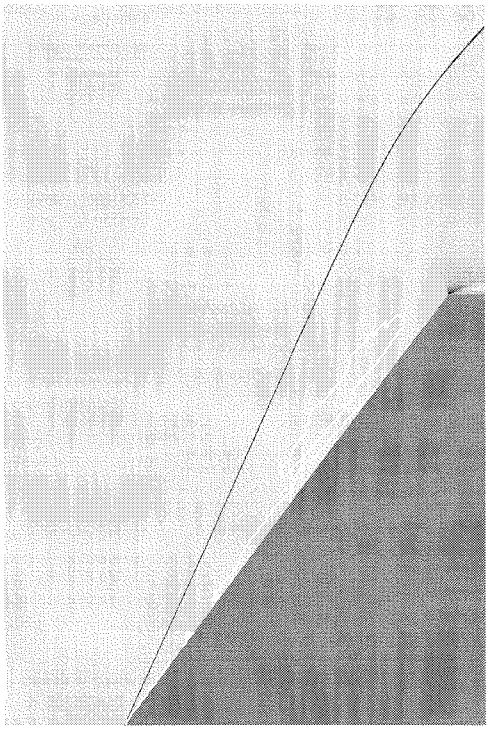

B. $\theta = 53.2°$ $M = 5.89$ $\gamma = 1.4$

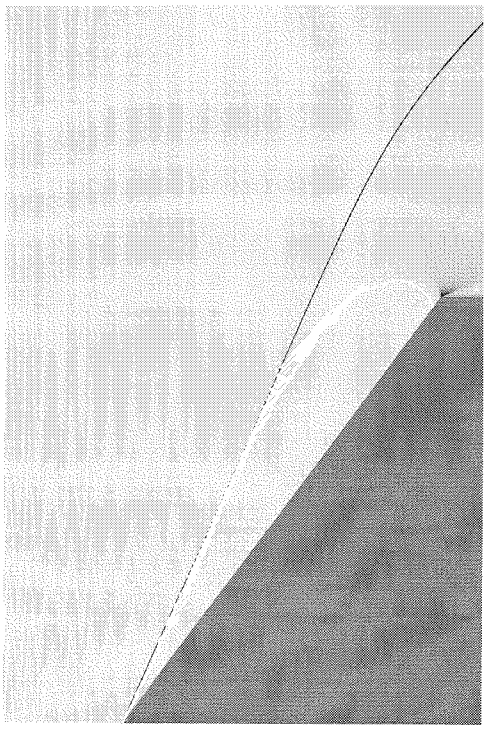

C. $\theta = 53.4°$ $M = 5.89$ $\gamma = 1.4$

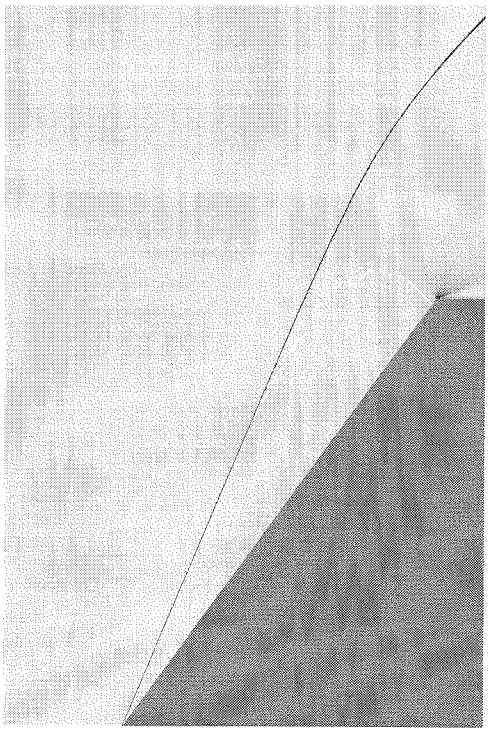

D. $\theta = 53.8°$ $M = 5.89$ $\gamma = 1.4$

Figure 5.1: Evolution of sonic line from attached shock conditions to incipient detachment. The calculations are inviscid and performed with Amrita.

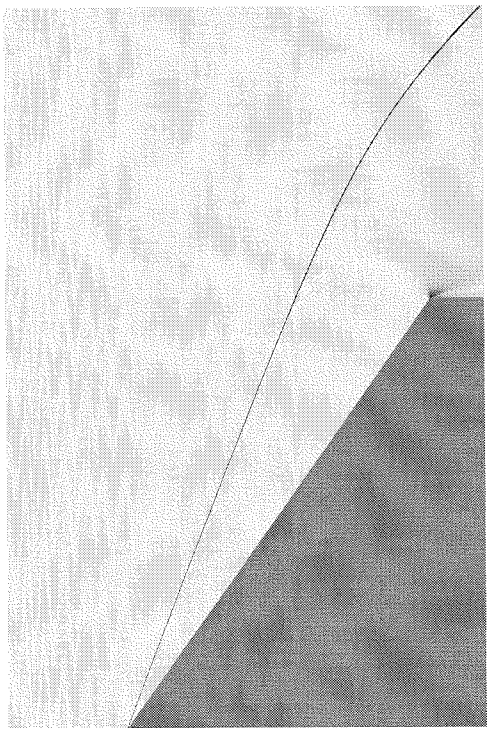

A. $\theta = 54.5°$ $M = 5.89$ $\gamma = 1.4$

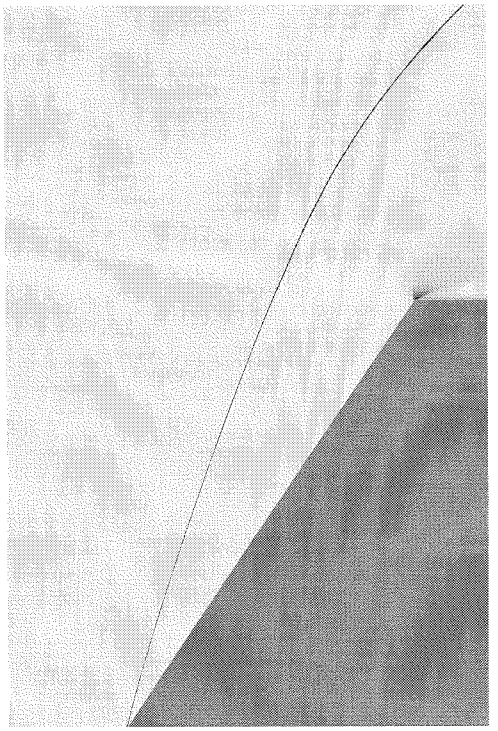

B. $\theta = 56.0°$ $M = 5.89$ $\gamma = 1.4$

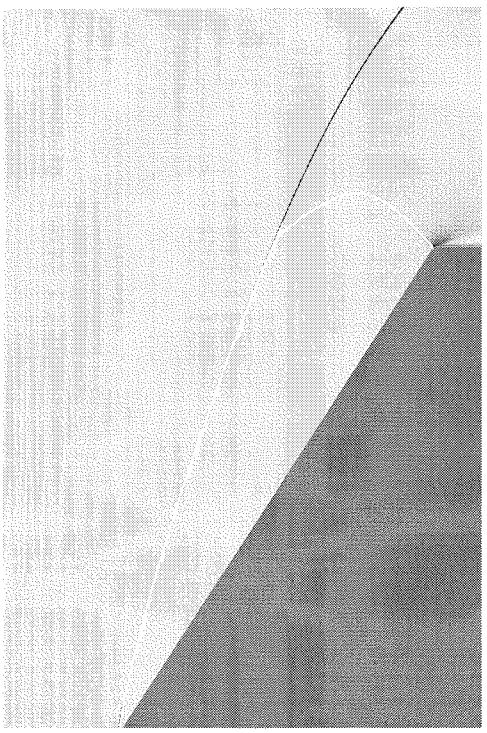

C. $\theta = 57.0°$ $M = 5.89$ $\gamma = 1.4$

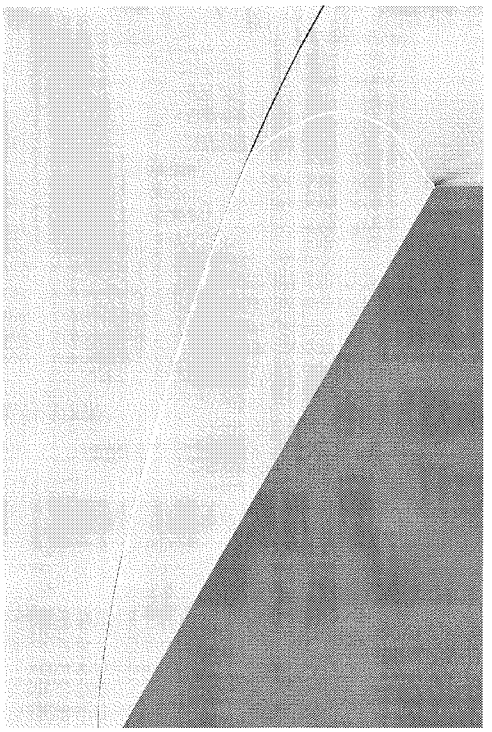

D. $\theta = 60.0°$ $M = 5.89$ $\gamma = 1.4$

Figure 5.2: Evolution of sonic line from attached shock conditions to incipient detachment. Cont'd.

conditions are necessary for the shock to start detaching. However, observe that the transition from incipient detachment to full detachment is not immediate. In this case this transition occurs between $\theta \approx 54.5°$ to $\theta \approx 57°$. The last two pictures of this figure show two examples of detached shocks. Observe that in these cases the shock is normal to the cone at the tip.

5.2 Contour plots of density and Mach number

One of the advantages of CFD is that one can solve for all the variables of interest throughout the shock layer, which is not possible experimentally with current hypervelocity shock tunnel instrumentation and flow visualization techniques. Having already pointed out the importance of tracking the sonic line for the cases studied, figure 5.3-A shows an example of a Mach number contour plot for a nonequilibrium calculation. The calculations in this case are viscous and performed with the code from Olejniczak (1997) and Candler (1988). For these conditions the shock is fully detached, and since the cone-half angle is beyond the critical detachment angle for equilibrium conditions (see section 2.1) the sonic line is at the corner of the cone and has the expected shape. Although not very clear from the picture, the sonic line bends up as it approaches the cone and reaches the corner of the cone. Another very important variable to track is the density. Figure 5.3-B shows the density contours for the same free-stream condition. This information is important since from the density field one can compute numerical interferograms as mentioned in section 4.2.3. Notice how the density is higher closer to the surface (since the flow decelerates as it approaches the cone surface) but decreases as the flow turns around the corner in an expansion.

5.3 Experimental and computational interferograms

The experimental interferogram of the same run presented in section 5.2 is shown in figure 5.4-A. In this case, the cone ($d = 4\,\text{cm}$) fits completely in the field of view and one can see the black shadow of its silhouette. On close inspection, one finds that the fringe distribution is asymmetric, with more dark fringes in the upper half than in the lower one. Also, the first dark fringe is closer to the surface in the upper half than in the lower half. This asymmetry was a recurrent feature in the shots performed for this study. Comparing this experimental interferogram with its numerical counterpart (see figure 5.4-B), one notices that the latter is symmetrical as one would expect since the flow is axisymmetric both at the exit-plane of the nozzle and around the cone. The apparent contradiction is resolved by taking into account the free-stream fringes shown in figure 5.4-C. These fringes, as discussed in section 3.2, are the result of mechanical displacement of the apparatus occurring in the time interval between taking the two pictures needed for the holograms. When the free-stream fringe distribution is subtracted (see figure 5.4-C) the agreement between the computed and the

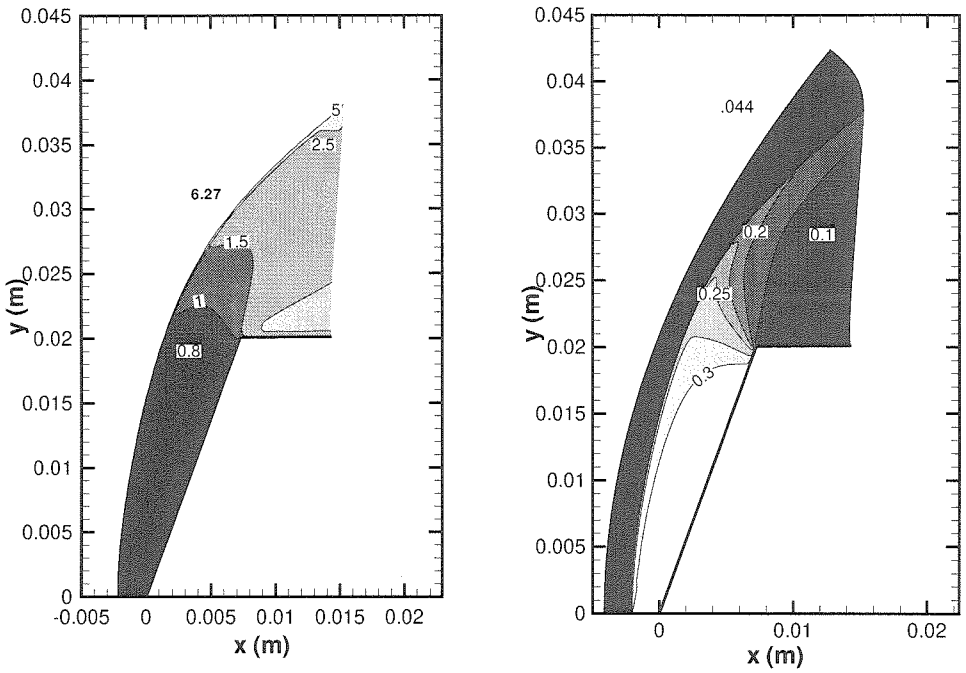

A. Mach contours.

B. Density contours.

Figure 5.3: Mach and density contours for shot 1653. Condition N_2 2: $P_o = 53.9$MPa, $h_o = 10.3$MJ/kg. The calculations are viscous and were performed using the nonequilibrium code.

experimental interferograms is significantly improved. The superposition of the free-stream fringes and the shock layer fringes makes the number of fringes in the shock layer increase which brings the numerical interferogram into close agreement with the experimental one. When incorporating the free-stream fringes into the computed interferograms, there is an initial uncertainty about the sign of the extra phase angle provided by the free-stream fringes. This uncertainty is resolved since only one sign gives the correct shape of the fringes in the vicinity of the corners of the cone. Compare figures 5.4-C and 5.4-D and notice the flip-flop of the shape of the fringes in the corners of the cone between the two figures. Only figure 5.4-C matches the geometry of figure 5.4-A.

Figure 5.5 shows another pair of experimental and computed interferograms. This interferogram is also obtained from the numerical simulation of the density field obtained with the nonequilibrium code. In this case, the computations are inviscid. Since this cone is bigger than the last ($d = 8$ cm) only half of it fits in the field of view and one cannot distinguish signs of asymmetry. However, based on the results discussed above, the free-stream fringes have been included in figure 5.5-B. This free-stream condition has a higher h_o than the conditions for the previous pair but the agreement is still good between the two figures. The flow fields agree qualitatively in the shape of fringes in the shock layer. Both pictures show a straight shock until the corner expansion which is what we

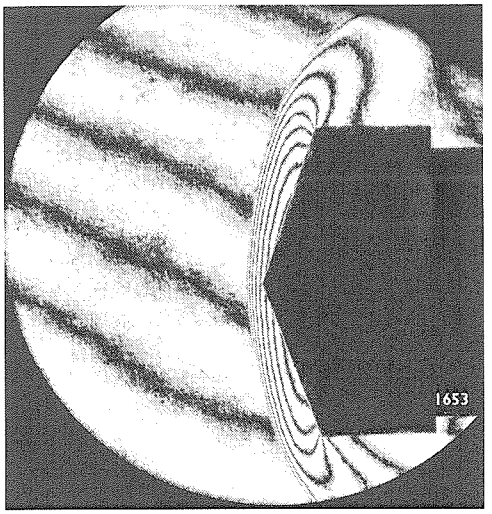

A. Experimental interferogram.

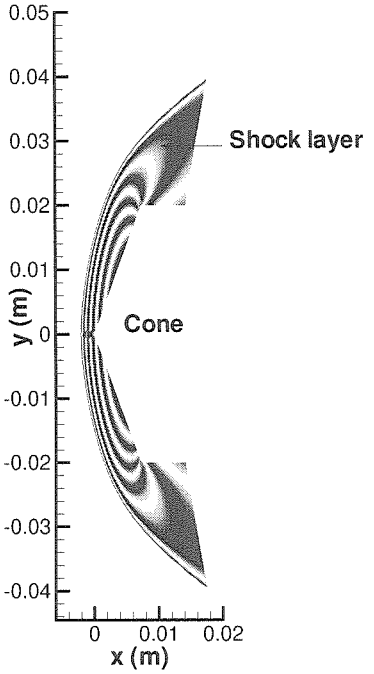

B. Computational interferogram not including free-stream fringes.

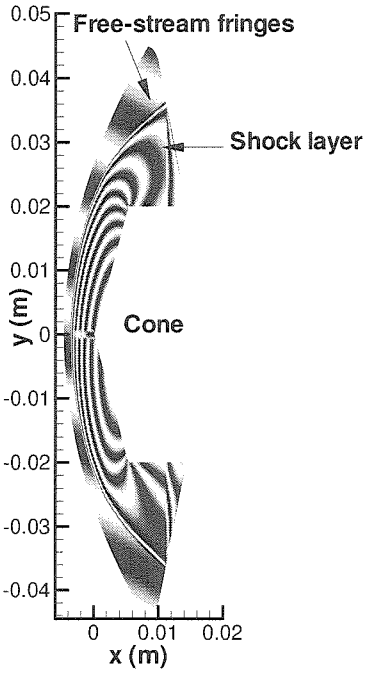

C. Computational interferogram including free-stream fringes.

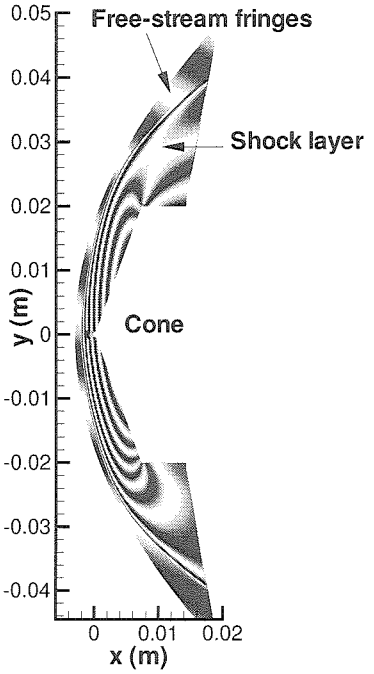

D. Computational interferogram with wrong sign for free-stream fringes.

Figure 5.4: Comparison of experimental and computational interferograms for shot 1653. Condition N_2 2: $P_o = 53.9$MPa, $h_o = 10.3$MJ/kg, $\theta = 70°$, $d = 4$cm. These computations were performed with the nonequilibrium code.

expect for the fully attached case. The discrepancy in the shock angle between the figures is about 0.4°. Since the number of fringes in the interferogram is directly proportional to the free-stream density, the ratio of the number of experimental to computational fringes can give us an estimate of the error in the density used to perform the numerical calculations. In this case, the experimental interferogram has nine dark fringes in the shock layer while the computational one has only eight. If the density were the only source of this error, this would mean that the free-stream density is underpredicted by 12% in the computational case.

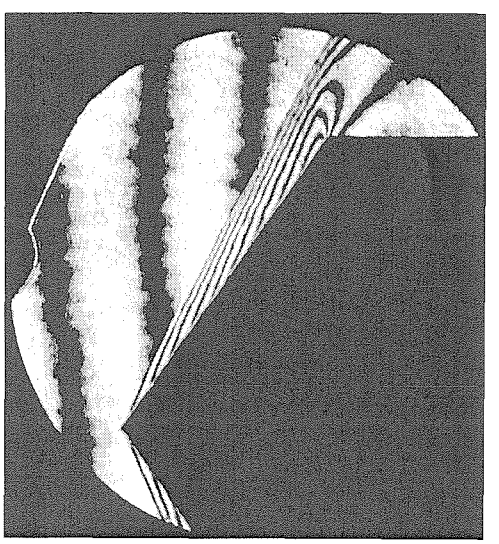

A. Experimental interferogram.

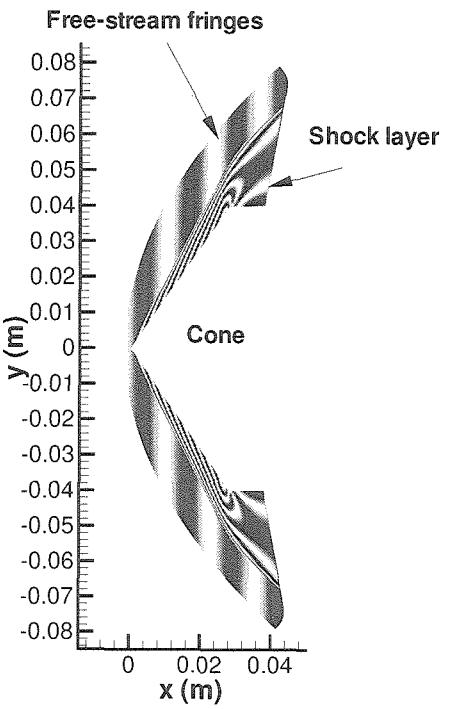

B. Computational interferogram including free-stream fringes.

Figure 5.5: Comparison of experimental and computational interferograms for shot 1500. Condition N_2 1: $P_o = 53.6$MPa, $h_o = 18.2$MJ/kg, $\theta = 55°$, $d = 8$ cm. The computational interferogram was obtained using the nonequilibrium code

5.4 Dependency of the detachment distance growth on the cone half-angle for different regimes of thermochemical-nonequilibrium

This section will present the experimental counterpart to the theoretical predictions of section 2.1, especially to figure 2.8.

5.4.1 Nitrogen flows

An explanation is due for the notation employed in the labels for all the figures presented in this section. The first letter refers to the test gas used (N_2 or CO_2), the first number is the condition number, the third number is the diameter of the cone in cm. For the case of frozen flows, the diameter is not important and it is omitted from the notation. The letter "c" indicates that the data point is obtained from the nonequilibrium numerical code. The letter "f" indicates frozen flow and "e" equilibrium flow. All the filled symbols denote experimental points. The curves joining the experimental points are fits of the form $y = A(x-a)^2 + B(x-a)^3$ where a is the $x-$intercept. They are presented to aid the eye in distinguishing each curve.

Since no runs were made with frozen or equilibrium conditions in this study, all the information gathered about these flows comes from computations performed using the nonequilibrium code, which can also be used to do frozen computations as stated in section 4.1.2. In the particular case of N_2 4 some calculations for the frozen limit were performed using Amrita to compare the results obtained from two independent numerical codes. Only representative experimental runs were chosen to be simulated numerically because each nonequilibrium CFD run could take days on the Cray to be completed. Most of the computational points presented here are from inviscid calculations. It was found, however, that whether the calculation was viscous or inviscid did not affect the detachment distance. This is to be expected since for the fully detached cases the ratio of the detachment distance to the boundary layer thickness is much bigger than one. It varies from 25 to about 70 depending on the cone half-angle and free-stream condition. All the numerical data obtained for this study are presented in the plots that follow.

The first figure in this section, figure 5.6, is for a condition of low stagnation pressure and low stagnation enthalpy. The line "n4f" is a linear fit to the data obtained with the nonequilibrium code. The fact that the CFD points are well approximated by the linear fit confirms previous experimental results that found linear growth for the detachment distance for frozen flows (Ward and Pugh (1968)). This result is also confirmed with the computations done using Amrita (curve "n4fa"). These computations also serve as an independent validation to the nonequilibrium CFD results. The discrepancy between both computations comes mainly from the uncertainty in the

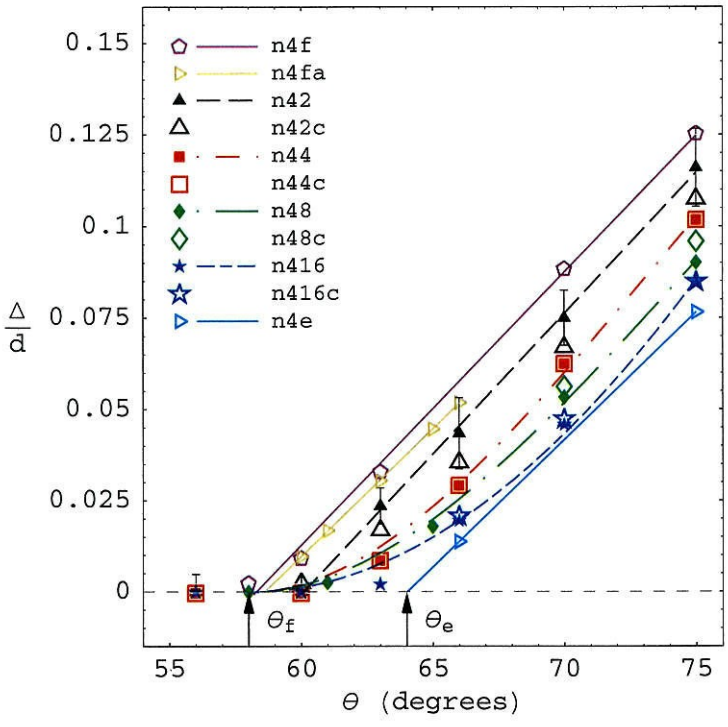

Figure 5.6: Non-dimensional detachment distance for condition N_2 4: P_o = 28.2MPa, h_o = 9.20MJ/kg. Filled symbols denote experimental data and hollow symbols denote computational results. The three straight lines are linear fits to the computational data while the rest of the curves are cubic fits to the experimental data.

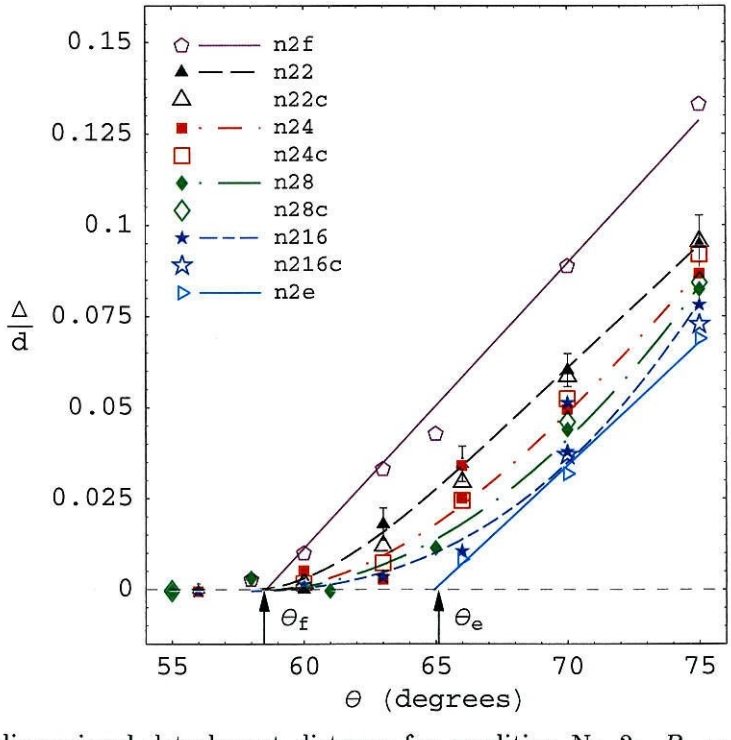

Figure 5.7: Non-dimensional detachment distance for condition N_2 2: P_o = 53.9MPa, h_o = 10.3MJ/kg. Filled symbols denote experimental data and hollow symbols denote computational results. The two straight lines are linear fits to the computational data while the rest of the curves are cubic fits to the experimental data.

effective γ used to characterize the free-stream condition and given as an input to the Amrita calculations. There is also some discrepancy due to the fact that the Amrita calculations do not take into account the conical nature of the free-stream flow. Conical free-stream conditions result in smaller detachment distances for the same cone half-angle and free-stream condition. Since in this case, the Amrita calculations give lower values of detachment distance, we conclude that the disagreement between the two codes comes mainly from the uncertainty on γ.

The point denoted θ_f is the critical angle for detachment in frozen flow. Taylor and Maccoll (1933) predict its value to be about 55.5°. The difference is attributed to the behavior of the sonic line discussed in sections 2.1 and 5.1. We expect that for a given set of angles, as the cone diameter is decreased the curve corresponding to the smallest diameter is closest to the frozen line. This is exactly what happens in figure 5.6. The curve "n42" is closest to the frozen line while "n416" is farthest away. Furthermore, "n42" is almost a frozen flow as revealed by the linear behavior of the curve and by the fact that the linear fit is good all the way to incipient detachment. The error bars presented for this curve are representative for all shots and are due to the inaccuracy of measuring the detachment distance off the experimental interferograms and to the uncertainties in the free-stream conditions as explained in appendix C. Table 5.1 presents several examples of the nondimensional vibrational and chemical relaxation lengths, l_v/d and l_c/d respectively, for several cone diameters, half-angles, and free-stream conditions. This is to give the reader an idea of the order of magnitude of these parameters for the cases studied here.

Condition	d (cm)	θ (degrees)	Stagnation streamline		Streamline entering shock layer at $y = d/2$	
			l_v/d	l_c/d	l_v/d	l_c/d
N_2 2	2	70	.023	-	.041	.54
N_2 2	4	70	.013	-	.015	.23
N_2 2	16	70	.036	-	.023	.15
N_2 3	2	75	.019	-	.025	.22
N_2 3	16	75	.0046	-	.0056	.14
N_2 4	16	70	.0096	-	.014	.22
N_2 4	16	75	.010	-	.012	.21

Table 5.1: Sample values for vibrational (l_v) and chemical (l_c) relaxation lengths. The vibrational relaxation length is measured to the point of thermal equilibrium. The chemical relaxation length is measured until the composition reaches a plateau value. The symbol - means that the chemical relaxation length is bigger than the detachment distance at the stagnation streamline

Notice the close agreement between the computational and experimental values for "n44" and "n44c". The discrepancy in Δ/d between experiment and computation is between $6 - 10\%$ with the computational values falling below the experimental values in most cases. The smaller value of the nonequilibrium CFD detachment distance could indicate that the actual free-stream condition has a lower density than the one used for the computations. However, even for the curves "n42" and "n42c" where the disagreement seems to be the greatest, the discrepancy between the two curves is about 10%. The shape of the curves is as expected, with the "n42" having the fastest rise since it is closest to the frozen limit, and as we advance from "n44" through "n416" the curves "hug" the θ-axis for a larger interval of angles before having an appreciable detachment distance.

Now keep h_o approximately constant and see what happens as P_o increases. A priori, we expect that for the same cone diameter, the curves corresponding to the higher P_o will be closer to the equilibrium limit. A higher P_o translates into higher ρ_∞ which makes the chemical reactions happen faster and so pushes all curves closer to the equilibrium limit. Upon close examination of figure 5.7 we find that this is the case. The curve "n22" is not only farther away from the frozen line than before but its shape has changed from almost linear to a more strongly curved contour typical of nonequilibrium flows. Observe the close agreement between computations and experiments in this case as well. The biggest discrepancy is for the smaller cone half-angle cones in "n22". For this cone diameter, the shapes of the nonequilibrium CFD and experimental curves disagree. The disagreement points to discrepancies in the chemical rates since the experimental points seem to be closer to the frozen limit than their CFD counterparts. Finally, note that θ_f has not changed significantly from the last figure.

Now increase h_o and keep P_o the same. The results are shown in figure 5.8. As expected, a

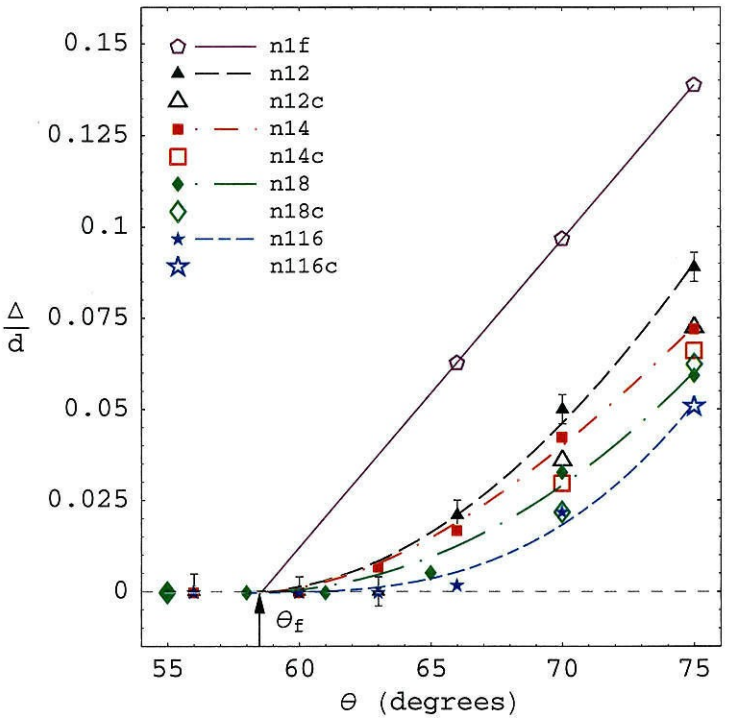

Figure 5.8: Non-dimensional detachment distance for condition N_2 1. P_o = 53.6MPa, h_o = 18.2MJ/kg. Filled symbols denote experimental data and hollow symbols denote computational results. The straight line is a linear fit to the computational data for the frozen case while the rest of the curves are cubic fits to the experimental data.

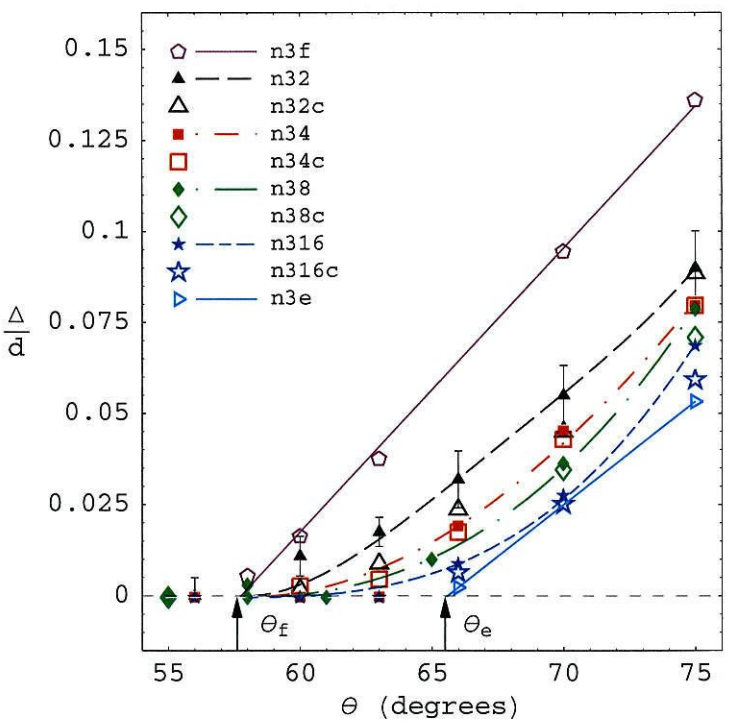

Figure 5.9: Non-dimensional detachment distance for condition N_2 3. P_o = 20.3MPa, h_o = 16.3MJ/kg. Filled symbols denote experimental data and hollow symbols denote computational results. The two straight lines are linear fits to the computational data while the rest of the curves are cubic fits to the experimental data.

higher h_o results in higher T_o which in turns gives a higher temperature at the shock. This means that the rates for the chemical reaction are even faster than for the last condition. The curves, then, are correspondingly closer to equilibrium than their previous counterparts. In this example, the slow rise of the detachment distance as the cone diameter is increased is more dramatic than in the previous cases. This condition suffered from the worst disagreement for the detachment distance between computations and experiments. The disagreement is attributed to test gas contamination. At this high enthalpy, as discussed in section 3.7 the test time is sometimes reduced to less than 0.8 ms, upon arrival of the test gas to the model, if the tunnel is driven in overtailored mode. This translates in a window of less than 0.1 ms to take a clean picture since it takes about 0.7 ms for the shock to be steady. The shots suspected of contamination are marked in appendix D.

Finally, decreasing P_o while retaining about the same high h_o results in a lower ρ_∞ and slower chemical reactions. The resulting figure 5.9 shows the effect in the shape of "n32", for example, which has a faster rise than "n12". Note, however, that this condition still has faster chemical rates than that depicted in figure 5.6 as seen by the slower rise of the curve "n316" than that for "n416". In general, notice how for the four conditions studied, the critical frozen detachment angle θ_f is about constant as is the slope of the frozen lines.

5.4.2 Carbon dioxide flows

The results obtained with the two different free-stream conditions chosen for CO_2 as the test gas are presented in this section. Figures 5.10 and 5.11 show the detachment distance behavior for both conditions. The computations in this case were made using the original code from Candler (see Candler (1988)) modified for CO_2. This code can also be used for frozen flows. The computations for CO_2 were not as successful as those for N_2. The computational model for CO_2 assumes the gas to be in thermal equilibrium and so any effects due to vibrational nonequilibrium are not taken into account. Also, there is only one vibrational temperature for all the diatomic species. The reaction rates for the chemical reactions of CO_2 are not as well known as those for N_2 and this translates into another source of error. In order for the computations to be more accurate, it is necessary to take into account the four different vibrational temperatures involved in CO_2 chemistry. We also need to have a separate nozzle flow program, like the one available for N_2, to calculate the free-stream conditions taking into account the different temperatures, and the conical nature of the free-stream flow. Finally, we need more accurate rates for the dominant chemical reactions.

A few numerical results are shown in figure 5.10. The discrepancies are biggest for the smallest cones. The computational runs for "c24c" and "c28c" are in better agreement with the experimental values. No CFD points are shown in figure 5.11 since the discrepancies in this case went from 40–50%. The numerical results for the frozen limit do not suffer from the limitations cited above as there is no chemistry nor vibrational relaxation involved in this case. They serve as an upper bound to

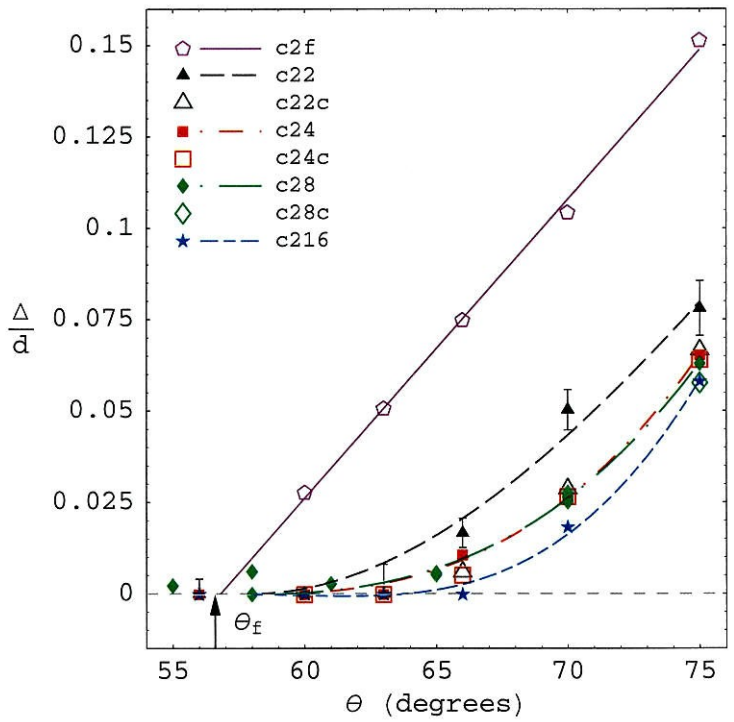

Figure 5.10: Non-dimensional detachment distance for condition CO_2 2: P_o = 24.5MPa, h_o = 6.62MJ/kg. Filled symbols denote experimental data and hollow symbols denote computational results. The straight line is a linear fit to the computational data for the frozen case while the rest of the curves are cubic fits to the experimental data.

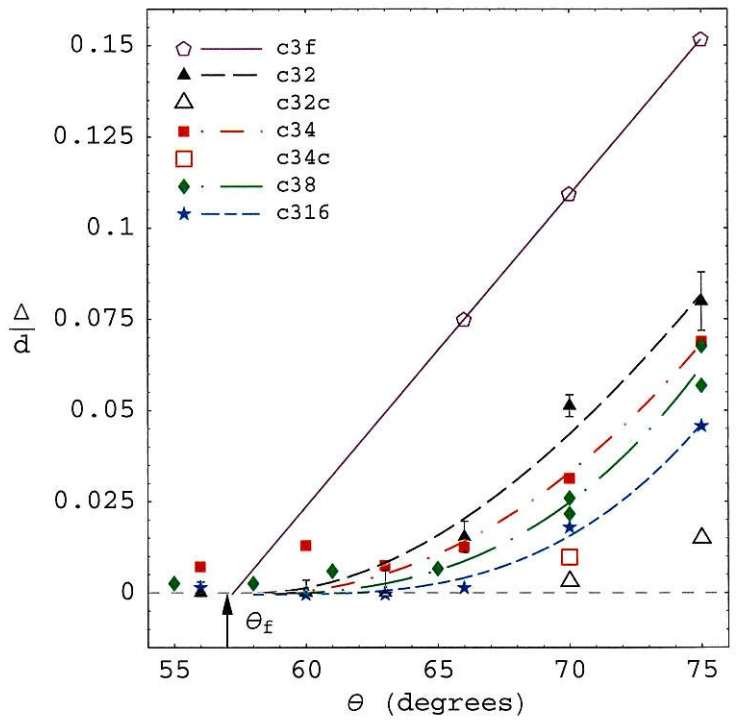

Figure 5.11: Non-dimensional detachment distance for condition CO_2 3: P_o = 64.7MPa, h_o = 9.13MJ/kg. Filled symbols denote experimental data and hollow symbols denote computational results. The straight line is a linear fit to the computational data for the frozen case while the rest of the curves are cubic fits to the experimental data.

the growth rate of the detachment distance and for the detachment distance itself for a given angle. Notice that for figure 5.10 all the experimental curves are close to equilibrium. They follow the same trend as expected, the curves for the smallest cones have largest detachment distances and as the diameter is increased the growth rates and the detachment distances decrease. The error bars shown for the CO_2 cases are only from the error in reading the detachment distance off the interferograms. There were not enough numerical calculations to make a detailed study of the impact of the error in the free-stream conditions in the detachment distance.

5.5 Equilibrium calculations

The numerical code from Olejniczak (1997) and Candler (1988) for N_2 flows is designed for frozen and nonequilibrium calculations. One way to obtain results approximating the equilibrium limit is to steadily increase the constants in front of the exponential and T terms in equation 4.24. The calculation is started with the normal constants and run until it reaches convergence. Next, the constants are increased 5–6 times in a single run. The calculation is run until convergence is achieved. The process is repeated until the detachment distance reaches a constant value or the equilibrium value. The process can also be used in the reverse mode to obtain frozen calculations if the constants are decreased instead of increased. It was found that the plateau detachment distance found for the frozen calculations performed this way was smaller than the detachment distance obtained starting with a frozen calculation. This is because in the proper frozen calculations, the vibrational temperature and chemical composition are frozen throughout the flow. When the constants are decreased, on the other hand, the vibrational temperature increases after the shock and some dissociation does occur resulting in a smaller detachment distance. For this equilibrium study, all the computations were inviscid. Refer back to figure 5.7 and concentrate on "n2e". In this case, the equilibrium calculations were performed on a $d = 16\,\text{cm}$ cone. In section 2.1.5 we inferred the linear behavior of this curve from previous observations in the frozen case and noting that the frozen and equilibrium cases should be similar since they both have the same important length scales. Such predictions are confirmed numerically for the first time, to the author's knowledge, in figure 5.7 where the curve labelled "n2e" is a straight line. Observe that the frozen and equilibrium lines are an envelope for the nonequilibrium curves as expected. Also note the two different critical detachment angles for the frozen and equilibrium cases (θ_f and θ_e respectively). Their difference being about 6° in this case. Calculating this equilibrium curve also showed that the slope of the two straight lines is not the same. There is really no reason for them to be the same, the only feature that we could conclude a priori is that both the frozen and equilibrium curves should be straight lines. Another interesting feature that we can check is dependency of the separation of θ_f and θ_e on h_o. In fact, from the three figures with equilibrium calculations (figures 5.6,5.7, and 5.9) we can see

that the separation is smallest for the condition for with lowest h_o (N_2 4) and highest for N_2 3 which has the biggest h_o. The angles θ_f and θ_e move to the left and right respectively as we increase the h_o of the free-stream condition.

Now consider the behavior of the detachment distance for the same angle as the flow goes from the frozen to the equilibrium limits in N_2 flows. So far we have looked at the detachment distance as a function of the cone half-angle for different diameters. There are two ways to go from the frozen to the equilibrium limits. The first one is, for the same free-stream condition and a reference cone diameter, to decrease the diameter until we reach the frozen limit and then to increase the diameter until we reach the equilibrium limit. The other way is to change the reaction constants as described before. Figures 5.12 and 5.14 through 5.16 are a compilation of the results obtained by both methods for different free-stream conditions and cone half-angles. The curves joining the computational points are fits of the form $y = A+B\arctan(cx+d)$ and they work remarkable well for all the curves presented here. The label CFD refers to the numerical calculations performed with the nonequilibrium code. In all of these figures, the x-axis is a new variable, the reaction rate parameter Ω, which quantifies the degree of nonequilibrium of a given flow. Wen and Hornung (1995) define the reaction rate parameter as,

$$\Omega \equiv -\frac{d}{\rho_s u_\infty}\left(\frac{1}{h_\rho}\sum_{i=2}^{n} h_{c_i}\frac{dc_i}{dt}\right)_s , \tag{5.1}$$

where c_i is the mass fraction of species i, the subscript s denotes conditions immediately after the shock, and the subscripts of h mean partial differentiation with respect to that variable. For a given gas mixture, Ω can be approximated as,

$$\Omega \sim \frac{\rho_s d\left(\sum_{i=2}^{n} h_{c_i}\frac{dc_i}{dt}\right)_s}{\rho_\infty u_\infty^3} . \tag{5.2}$$

This dimensionless number measures the ratio of the energy absorption rate by chemistry to the input rate of free-stream kinetic energy. When Ω is infinity we have equilibrium flows and when it is zero we have frozen flows. In this sense it is similar to the ratio l/d used previously. For the case of N_2 flows, we can use the ideal dissociating gas model (Vincenti and Kruger, 1975) to evaluate the terms in this equation. The expression for Ω becomes,

$$\Omega \sim \frac{\rho_s d\left(\frac{\partial h}{\partial \alpha}\frac{d\alpha}{dt}\right)_s}{\rho_\infty u_\infty^3} , \tag{5.3}$$

where α is the mass fraction of dissociating gas (N) and the expression for the enthalpy is,

$$h = \frac{k}{2m}\left[(4+\alpha)T + \alpha\theta_d\right] . \tag{5.4}$$

Combining this expression and the modified Arrhenius equation (4.24) evaluated only at the translational temperature immediately after the shock, we can evaluate Ω for all the computations performed. The experimental data is normalized by the values obtained from the computations performed for the same free-stream condition and cone half-angle with the standard Park 85 rates.

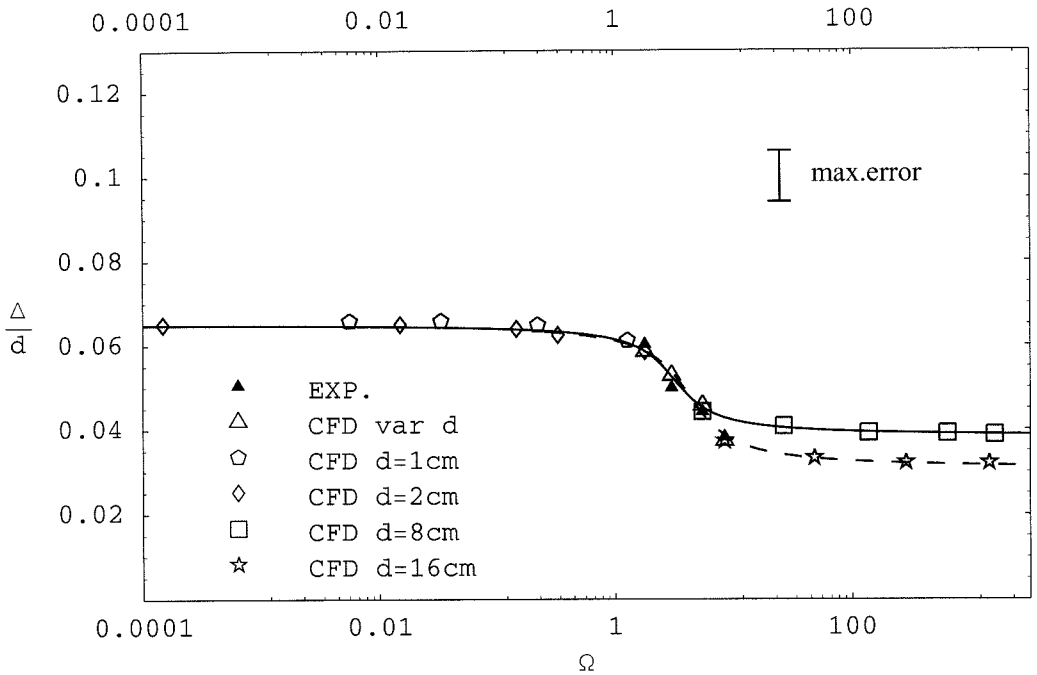

Figure 5.12: Non-dimensional detachment distance from frozen to equilibrium limits for condition N_2 2: $P_o = 53.9$MPa, $h_o = 10.3$MJ/kg, $\theta = 70°$.

In figure 5.12, the curve "CFD d=2cm" is obtained by taking as initial condition the calculation corresponding to this free-stream condition with $d = 2$ cm. Then, the constant k for each reaction is reduced until a plateau is reached. This plateau is a graphical demonstration of the relation $\Delta = O(d)$ for the frozen case where k (or Ω) tends to zero. However, note that this value of $\Delta/d \approx .065$ is lower than the value obtained with proper frozen calculations which is $\Delta/d = .089$. As explained before this difference is due to the finite (although slow) reaction rates and to the fact that the vibrational temperature is not frozen throughout the flow field. Notice that if we reduce the diameter of the cone (see "CFD d=1cm") we obtain larger detachment distance but still cannot reproduce the values of truly frozen calculations. The points in "CFD variable d" are the computed values for the experimental runs represented in "EXP". For these runs, the free-stream conditions are the same, including the rate constants, but the diameter is different. The curve "CFD d=8cm" is obtained by taking as reference the numerical solution for $d = 8$ cm and then increasing the rate constants. Similarly, in "CFD d=16cm", the calculations for the case with $d = 16$ cm are taken as

the reference and the constants are increased until a plateau is reached. The error bars shown in the graph represent the uncertainty in the rate constants due to the uncertainty in the free-stream conditions (see appendix C).

At first glimpse, it would seem that this nonequilibrium process exhibits binary scaling (Anderson (1989)). For N_2 flows, we have a two-body reaction process for dissociation and a three-body process for recombination. For the free-stream conditions used here, the ratio of the dissociation to the recombination reaction rates varies from $500 - 5000$. That is, dissociation is the dominant reaction and we can treat this problem as a two-body process. For binary processes (Hornung (1996)) the reaction rate is proportional to the free-stream density which after some algebraic manipulation translates to the binary scaling parameter,

$$kd = \text{binary scaling parameter}\,, \tag{5.5}$$

which means that even if we change the reaction rate (and consequently Ω) or the diameter of the cone, as long as this parameter is constant, the flow fields behind the shock, plotted in normalized coordinates, should be the same. Also implying the same normalized detachment distance. However, Figure 5.12 shows two different plateau values for the equilibrium limit for the curves "CFD d=8cm" and "CFD d=16cm". This difference can be explained by looking at the vibrational temperature. To derive the binary scaling parameter, the vibrational energy is neglected and so changes on the vibrational temperature as we change the size of the body in question are neglected. In fact, these changes are important as shown in figure 5.13. The first figure compares the density field for a cone of $d = 16\,\text{cm}$ and standard reaction rates and for a cone of $d = 8\,\text{cm}$ and double the standard rates. If binary scaling would apply these two fields would superimpose exactly on each other in the normalized coordinate system used. The x-axis was normalized by the horizontal length of the cone and the y-axis by the vertical length of the cone. One sees that the fields are similar in shape but do not superimpose on each other. The detachment distance is smaller for the case of $d = 16\,\text{cm}$. The vibrational temperature along the stagnation streamline (figure 5.13-B) for both cases shows that the vibrational temperature is higher for the larger cone and also that relaxation length needed to equilibrate the vibrational and translational temperatures is smaller for the bigger cone. This is because as the cone becomes bigger the flow approaches the equilibrium limit. The discrepancy in relaxation time and in the value of the vibrational temperature results in the difference in normalized detachment distance observed between the curves "CFD d=8cm" and "CFD d=16cm" of figure 5.12. As a final check to discard the possibility that the difference is due to the grid, equivalent normalized grids were used to do the same comparison and the results were the same.

Three more cases are presented to see the effect of the angle and the free-stream conditions in the general behavior of the detachment distance. The first case corresponds to the same condition

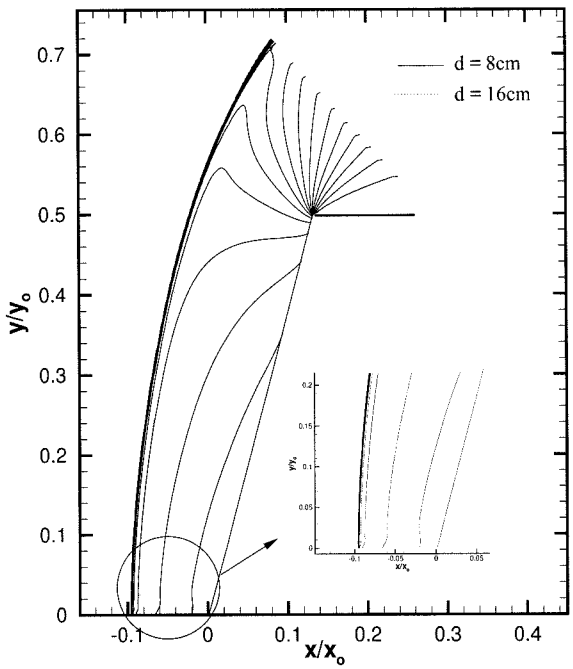

A. Density contour fields.

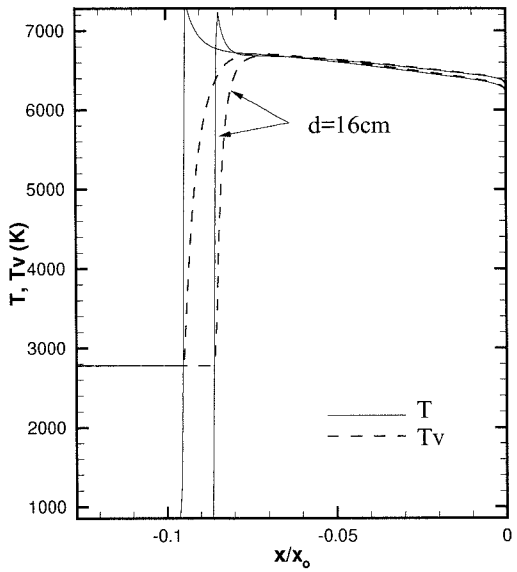

B. Vibrational and translational temperature along stagnation streamline.

Figure 5.13: Comparison of normalized detachment distance between a cone of $d = 8$ cm with double the Park 85 rates and a cone of $d = 16$ cm with the standard Park 85 rates. If binary scaling would apply to these two flows, the contour fields and temperature traces would be identical. The free stream conditions in both cases are those of N_2 2 ($P_o = 53.9$MPa, $h_o = 10.3$MJ/kg) and the angle is $\theta = 70°$.

as before but with a cone half-angle of 75° (see figure 5.14). This curved is shifted upward from the last one, as expected since we now have a bigger half-angle. The plateau value for the frozen limit is higher than for the previous case ($\Delta/d \approx .105$) but still lower than the actual frozen value of $\Delta/d = .133$. In both figures, the difference between the plateau value for "CFD d=2cm" and the actual frozen value is about 23%. Note also the same discrepancy between the curves "CFD d=8cm" and "CFD d=16cm" as for the previous figure. The percentage difference in the plateau values between the two curves is 9.5%, smaller than for the previous angle (18%). Finally, let's keep the angle constant at 75° and vary the free-stream conditions. Figure 5.15 is the corresponding picture for N_2 4. The figure is similar to the last one, except that the equilibrium values are higher since we have a smaller density in the free-stream condition. Notice that the percentage difference between the curves "CFD d=8cm" and "CFD d=16cm" is the same as for the last figure regardless of the difference in free-stream conditions. Finally, figure 5.16 is the corresponding case for N_2 3. In this case, we have three equilibrium curves to compare, "CFD d=2cm", "CFD d=8cm" and "CFD d=16cm". The percentage difference between the curves "CFD d=2cm" and "CFD d=8cm" is about the same as that between "CFD d=8cm" and "CFD d=16cm". A last feature to notice of the four figures shown last is that the rate of change in the most rapidly changing region is about the same

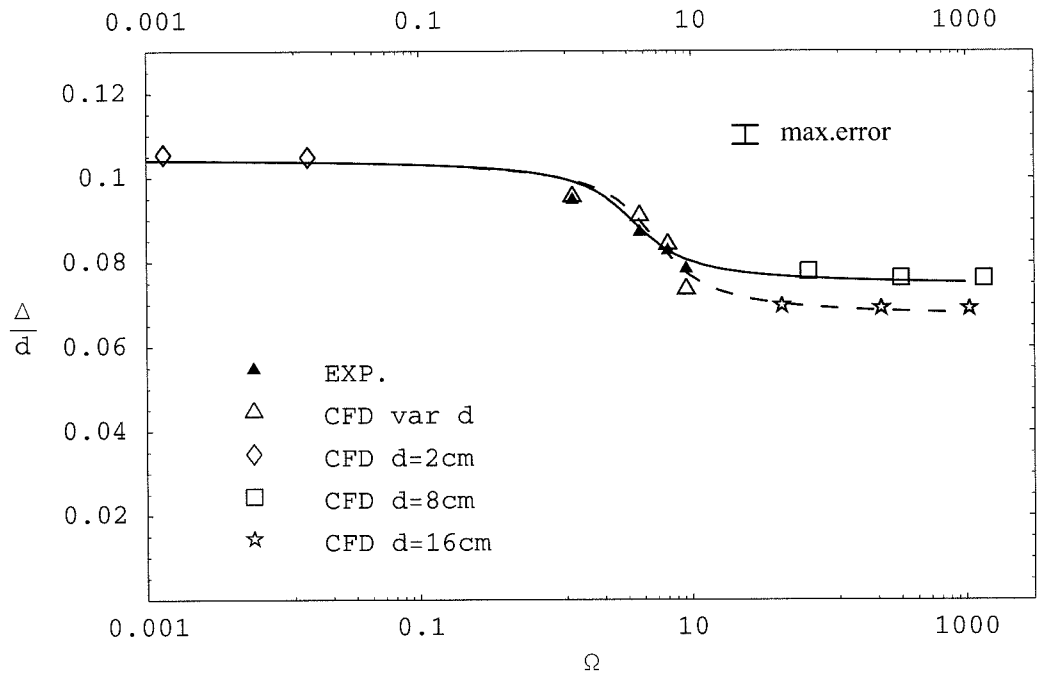

Figure 5.14: Non-dimensional detachment distance from frozen to equilibrium limits for condition N_2 2: $P_o = 53.9$MPa, $h_o = 10.3$MJ/kg, $\theta = 75°$.

for all as seen by the fact that the variable c in the fits is about the same.

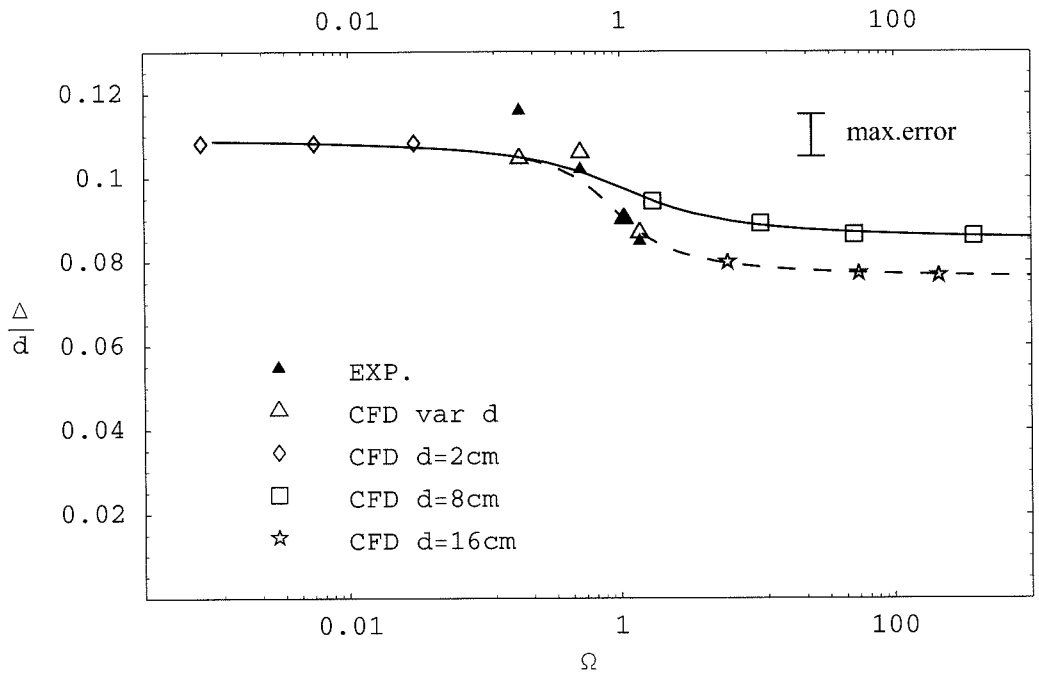

Figure 5.15: Non-dimensional detachment distance from frozen to equilibrium limits for condition N_2 4: $P_o = 28.2$MPa, $h_o = 9.20$MJ/kg, $\theta = 75°$.

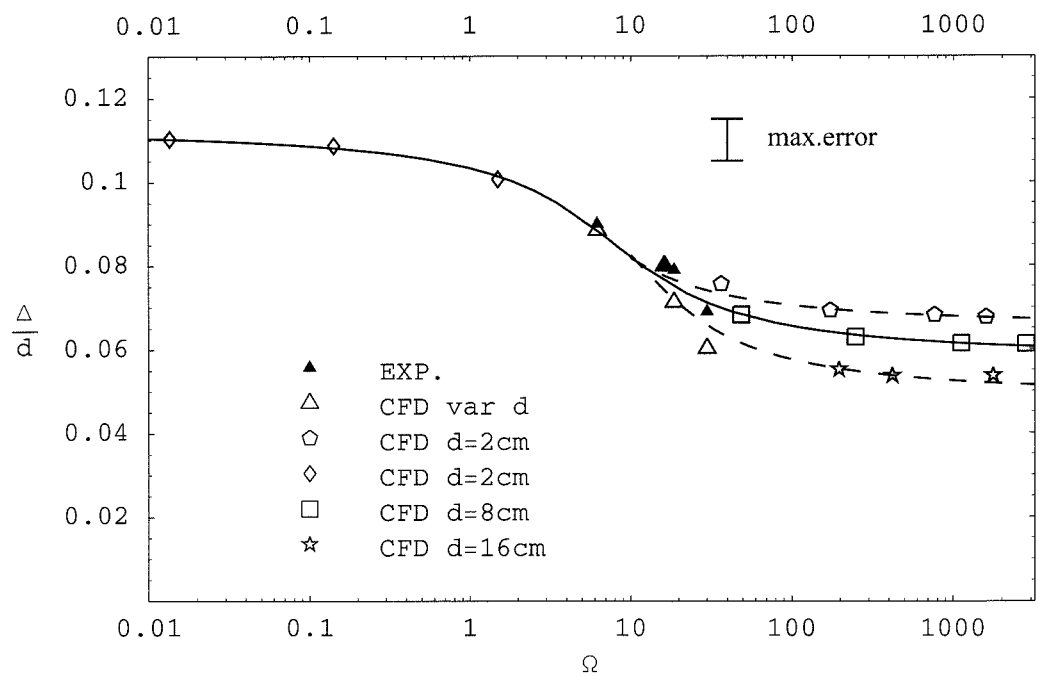

Figure 5.16: Non-dimensional detachment distance from frozen to equilibrium limits for condition N_2 3: $P_o = 20.3$MPa, $h_o = 16.3$MJ/kg, $\theta = 75°$.

Wen and Hornung (1995) correlated the modified detachment distance,

$$\Delta_m \equiv \frac{\Delta}{d}\frac{\rho_s}{\rho_\infty}, \tag{5.6}$$

for spheres in hypervelocity flows to the reaction rate parameter Ω. They found similar behavior of the detachment distance as Ω varies from the frozen to the equilibrium limits as the one seen in the last four figures. The main difference between the two studies is that they did not find any effects due to vibrational nonequilibrium when they used the modified detachment distance instead of the simple normalized detachment distance. They found similar "peel-offs" from a main curve but in their case they were due to a difference in stagnation enthalpy of the free-stream condition and not to vibrational nonequilibrium. Figure 5.17 shows the results obtained for this study when using the modified detachment distance and putting together the detachment distance curves for three different N_2 free-stream conditions. We see that the collapse of the data is better in terms of closer agreement of the curves for different diameters of the same condition in the equilibrium limit. The difference observed between the curves "CFD d=8cm" and "CFD d=16cm" for the condition N_2 4 can be explained in terms of the error in the modified detachment distance which for this condition is about 20 %. The same is true for the curves "CFD d=2cm" and "CFD d=8cm" for the condition N_2 3. What cannot be explained by the error in the modified detachment distance is the difference between the curves "CFD d=8cm", "CFD d=2cm", and the curve "CFD d=16cm" for the same condition. These difference most probably come from vibrational nonequilibrium. Finally, notice the collapse of the three curves for the different conditions in the frozen limit.

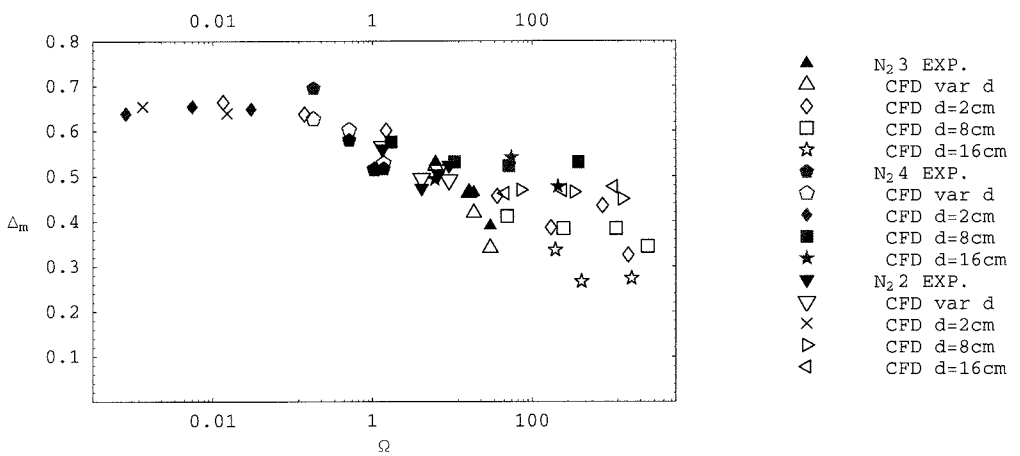

Figure 5.17: Modified non-dimensional detachment distance from frozen to equilibrium limits. The first set of points are for condition N_2 3, the next set of points correspond to condition N_2 4, and the last set is for to condition N_2 2. For all of these cases the cone half-angle is 75°.

Chapter 6 Surface measurement results: heat flux and surface pressure

The first part of this chapter covers the effects of detachment on the heat flux. A comparison is made between heat fluxes for the same free-stream condition and diameter but different cone half-angles ranging from attached to detached conditions. Several comparisons are also made of heat fluxes for different cone diameters with the same free-stream condition and cone half-angle. The effect of the corner of the cone in the traces is also explained for the attached and detached cases. Finally, the heat fluxes are compared across different free-stream conditions for the same size and half-angle. The second part of the chapter presents the results for surface pressure. Only the largest diameter cones are equipped with pressure transducers. Dimensional and non-dimensional traces are presented for different conditions, cone diameters, and half-angles. As expected, the pressure is insensitive to chemistry and almost all traces presented fluctuate around the same value (away from corner and tip) regardless of free-stream condition or half-angle.

6.1 Dimensional heat flux

As mentioned in section 3.5, the heat flux traces are obtained from the temperature-time traces for each thermocouple. Figure 6.1 is a typical set of heat flux time traces for a given shot. Each trace corresponds to a particular thermocouple whose location along the surface of the cone is stated in each subgraph. The dashed vertical lines indicate when the interferogram was taken. The last subgraph is the set of heat flux averages for each thermocouple during the test time. The averages are taken over an interval of 0.1 ms and, in general, centered at the time the interferogram was taken like in the case shown in this figure. The location of the thermocouples is normalized with the length of the cone hypotenuse. For the case presented in this figure, the shock is fully detached and we can observe that the heat flux is almost constant along the surface of the cone. It was found that, in general, the experimental heat flux average traces for detached cases are almost constant along the surface of the cone, whereas for attached cases, the heat flux shows a peak near the cone tip. We will expand on this feature later in the chapter.

Joining the above graph with similar ones (same free-stream condition and diameter) of different cone half-angles gives figure 6.2. For the first two cases corresponding to $\theta = 55°$ and $58°$, the shock is attached at this free-stream condition. Note the fast drop in the heat flux in the three thermocouples closest to the cone tip. Contrast this with the almost constant traces for $\theta = 65°$,

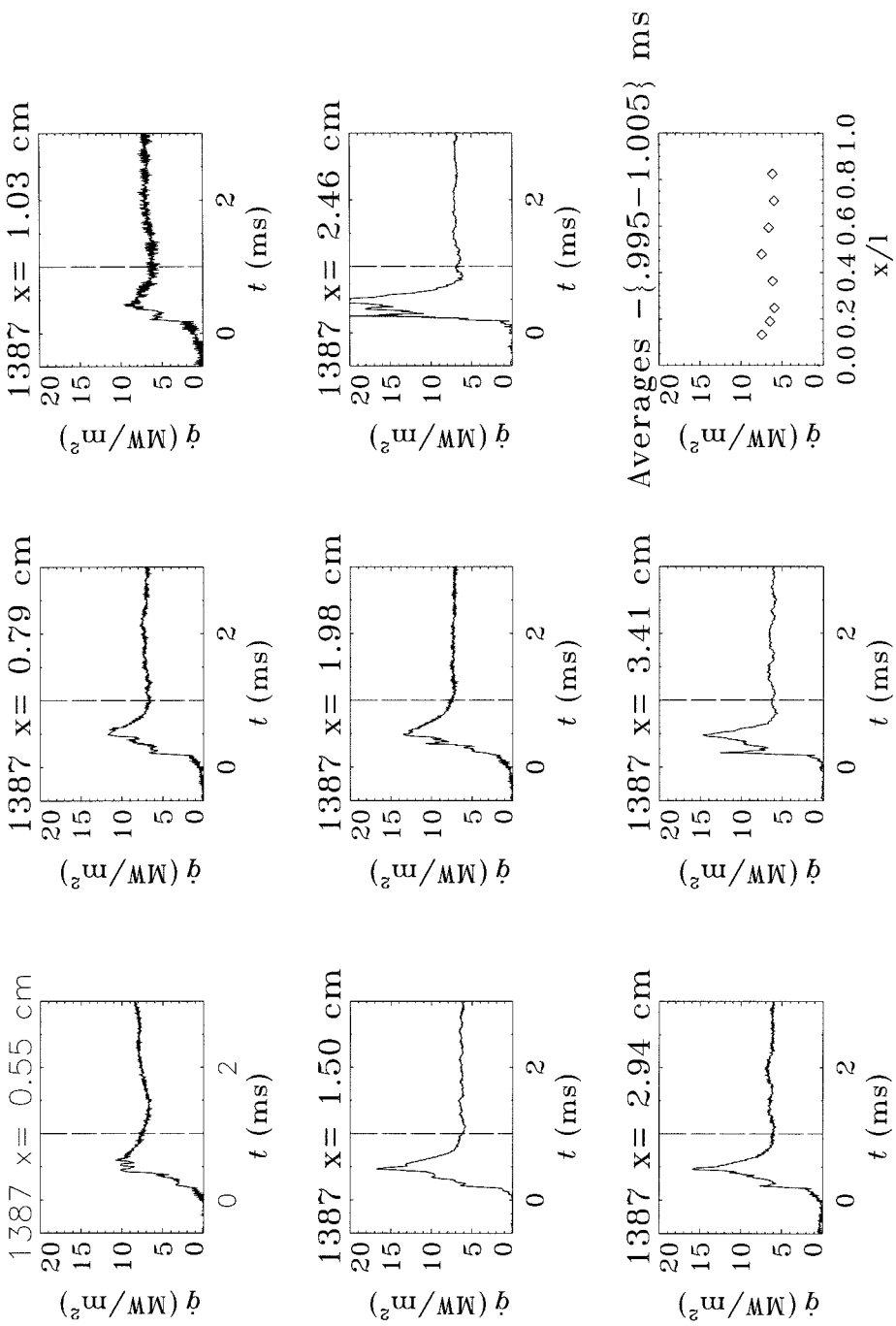

Figure 6.1: Dimensional heat flux traces for shot 1387. Condition N_2 4: P_o = 28.2MPa, h_o = 9.20MJ/kg.

70°, and $\theta = 75°$. The peak in the second thermocouple for the case $\theta = 70°$ is attributed to malfunctioning of the thermocouple and not to a physical increase in heat flux at that location. The case $\theta = 65°$ is a transition case with incipient detachment. The higher heat flux close to the tip for the attached cases can be understood by looking at the boundary layer and the flow field just outside of it. For the attached case, the edge of the boundary layer is supersonic, whereas for the fully detached case the boundary layer is subsonic throughout. Also, for the attached case, we have a constant pressure field outside the boundary layer while for the detached case, we have a favorable pressure gradient which makes the boundary layer thinner. Finally, the temperature outside the boundary layer is higher near the cone tip in the attached case since the temperature has not relaxed to its final equilibrium value before reaching the boundary layer. All of the above result in higher heat flux near the tip for the attached cases. However, the heat flux traces for all angles tested tend to the same value from about the middle of the cone until the corner.

To see that the described features are not particular to the above free-stream condition, refer to figures 6.3 and 6.4. In the first of the two figures we again see high peaks in the heat flux for the smallest two angles and approximately constant traces for the last two angles. Note also that the plateau value for the N_2 2 condition is higher than for the last condition (see figure 6.2) since the former has higher temperatures outside the boundary layer. Figure 6.4 shows that the behavior of the boundary layer and edge temperature is common to N_2 and CO_2 as one would expect since the features discussed are independent of the gas in question.

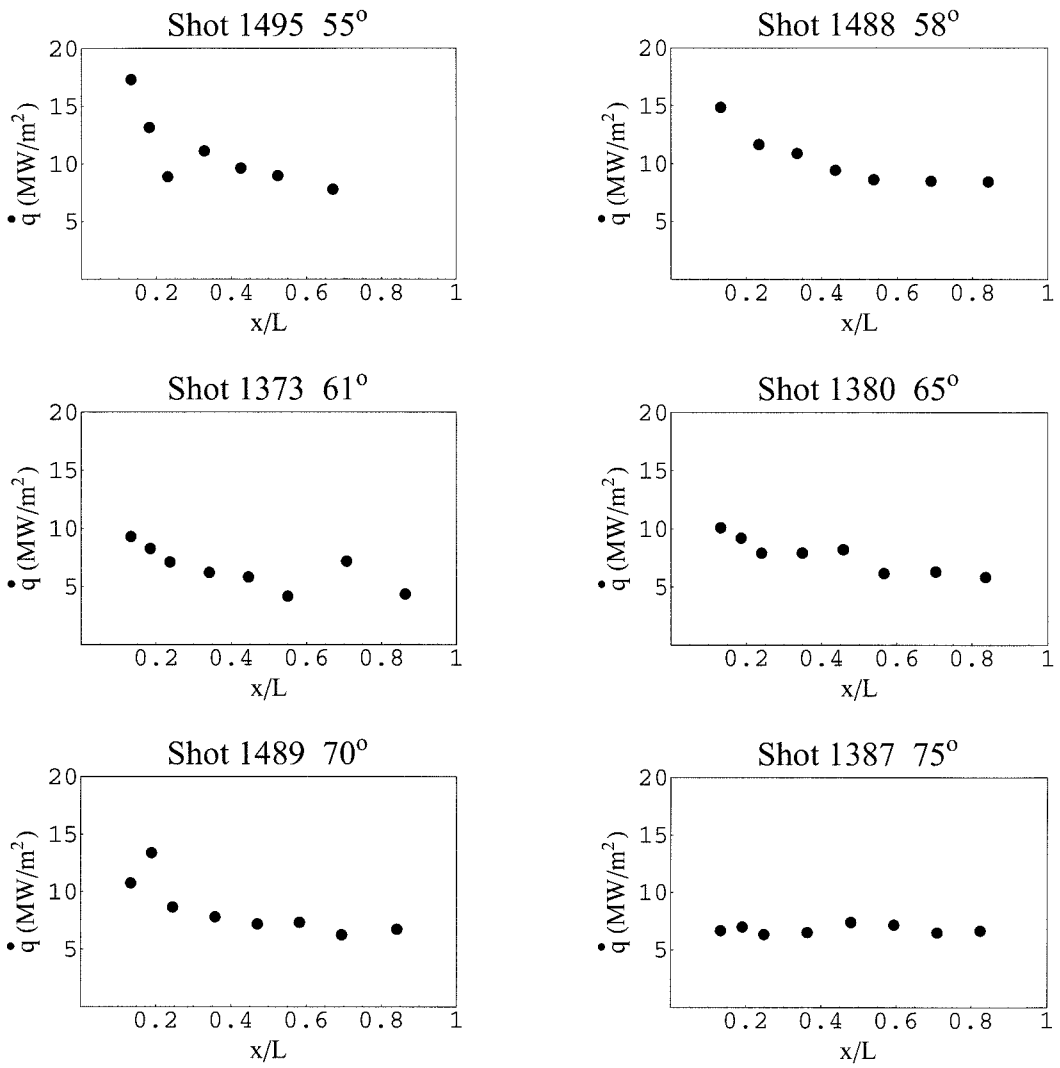

Figure 6.2: Average heat flux for $d = 8\,\mathrm{cm}$. Condition N_2 4: $P_o = 28.2\mathrm{MPa}$, $h_o = 9.20\mathrm{MJ/kg}$.

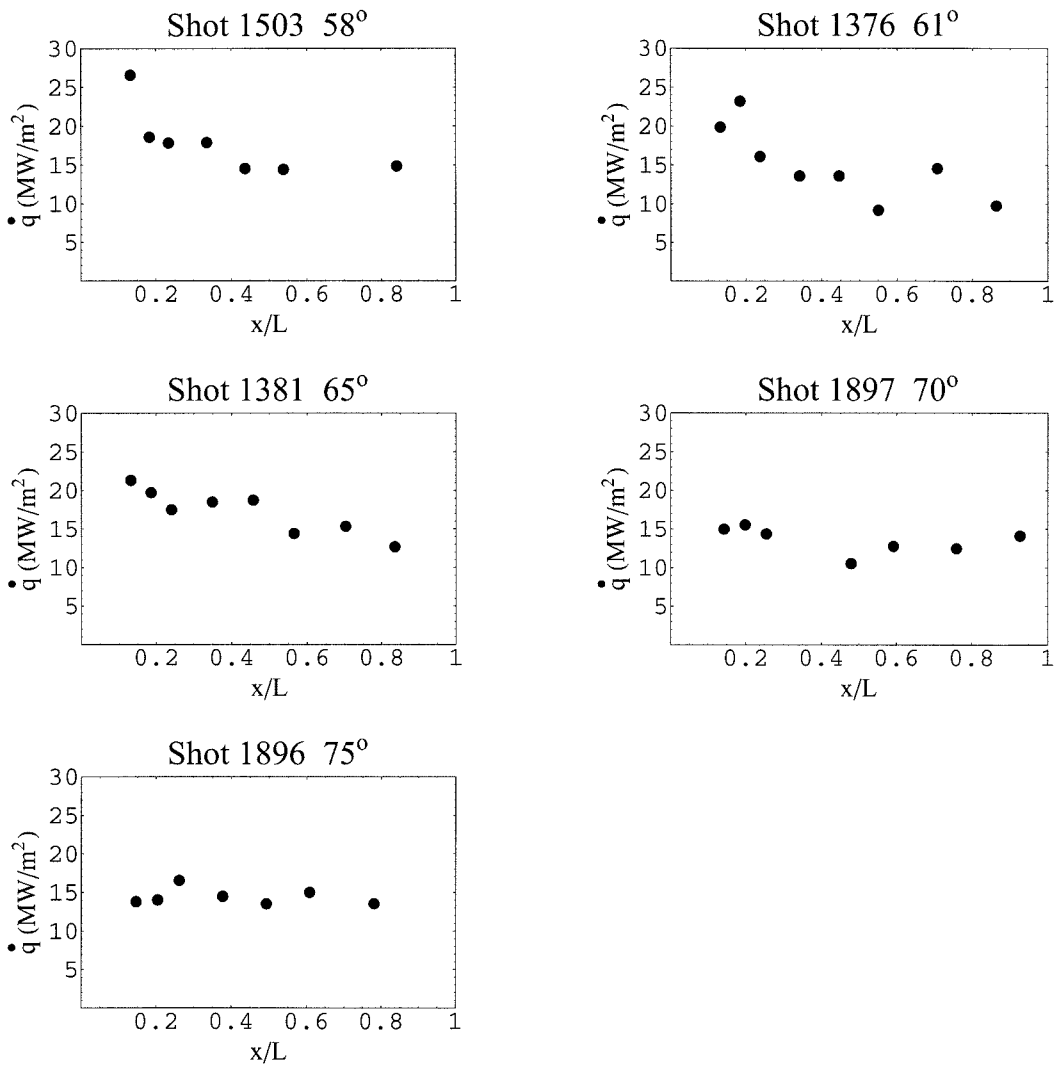

Figure 6.3: Average heat flux for $d = 8\,\mathrm{cm}$. Condition N_2 2: $P_o = 53.9\mathrm{MPa}$, $h_o = 10.3\mathrm{MJ/kg}$.

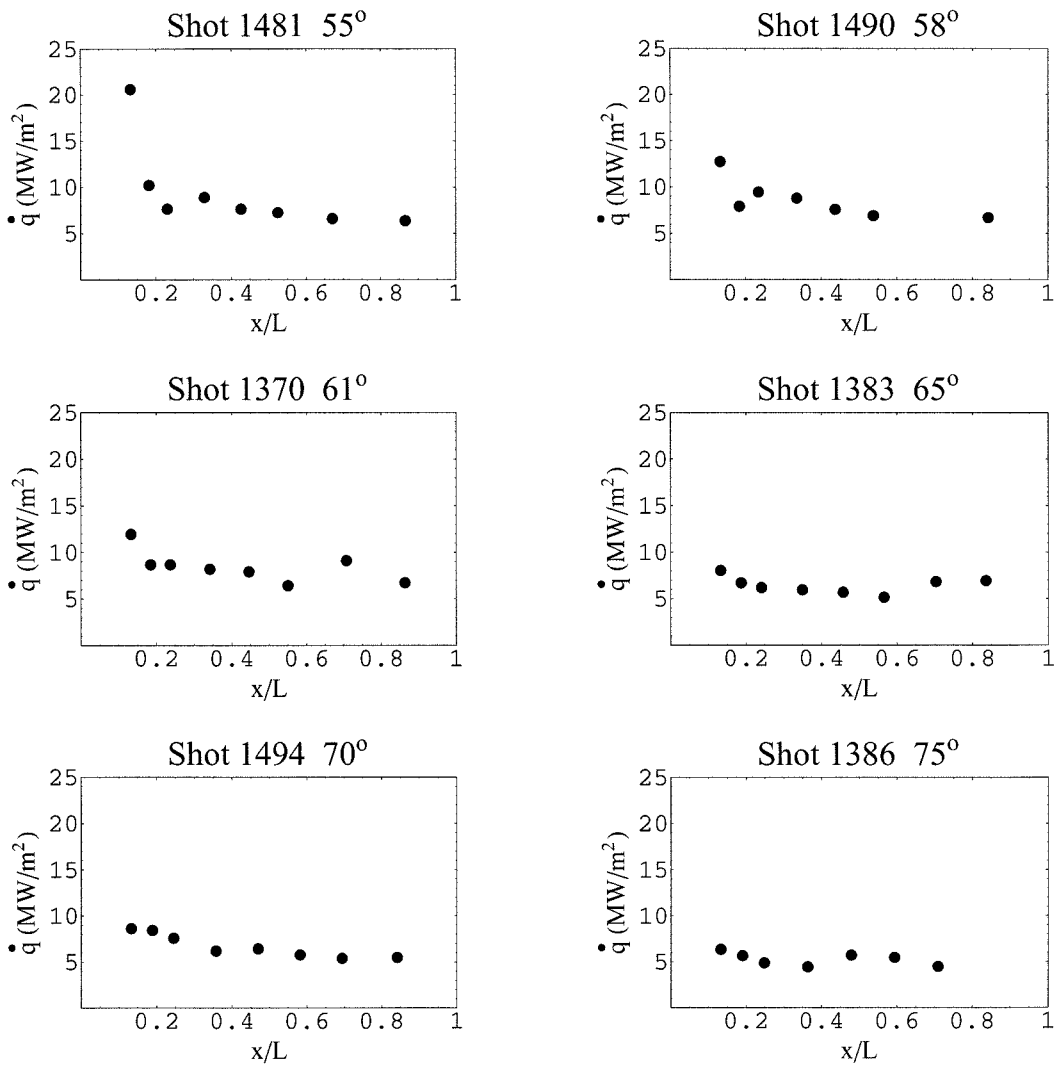

Figure 6.4: Average heat flux for $d = 8\,\mathrm{cm}$. Condition CO_2 2: $P_o = 24.5\mathrm{MPa}$, $h_o = 6.62\mathrm{MJ/kg}$.

6.2 Non-dimensional heat flux

Now non-dimensionalize the heat flux to form the Stanton number and study the behavior of St vs. Re. Figure 6.5 shows on the left the dimensional heat flux averages with the respective error bars. The error bars are computed as discussed in appendix C. They are about $10 - 15\%$ for all cases. The solid line is the result obtained from the nonequilibrium code run in its viscous mode. Since all the numerical results obtained in this chapter are from the same nonequilibrium code, they will be referred to as the CFD data. The peak close to the corner of the cone is due to the thinning of the boundary layer that happens because of the expansion around the corner. In this case, the only subsonic flow is inside the boundary layer (see figure 6.6) since the shock is attached and the flow is everywhere supersonic outside the boundary layer. The effect of the corner can only be transmitted

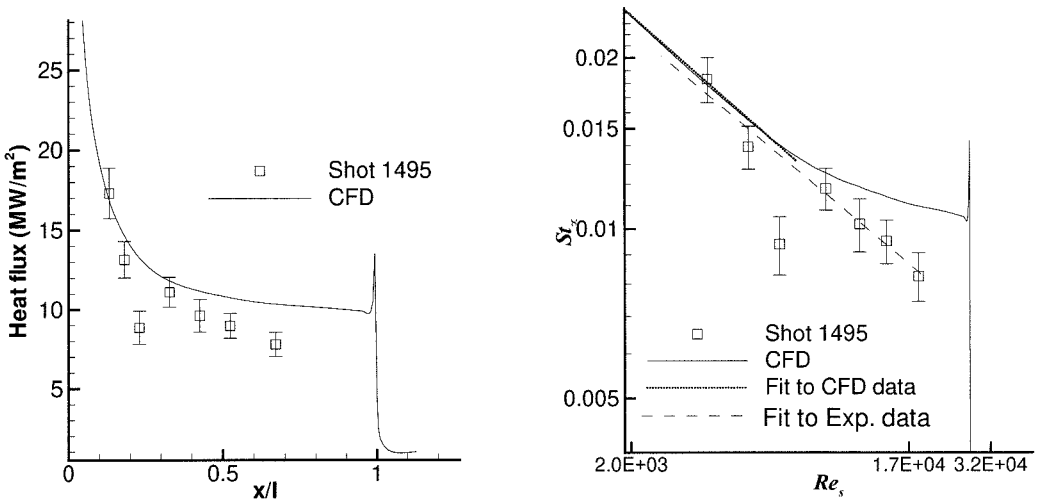

Figure 6.5: Dimensional and non-dimensional heat flux for condition N_2 4: $P_o = 28.2$MPa, $h_o = 9.20$MJ/kg, $\theta = 55°$, $d = 8$ cm. The shock is attached in this case.

upstream through the subsonic portion of the boundary layer. Therefore the effect is felt only very close to the actual corner. The right graph in figure 6.5 is the heat flux in non-dimensional form. First, note that the highest Re in this case is about $3.2e4$ and therefore the flow is laminar (see Adam (1997) for transition Re in cones in hypervelocity flows). The dotted line is a fit to the expression derived in equation 2.14 for the experimental data. Adam (1997) showed that, for attached cases in air with stagnation enthalpies varying from 5–30 MJ/kg, the value of A in equation 2.14 goes from $\approx 0.65 - 0.8$. In his case, the Mach number at the edge of the boundary layer was higher than for the present cases but it is nevertheless instructive to obtain reference values for the constant A. In the present case, $A = 0.810$ for the CFD curve (fitted in its linear range for low Re) and $A = 0.679$ for

the experimental results. Both of these values are within the range given by Adam (1997) despite the difference in the values of the edge Mach number. The fitted line should have a slope of $-1/2$ according to equation 2.14. The calculated values for the slope are -0.47 and -0.45 for the CFD and experimental cases respectively, which are also in good agreement with the theoretical value. Note that the experimental data are linear in the log-log scale up to the last thermocouple closest to the corner.

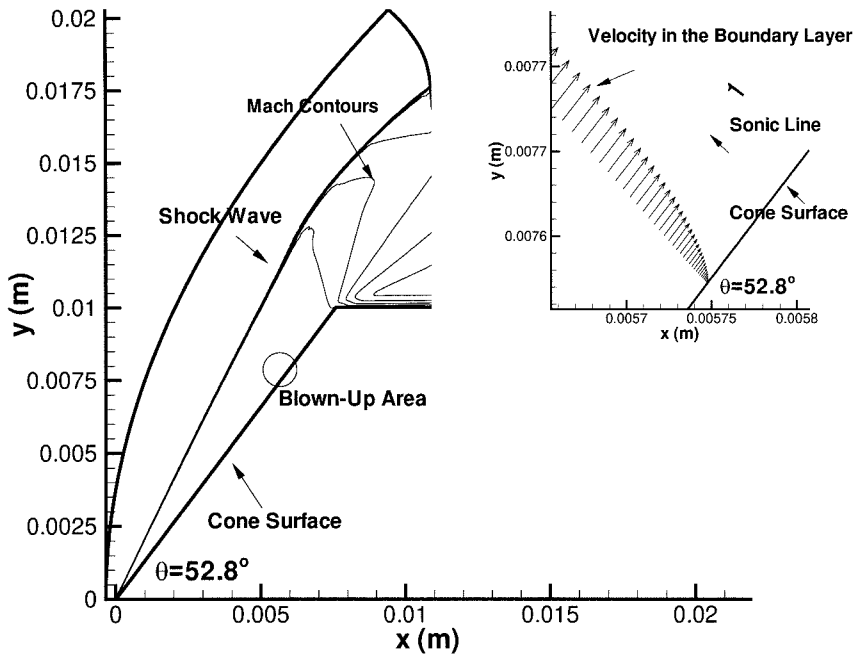

Figure 6.6: Sonic line for condition N_2 4: $P_o = 28.2$MPa, $h_o = 9.20$MJ/kg.

Figure 6.7 shows the heat flux in dimensional and non-dimensional form for a detached case for the same free-stream condition. First note that the agreement between the experiments and the CFD results is better. For the heat flux results in this study, the agreement between CFD and experiments has to be looked at on a case to case basis (see appendix C for a detailed explanation of the error in the heat flux measurements). Sometimes, the CFD curves fall within the error bars of the experimental points and sometimes there is an offset, either positive or negative, with respect to the experimental points. The agreement depends greatly on the quality of the thermocouple traces, any local disturbances in the flow affecting a particular thermocouple reading, and how close is the particular shot to the average flow conditions used for a given free-stream condition. The case in question is an example of low-noise and fast response thermocouple traces. Comparing this case with the previous, in the dimensional graph, one notices that the heat flux drop close to the tip is fastest in the detached case. This means, that if we place thermocouples in the same non-dimensional locations for both cases, we would see some of the fast decaying part of the attached cases, but we would only see an almost constant trace for the detached cases. This is exactly what we saw in figures 6.2 – 6.4.

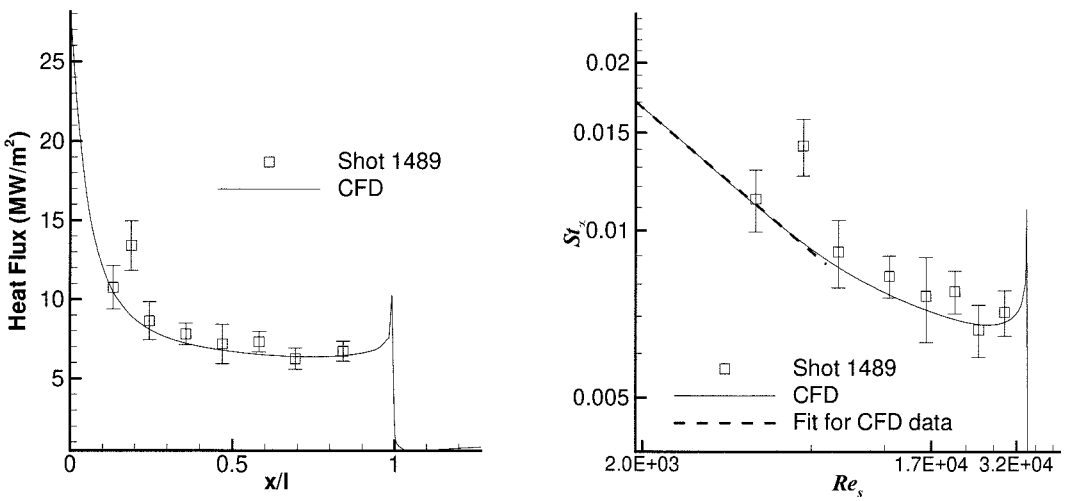

Figure 6.7: Dimensional and non-dimensional heat flux for condition N_2 4: $P_o = 28.2$MPa, $h_o = 9.20$MJ/kg, $\theta = 70°$, $d = 8$ cm. The shock is fully detached in this case.

Turning now to the $St - Re$ graph, we note that although the shock is detached and we no longer have a constant pressure field outside the boundary layer, equation 2.14 still holds very well with $A = 0.622$ and a slope of -0.48 when fitting the linear part of CFD curve. The agreement is best close to the tip of the cone. In this case, the effect of the corner expansion can be transmitted back more effectively because the flow is completely subsonic in the shock layer prior to the corner

expansion. This is why St starts increasing earlier than for the previous cases as the corner is approached.

Although there are no experimental data for heat flux for cones with $d <$ 8cm it is instructive to run a case with a smaller cone diameter and see how the heat flux varies as we vary the diameter of the cone, keeping the angle and free-stream conditions the same. Figure 6.8 shows the heat flux for three different cone diameters. The middle curve was already presented in more detail in figure 6.7. If the heat flux were sensitive to the chemistry, we should see the effects in this graph where the cone diameter changes by a factor of four. What we see, instead, are very similar curves in terms of the slope in the linear part close to the tip and their general shape. The constant A varies from 0.622 to 0.810 from the smaller to the larger cone diameter. This constant represents the intercept with the St-axis of the curve and for this case, there is no direct relation between the value of A and the diameter of the cone. The middle curve has the highest A while the curve corresponding to $d = 16\,\mathrm{cm}$ has the middle value. The corner of the cone manifests itself in two ways, the most evident one is the heat flux peak already discussed before. The more subtle one is the "peel-off" of each curve from their linear behavior. As the size of the cone increases, the range of Re covered by the cone is larger and the heat flux follows the linear part of the curve longer before feeling the effects of the corner. This means that the heat flux measured close to the end of the cone (before the corner peak) gets lower and lower as the cone diameter increases.

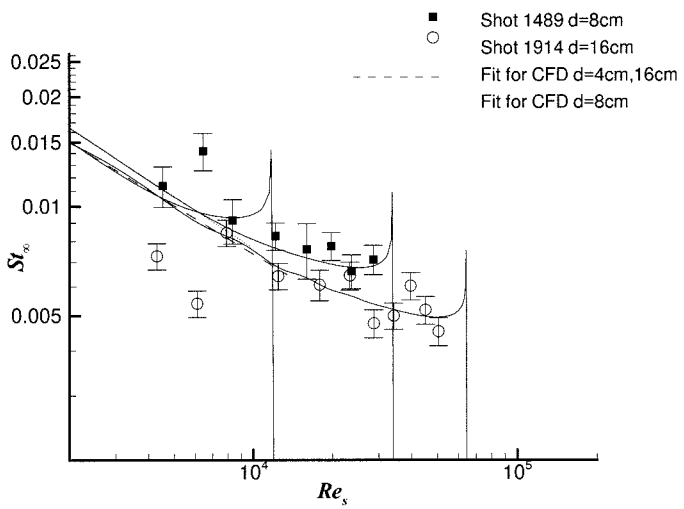

Figure 6.8: Comparison of non-dimensional heat flux for condition N_2 4: P_o = 28.2MPa, h_o = 9.20MJ/kg, $\theta = 70°$.

The last figure in this section, 6.9, is a similar comparison but for condition N_2 2. The results are also equivalent. Although the heat flux is consistently higher in the linear part for the curve

corresponding to $d = 4\,\text{cm}$ than for $d = 8\,\text{cm}$, no direct relation can be found between A and d since the curve for $d = 16\,\text{cm}$ crosses the other two curves. Note that for this case, we have experimental heat flux traces closer to the corner and they indicate the rise predicted by CFD.

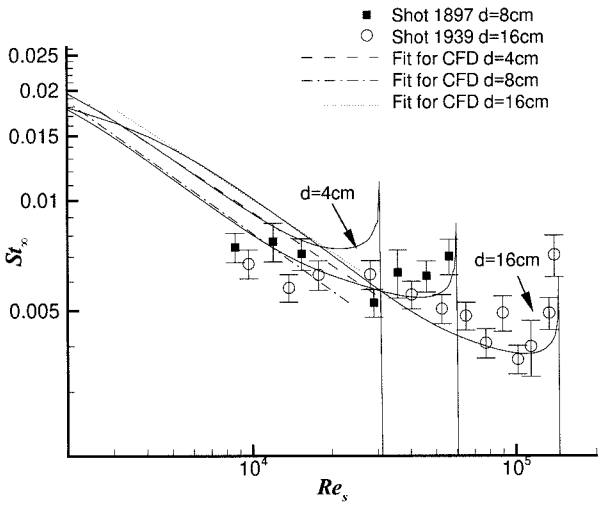

Figure 6.9: Comparison of non-dimensional heat flux. Condition N_2 2: $P_o = 53.9\text{MPa}$, $h_o = 10.3\text{MJ/kg}$, $\theta = 70°$.

6.3 Pressure measurements

The last part of this chapter deals with the surface pressure measurements for the largest cones. The first figure in this section (6.10) is a sample of the pressure-time traces for a given shot. The vertical line indicates when the interferogram and pressure averages were taken. In this case, the first two traces would not be considered when making an average plot. They have a slow rise due most probably to a loose connection of the transducer into its fitting. Refer to appendix A for a drawing of the pressure transducer mountings.

The pressure traces are non-dimensionalized into a pressure coefficient C_p as follows,

$$C_p = \frac{p}{1/2\rho_\infty u_\infty^2}, \tag{6.1}$$

and C_p is plotted against the distance along the hypotenuse (x) of the cone normalized by the length of the hypotenuse (L). Figure 6.11 shows four different CFD traces for different cone diameters with the same angle of 70°. The CFD calculations are inviscid and use grids of 200 × 200 points on average. The experimental data for $d = 16\,\text{cm}$ are also presented with the corresponding error bars.

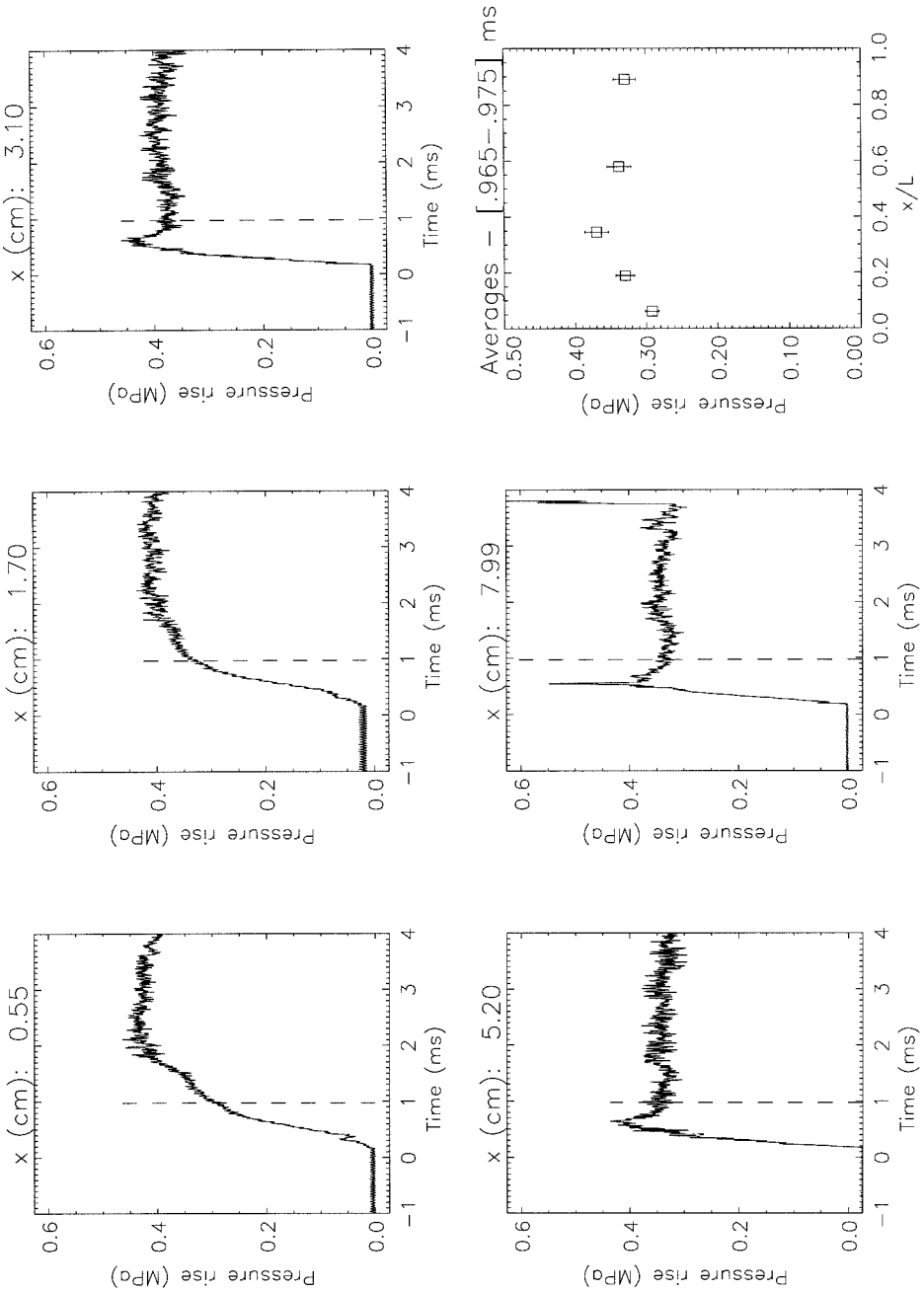

Figure 6.10: Dimensional pressure traces for condition N_2 4: $P_o = 28.2$MPa, $h_o = 9.20$MJ/kg, $\theta = 70°$, $d = 16$ cm.

The striking feature is that all the traces fall on top of each other. There is no discernible effect of the chemistry on the surface pressure field. We know from previous discussions about the detachment distance (see figure 5.7) that the flow around the smallest cone ($d = 2$ cm) is almost frozen and

for the biggest it is almost in chemical and thermal equilibrium. The surface pressure, however, is practically the same for both extremes. This confirms that the pressure is mostly a mechanical variable which depends more on the mechanical aspects of the flow than on its thermodynamics or chemistry (see Hornung (1996) and Anderson (1989)). Another feature to observe in all traces is that the pressure decreases throughout the length of the cone. This is to be expected since the flow is accelerating in its trajectory from the tip to the corner. There is a favorable pressure gradient for all the cases with detached shocks studied here. One of the reasons why we found such good agreement between the experimental heat flux and 2.14 in the last section, even though the shock was detached and the pressure gradient outside the boundary layer was not constant, is precisely that the pressure remains about constant prior to responding to the corner flow acceleration.

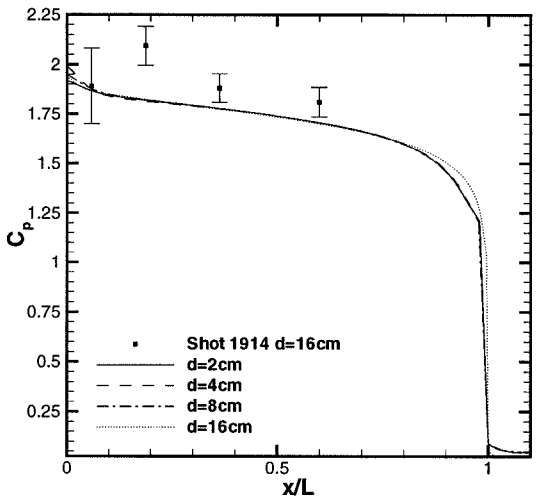

Figure 6.11: Pressure coefficient for four different cone diameters. Condition N_2 2: P_o = 53.9MPa, h_o = 10.3MJ/kg, $\theta = 70°$.

Figure 6.12 shows the surface pressure traces for three different free-stream conditions but with the same cone diameter and half-angle. The experimental and CFD results are presented for each case. The CFD traces only differ slightly toward the corner expansion. It is difficult to point out any trend for the experimental results as they seem to fluctuate around a constant value. This graph is another way of checking that the surface pressure is insensitive to chemistry since both P_o and h_o determine the reaction rates and the vibrational temperature and they vary widely for each condition.

The previous conclusions are also valid for CO_2 2 and figure 6.13 shows proof of this. For CO_2 2 there are no CFD calculations but one can see from the graph that the difference between the two traces is only about 10% and the P_o changes by a factor of more than two between the two conditions.

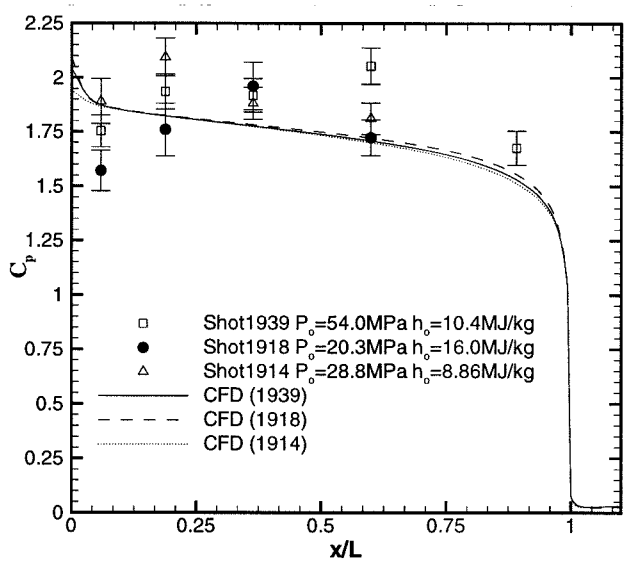

Figure 6.12: Pressure coefficient for different conditions in N_2 flows ($\theta = 70°$, $d = 16\,\text{cm}$).

Therefore, the pressure is insensitive to the chemistry.

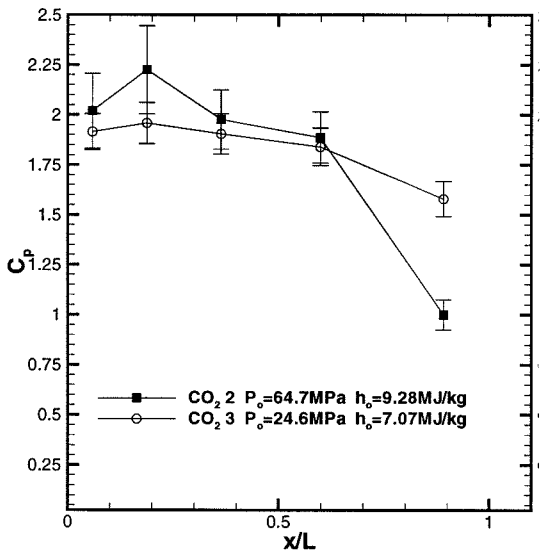

Figure 6.13: Pressure coefficient for different conditions in CO_2 flows ($\theta = 70°$, $d = 16\,\text{cm}$).

The last comparison that will be made is between different cone half-angles keeping the cone diameter and free-stream condition the same. Figure 6.14 shows four different traces for cone half-angles ranging from $\theta = 56°$ and $\theta = 75°$. In this case, there is a increase in pressure as the angle increases. This is because for the same free-stream condition, the shock gets stronger as the angle

increases and this results in higher pressures after the shock. The same comparison was made for the condition CO_2 2 for $\theta = 70°$ and $\theta = 75°$ and the conclusions were the same.

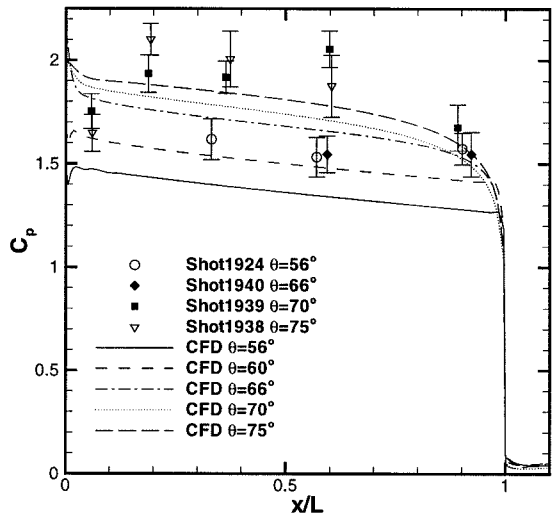

Figure 6.14: Surface pressure distributions for different cone half-angles. N_2 2: $P_o = 53.9$MPa, $h_o = 10.3$MJ/kg.

Chapter 7 Conclusions

A comprehensive experimental and computational study has been made on the shock detachment process on cones in hypervelocity flows. The experimental program consisted of about 170 shots performed at Caltech's hypervelocity shock tunnel, T5. A total of 24 cones were tested, each in six different free-stream conditions. Four of these conditions used N_2 as the test gas and two used CO_2. These conditions were designed to span the maximum ranges of P_o and h_o available for a given nozzle and piston mass. The cones ranged in diameter from 2cm to 16cm and varied in half-angles from 55° to 75°. The detachment distance was measured off holographic interferograms taken of every shot. Heat flux and surface pressure measurements were also made on the larger cones to determine how sensitive these parameters are to nonequilibrium effects. The numerical study used the code provided by Joe Olejniczak from NASA Ames (Olejniczak, 1997). After being validated with frozen attached cases and with available experimental data, the code was extensively used to expand the domain of sizes and conditions covered by the experimental data. This code is a Navier-Stokes solver that can account for thermal and chemical nonequilibrium in axisymmetric flows. The agreement found between the computational and experimental measurements of the detachment distance fell within the experimental error.

One of the main findings from the experimental and computed detachment distances is that, for a given free-stream condition, the normalized shock detachment distance grows more slowly for nonequilibrium flows than for frozen and equilibrium flows as a function of the cone half-angle. The same trend is found in CO_2 and N_2 flows. This confirms the previous theoretical model of Hornung and Houwing (1980). The explanation lies in the behavior of the sonic line in the shock layer. The detachment distance grows faster when it is scaled by the diameter of the cone as is the case for the frozen and equilibrium flows, than when it depends on the relaxation length as is the case in nonequilibrium flows. This is a consequence of the different behavior of the speed of sound and flow speed inside the relaxation zone. The computations were very useful for finding the limiting behaviors of the detachment distance in frozen and equilibrium conditions where no experimental data were available. In both limits the growth of the detachment distance is found to be linear with the cone half-angle. This linear growth agrees with experimental data for the frozen limit (see Ward and Pugh (1968)) and for the first time shows evidence for the theoretical predictions in the equilibrium limit.

The behavior of the detachment distance has also been analyzed for a given angle from the frozen to the equilibrium limits in N_2 flows. The computational results show strong support for

the theoretical predictions by Hornung and Houwing (1980) that the ratio of the shock detachment distance to the diameter is constant (for a given angle and free-stream condition) for the two limits. The detachment distance is seen to change most dramatically for the range of cone diameters used in this study. This dramatic change means that we have captured experimentally the most sensitive regime for the effects of nonequilibrium on the detachment distance.

A comparison has also been made between experimental and computational interferograms. The interferograms are compared in terms of the detachment distance, the number of fringes in the shock layer, and the shape of the fringes. We were able to reproduce the asymmetry observed in the experimental interferograms by taking into account the mechanical displacements of the interferometer that can occur in the time interval between taking the two pictures needed for the holograms. With this correction the agreement was found to be good between the computational and experimental interferograms.

The heat flux measurements showed that they are more sensitive to the conditions at the edge of the boundary layer, the pressure field outside the boundary layer, and to the Reynolds number than to the nonequilibrium effects in the flow. One could not relate changes seen in the different traces to nonequilibrium effects directly. These conclusions apply to all the free-stream conditions studied. The heat flux measurements agree within the experimental error with the computational results. The pressure measurements confirmed the theoretical prediction that surface pressure is not sensitive to nonequilibrium effects. The computational results supported this statement as well.

Appendix A Test model drawings

A.1 Model layout for $d = 2\,\mathrm{cm}$ and $d = 4\,\mathrm{cm}$

A.2 Model layout for $d = 8\,\mathrm{cm}$

A.3 Model layout for $d = 16\,\mathrm{cm}$

A.4 Drawings for thermocouples and pressure transducer mountings

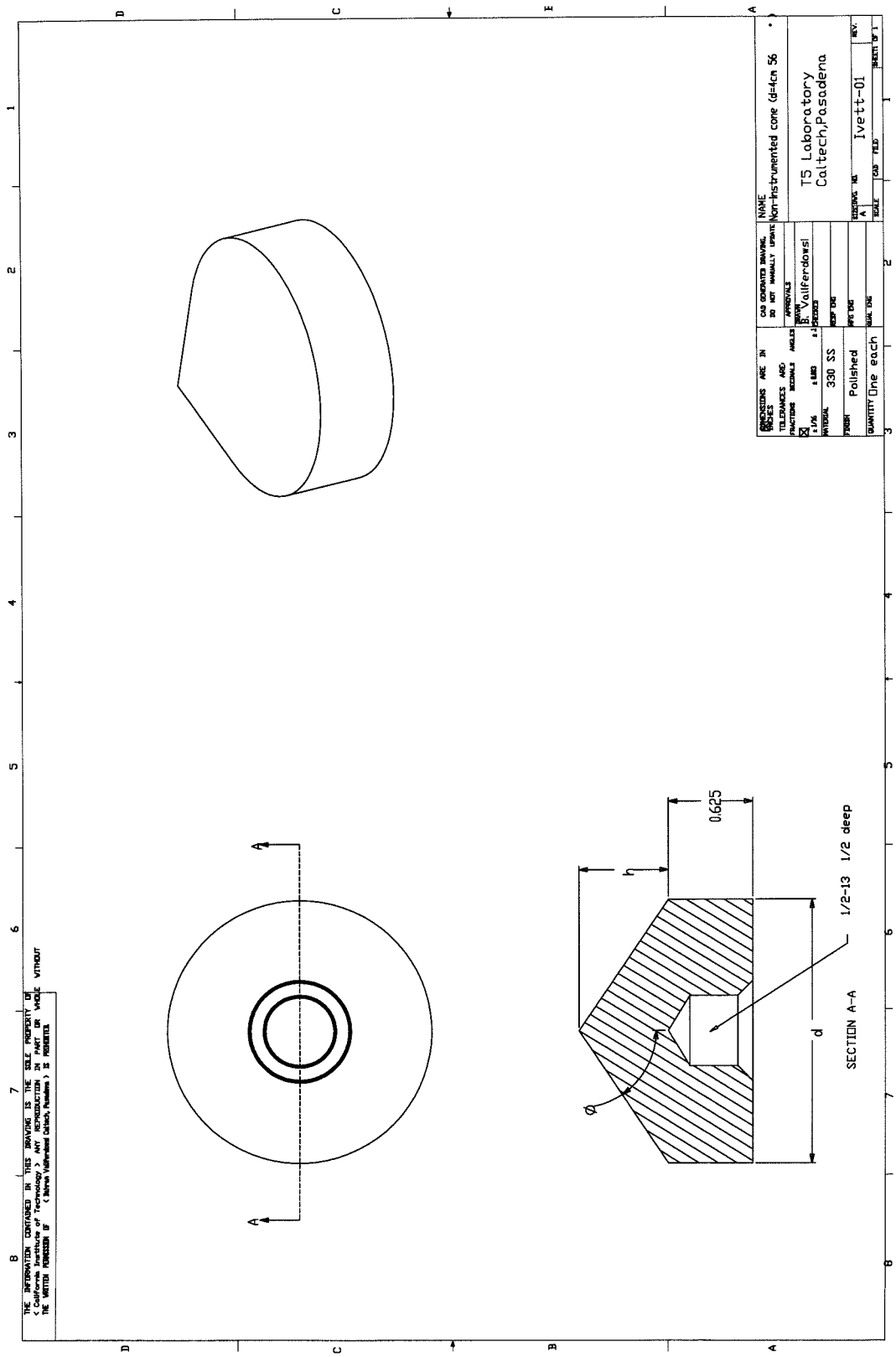

Figure A.1: Drawings for cones with $d = 2\,\mathrm{cm}$ and $d = 4\,\mathrm{cm}$.

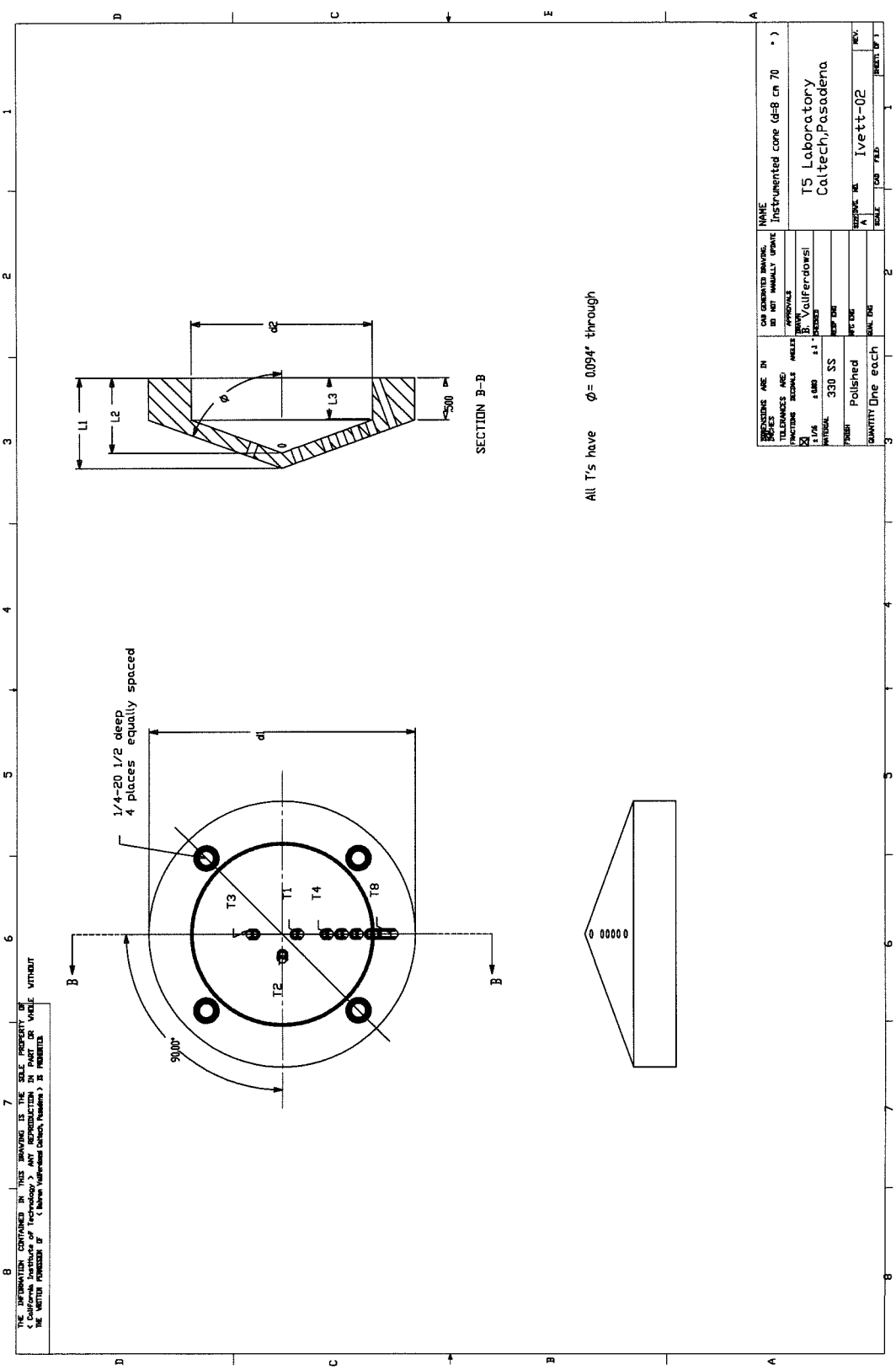

Figure A.2: Drawings for cones with $d = 8\,\mathrm{cm}$.

angle (deg)	56.0	60.0	63.0	66.0	70.0	75.0
$d = 2\,\mathrm{cm}$						
L	1.206	1.155	1.122	1.095	1.064	1.035
$d = 4\,\mathrm{cm}$						
L	2.412	2.309	2.244	2.189	2.128	2.071

Table A.1: Dimensions for the cones with $d = 2\,\mathrm{cm}$ and $d = 4\,\mathrm{cm}$. All dimensions are in cm.

angle (deg)	55.0	58.0	61.0	65.0	70.0	75.0
d1	8.000	8.000	8.000	8.000	8.000	8.000
d2	5.462	5.462	5.462	5.462	5.462	5.462
L1	4.070	3.769	3.487	3.135	2.726	2.342
L2	3.582	3.298	3.030	2.694	2.300	2.002
L3	1.670	1.592	1.517	1.421	1.307	1.270
Thermocouples						
T1	0.647	0.626	0.607	0.585	0.566	0.549
T2	0.886	0.864	0.845	0.824	0.805	0.788
T3	1.124	1.103	1.084	1.062	1.043	1.027
T4	1.602	1.581	1.562	1.540	1.521	1.504
T5	2.079	2.058	2.039	2.018	1.998	1.982
T6	2.557	2.536	2.517	2.495	2.476	2.459
T7	3.273	3.252	3.233	3.104	2.954	2.937
T8	4.228	3.968	3.949	3.689	3.581	3.414

Table A.2: Dimensions and location of thermocouples for the cones with $d = 8\,\mathrm{cm}$. All dimensions are in cm. The distances given for the thermocouples are from the tip of the cone.

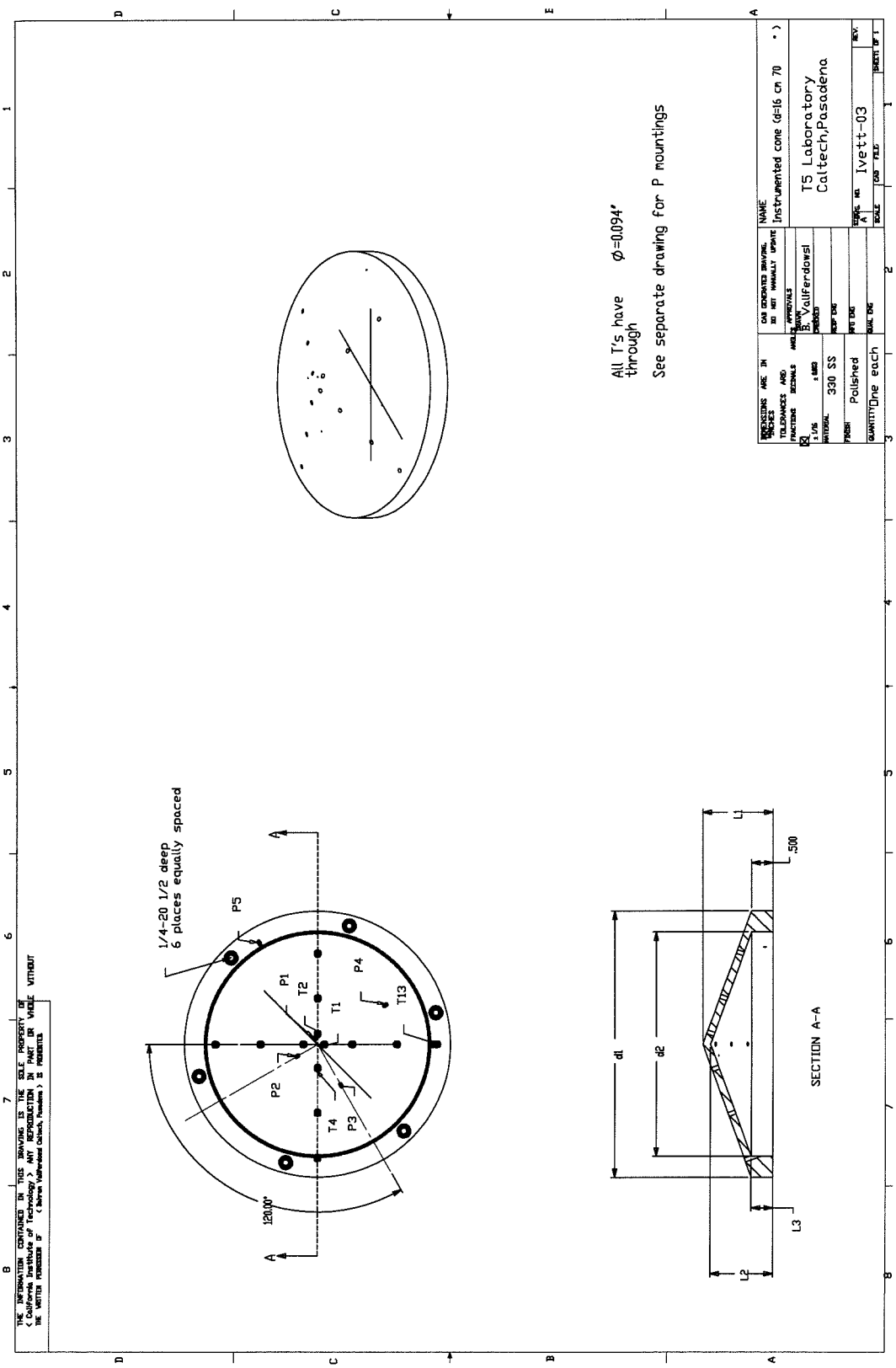

Figure A.3: Drawings for cones with $d = 16\,\mathrm{cm}$.

angle (deg)	56.0	60.0	63.0	66.0	70.0	75.0
d1	16.000	16.000	16.000	16.000	16.000	16.000
d2	13.462	13.462	13.462	13.462	13.462	13.462
L1	6.668	5.890	5.347	4.831	4.181	3.414
L2	6.185	5.428	4.897	4.394	3.757	2.300
L3	1.643	1.542	1.468	1.397	1.306	1.270
Thermocouples						
T1	0.640	0.614	0.595	0.580	0.566	0.549
T2	0.879	0.852	0.833	0.819	0.805	0.788
T3	1.165	1.091	1.072	1.058	1.043	1.027
T4	1.762	1.807	1.671	1.655	1.640	1.624
T5	2.478	2.285	2.388	2.371	2.357	2.340
T6	3.195	3.001	3.104	3.087	3.073	3.056
T7	3.911	3.717	3.820	3.803	3.789	3.772
T8	4.627	4.434	4.536	4.520	4.505	4.489
T9	5.343	5.150	5.253	5.236	5.222	5.205
T10	6.060	5.866	5.969	5.952	5.938	5.921
T11	6.776	6.583	6.685	6.669	6.654	6.638
T12	7.493	7.295	7.163	7.384	7.371	7.402
T13	8.209	8.011	7.640	8.075	7.800	7.757
T14	8.926	8.595	8.346	8.433	8.158	
T15	9.373	8.964	8.705			
Pressure transducers						
P1	0.700	0.580	0.550	0.550	0.500	0.500
P2	1.800	1.800	1.700	1.700	1.600	1.600
P3	3.200	3.000	3.100	3.100	3.100	3.100
P4	5.500	5.200	5.200	5.200	5.100	5.000
P5	8.700	8.500	7.993	8.075	7.585	7.250

Table A.3: Dimensions and location of thermocouples and pressure transducers for the cones with $d = 16\,\text{cm}$. All dimensions are in cm. The distances given for the thermocouples and pressure transducers are from the tip of the cone.

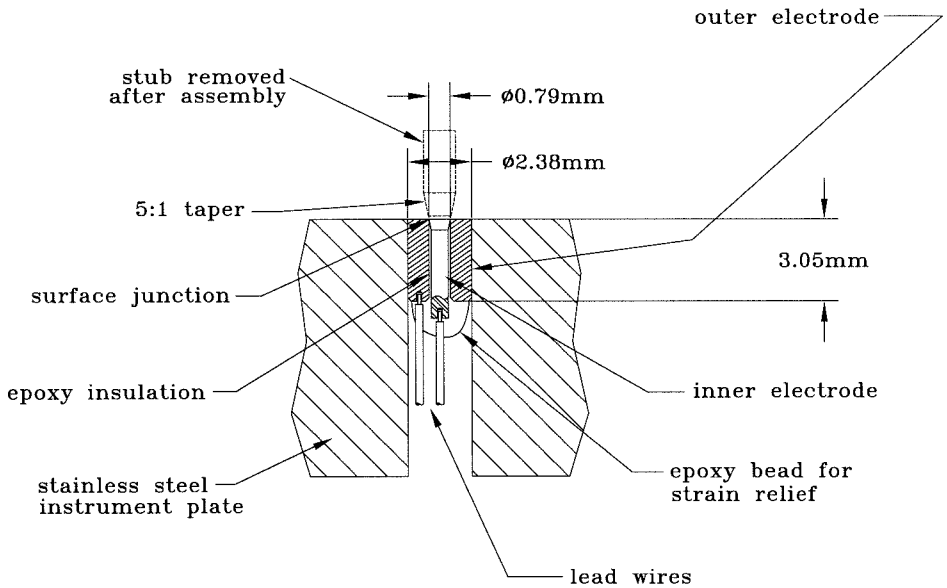

Figure A.4: Sketch of thermocouples and their mountings from Davis (1998).

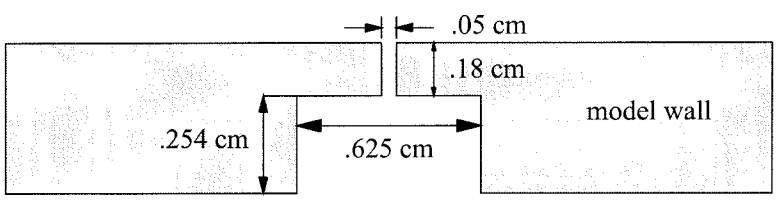

Figure A.5: Sketch of mounting setup for pressure transducers.

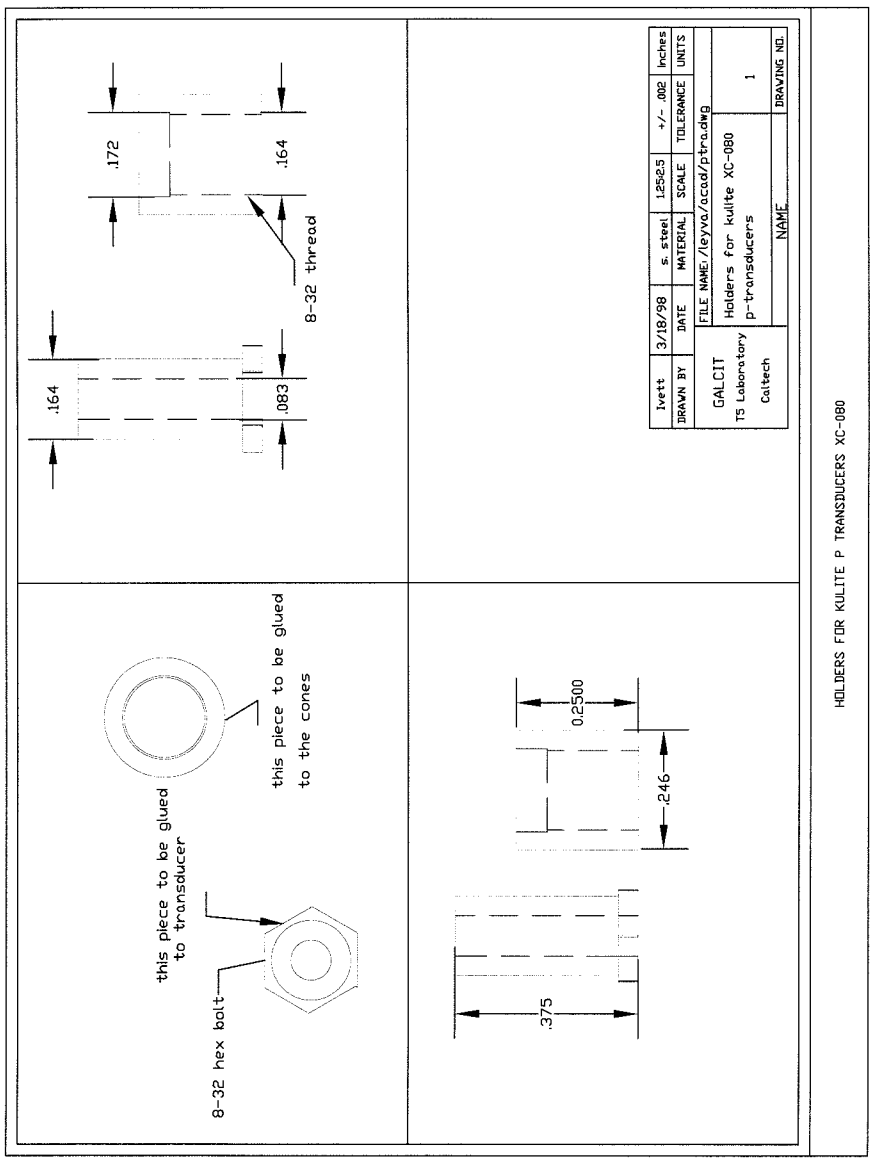

Figure A.6: Sketch of mounting pieces for pressure transducers.

Appendix B Constants used in computations

Collision partner	C_{f_m} (m^3/kmol s)	η_m	θ_m (K)
$N_2 + M \rightarrow 2N + M$			
N_2	$3.7x10^{18}$	-1.6	113200
N	$1.1x10^{19}$	-1.6	113200

Table B.1: Coefficients used for the reactions in N_2 flows. The reaction rates are taken to have the form $k_{f_m} = C_{f_m} T^{\eta m} e^{-\theta_m / T}$. Data taken from Park (1985).

Collision partner	C_{f_m} (m^3/kmol s)	η_m	θ_m (K)
$CO_2 + M \rightarrow CO + O + M$			
CO_2	$3.7x10^{11}$	0	52500
CO	$3.7x10^{11}$	0	52500
O_2	$3.7x10^{11}$	0	52500
C	$3.7x10^{11}$	O	52500
O	$3.7x10^{11}$	O	52500
$CO + M \rightarrow C + O + M$			
CO_2	$2.30x10^{16}$	-1.0	129000
CO	$4.48x10^{16}$	-1.0	129000
O_2	$2.30x10^{16}$	-1.0	129000
C	$3.40x10^{17}$	-1.0	129000
O	$3.40x10^{17}$	-1.0	129000
$O_2 + M \rightarrow 2O + M$			
CO_2	$2.0x10^{18}$	-1.5	59750
CO	$2.0x10^{18}$	-1.5	59750
O_2	$2.0x10^{18}$	-1.5	59750
C	$1.0x10^{19}$	-1.5	59750
O	$1.0x10^{19}$	-1.5	59750
$CO + O \rightarrow O_2 + C$			
	$3.9x10^{10}$	-.18	69200
$CO_2 + O \rightarrow O_2 + CO$			
	$1.7x10^{10}$	0.0	26500

Table B.2: Coefficients used for the reactions in CO_2 flows. The reaction rates are taken to have the form $k_{f_m} = C_{f_m} T^{\eta m} e^{-\theta_m / T}$. Data taken from Park *et al.* (1994).

$\theta_{v,r}$ K	g_r
1903	1
945	2
3329	1

Table B.3: Characteristic vibration temperature and degeneracy modes for CO_2 flows.

Species	κ_s (m^3/kg)
N_2	$.238x10^{-3}$
N	$.310x10^{-3}$

Table B.4: Gladstone-Dale constants. Taken from Merzkirch (1987)

Appendix C Error analysis

This appendix describes the different sources of error for important physical variables used throughout this analysis.

P_o

The main source of error for P_o is in the calibration of the transducers. These transducers are recalibrated by the manufacturer every 3–4 years and this translates into an uncertainty of about $\pm 5\%$ based on the redundant readings from the two transducers used. The repeatability error for the free-stream conditions used here is represented by the standard deviations given in table 3.1.

u_s

The largest uncertainty for the shock speed comes from the fact that the shock is attenuated by the turbulent boundary layer as it travels down the shock tube. In these experiments, the value taken for u_s is obtained from the second-last timing interval. Although no rigorous error analysis has been done on the shock attenuation, it is estimated that the error incurred by taking the value of shock speed at this timing interval is about $\pm 4\%$. The error involved in measuring the rising times of the pressure transducers is less than 1%. The repeatability error varies from $\pm 2\%$ to $\pm 4\%$ for the conditions used here.

h_o

Since $h_o \approx u_s^2$ then any error for u_s doubles when calculating h_o. In this case we take the error in h_o to be about 8% based on the above discussion. The repeatability errors are given in table 3.1 as the standard deviation obtained for each condition.

Free-stream conditions

Based on the error analysis performed by Davis (1998) the uncertainties for the free stream conditions, based on a variation of $\pm 5\%$ P_o and $\pm 8\%$ in h_o, are as follows, $\pm 6\%$ in p_∞, $\pm 7.8\%$ in ρ_∞, $\pm 5.6\%$ in T_∞, $\pm 3\%$ in u_∞, and $\pm 1.6\%$ in T_{v_∞}. His calculations do not include the error in the

thermochemical model used in the nonequilibrium code or any effects due to the assumption of a laminar boundary layer in the nozzle.

Heat flux

Also based on the work of Davis (1998), the error in the heat flux comes from the voltage-to-temperature conversion (±1.7%), the uncertainty in the thermal properties of the thermocouples (±8%), and the unsteadiness of the heat flux trace during the averaging interval. The last error is calculated as twice the standard deviation of the experimental data during the test time. These three errors are taken into account in the error bars shown in the heat flux data presented in chapter 6.

Surface pressure

In these case there are one two important sources of error, the one due to the calibration which is about ±3% in this case, and the one due to unsteadiness of the signal during the test time. The latter is calculated similarly to the heat flux case. The error bars of the surface pressure data shown in chapter 6 take both errors into account.

Reaction rates

The error in the free-stream speed translates into an error in the temperature immediately after the shock (T_s) which goes as $\frac{\Delta T}{T} \approx 2\frac{\Delta u_\infty}{u_\infty}$. With this value and using equation 4.24 we can find the error in the rate reaction after the shock. For simplicity assume that $T = T_v$ after the shock. Then

$$\frac{\Delta k_{f_M}}{k_{f_M}} = \left(\eta + \frac{\theta_d}{T}\right)\frac{\Delta T}{T}, \tag{C.1}$$

which means that for the errors given before for u_∞ and taking typical values for T right after the shock, we obtain that for the case of N_2 flows, the error in the reaction rates is about $20\frac{\Delta u_\infty}{u_\infty}$, or about $20 \times 3\% = 60\%$.

Reaction rate parameter

In this case, the reaction rate parameter is affected by the errors in the free-stream velocity, temperature, and density. Differentiating the reaction rate parameter with respect to these variables and using their respective uncertainties, we obtain an error of about 80% in the reaction rate parameter.

Detachment distance

The error in the detachment distance comes mainly from two sources. The error associated with reading the detachment distance off the experimental interferograms and the error associated with the uncertainty in the free-stream conditions. The first error is about ± 1 mm and can result in an error of 1-40% in δ/d depending on the detachment distance and the diameter of the cone. The biggest errors being associated with the smallest cones close to incipient detachment. From the above analysis for the error in the rate coefficients due to free-stream uncertainties, we can obtain an estimate in the error in the detachment distance. The error bar in each of figures 5.12 and 5.15 to 5.16 represents the maximum error in the detachment distance due to the error in the reaction rate parameter. The error bars are computed at the region of maximum rate of change of the detachment distance. Both of these errors are taken into account in the error bars shown in figures 5.6 through 5.11.

Appendix D Data summary

D.1 Data summary for condition N_2 1.

(* denotes shots that are suspected of driver gas contamination)

Shot Number	1377	1378	1382	1498	1499	1500	1501	1519
diameter (cm)	8	8	8	8	8	8	8	4
angle(degrees)	61	61	65	70	58	55	70	70
P_{2R}(psig)	1225	1225	1175	1175	1175	1175	1175	1175
P_{CT} (KPa)	116	116	116	116	116	116	116	116
% He	95	95	97	97	97	97	97	97
P_{ST} (KPa)	42.5	42.5	40	40	40	40	40	40
dia. (in/in)	260/222	260/220	260/222	260/222	260/215	160/215	263/217	260/223
P_{4N} (MPa)	91.0	89.2	93.1	98.3	86.5	63.3	60.7	96.9
P_{4S} (MPa)	87.5	84.4	88.9	107.7	97.3	71.0	75.4	100.6
T_{amb} (K)	294	297	296	299	298	298	298	298
u_s (m/s)	4082	4082	4348	4412	4286	4082	4138	4286
P_{0N} (MPa)	54.6	56.2	52.5	50.3	48.2	43.2	43.8	47.05
P_{0S} (MPa)	57.9	58.8	55.1	62.0	60.8	54.2	54.6	60.41
P_{0a} (MPa)	56.2	57.5	53.8	54	53	54	52	53
t_{fire} (ms)	1.0	1.0	1.0	1.0	1.0	1.0	1.0	1.0
t_{del} (ms)	.15	.15	-	.12	.1	.12	.15	
t_{Kazu} (ms)	1.16	1.16	1.07	1.05	1.1	1.17	1.16	1.10
d_{epl} (cm)	14.7	14.9	15.0	14.4	13.5	13.3	14.5	14.2
δ/d	.003086	0.0	.00937	.0358	.00312	0.00	.0448	.0452
T_O (K)	8972	8995	9310	9321	9168	8966	8990	9168
h_0 (MJ/kg)	17.1	17.1	19.2	19.3	18.4	17.1	17.4	18.4
T_∞ (K)	2558	2560	2957	2977	2820	2588	2617	2812
P_∞(KPa)	24.3	24.0	24.8	25.1	24.4	23.9	22.7	24.1
$\rho_\infty(kg/m^3)$	.0317	.0314	.0277	.0279	.0184	.0171	.0174	.0284
u_∞(m/s)	5239	5241	5481	5486	5384	5242	5271	5386
M_∞	5.27	5.26	5.11	5.10	5.15	5.24	5.24	5.16
$[N2]$	.9821	.9818	.9620	.9614	.9696	.9804	.9871	.9697

Table D.1: Data summary for condition N_2 1.

Shot Number	1520	1521	1522	1523	1538	1655	1656	1657
diameter (cm)	4	4	4	4	4	2	2	2
angle(degrees)	75	66	63	60	56	56	60	63
P_{2R}(psig)	1175	1175	1175	1175	1175	1175	1175	1175
P_{CT} (KPa)	116	116	116	116	116	116	116	116
% He	97	97	97	97	97	97	97	97
P_{ST} (KPa)	40	40	40	40	40	40	40	40
dia. (in/in)	260/223	263/222	262/218	261/217	265/216	249/190	249/190	249/190
P_{4N} (MPa)	95.9	-	98.9	85.9	88.8	95.6	101.7	100.3
P_{4S} (MPa)	109.5	109.9	99.8	90.2	96.2	80.0	94.0	93.6
T_{amb} (K)	298	298	299	299	297	297	298	296
u_s (m/s)	4317	4348	4317	4255	4255	4286	4286	4225
P_{0N} (MPa)	47.97	47.31	45.7	38.4	47.5	52.0	53.1	53.6
P_{0S} (MPa)	60.30	60.25	58.2	49.7	59.1	53.5	54.4	53.7
P_{0a} (MPa)	53	54	53	49	53	52.8	53.7	53.7
t_{fire} (ms)	1.0	1.0	.95	.95	.9	1.0	1.0	1.0
t_{del} (ms)								
t_{Kazu} (ms)	1.10	1.08	1.10	1.1	1.13	1.09	1.09	1.1
d_{epl} (cm)	14.5	14.3	14.3	13.9	13.7	14.0	14.2	14.3
δ/d	.0823	.0217	.00694	0.0	0.0	0.0	0.0	0.0
T_O (K)	9201	9252	9203	9059	9133	9162	9181	9112
h_0 (MJ/kg)	18.6	18.9	18.6	18.0	18.2	18.4	18.4	18.0
T_∞ (K)	2846	2898	2851	2726	2779	2809	2821	2741
P_∞(KPa)	24.1	24.9	24.2	22.1	24.2	24.1	24.5	24.1
$\rho_\infty(kg/m^3)$	.0281	.0284	.0282	.0269	.0289	.0284	.0288	.0292
u_∞(m/s)	5410	5439	5410	5332	5361	5383	5391	5345
M_∞	5.15	5.13	5.14	5.18	5.17	5.16	5.15	5.19
$[N2]$	.9999	.9658	.9676	.9713	.9716	.9698	.9697	.9735

Data summary for condition N_2 1 (cont. 2/4)

Shot Number	1658	1659	1660	1903	1904	1925	1926	1927
diameter (cm)	2	2	2	8	8	16	16	16
angle(degrees)	66	70	75	61	75	70	70	63
P_{2R}(psig)	1175	1175	1175	1175	1175	1175	1175	1175
P_{CT} (KPa)	116	116	116	116	116	116	116	116
% He	97	97	97	97	97	97	97	97
P_{ST} (KPa)	40	41.5	41.5	40	40	40	45	45
dia. (in/in)	248/195	248/195	247/195	250/189	250/193	247/194	200/136	201/138
P_{4N} (MPa)	106.2	110.2	108.8	94.3	104	108	109	101
P_{4S} (MPa)	101.7	109.9	106.0	93.5	102	111	113	103
T_{amb} (K)	297	297	297	298	297	299.5	298	298.5
u_s (m/s)	4412	4412	4380	4170	4290	4320	4260	4230
P_{0N} (MPa)	54.1	55.5	54.4	52.8	54.4	56.3	54.7	54.3
P_{0S} (MPa)	53.1	54.4	53.4	53.8	55.4	53.3	52.5	52.4
P_{0a} (MPa)	53.6	54.9	53.9	53.3	54.9	54.8	53.6	53.4
t_{fire} (ms)	1.0	1.0	1.0	1.0	1.0	.9	.9	.9
t_{del} (ms)								
t_{Kazu} (ms)	1.05	1.06	1.06	.1	.1	.12	.15	.12
d_{epl} (cm)	14.3	14.4	14.3	1.16	1.12	1.1	1.12	1.13
δ/d	.0222	.0505	.0886	.1	.1	.1	.1	.1
T_O (K)	9309	9316	9264	0.0	.0595	.0221	.0268	0.0
h_0 (MJ/kg)	19.2	19.2	18.9	9060	9204	9240	9090	9050
T_∞ (K)	2968	2964	2914	17.4	18.3	18.5	17.6	17.4
P_∞(KPa)	25.0	25.5	24.9	2328	2301	2968	2964	2914
$\rho_\infty(kg/m^3)$	.0278	.0284	.0283	44.4	43.9	25.0	25.5	24.9
u_∞(m/s)	5480	5478	5447	.0906	.0912	.0278	.0284	.0283
M_∞	5.10	5.10	5.12	3335	3305	5480	5478	5447
$[N2]$	.9616	.9628	.9650	4.43	4.43	5.10	5.10	5.12

Data summary for condition N_2 1 (cont. 3/4)

Shot Number	1930	1931	1932	1933	1934	1947	1949	1951
diameter (cm)	16	16	16	16	16	8	8	8
angle(degrees)	60	60	75	56	66	61	75	75
P_{2R}(psig)	1175	1175	1175	1175	1175	1175	1175	1175
P_{CT} (KPa)	116	116	116	116	116	116	116	116
% He	97	97	97	97	97	97	97	97
P_{ST} (KPa)	44	45.5	45.5	46	46	47.5	46	48.5
dia. (in/in)	248/195	248/196	250/197	249/197	249/197	247/195	247/201	247/201
P_{4N} (MPa)	124	124	124	124	124	123	124	124
P_{4S} (MPa)	108	111	109	108	108	108	118	119
T_{amb} (K)	297	298	298	298	297.5	297	296.5	297
u_s (m/s)	3870	4200	4230	4260	4290	4110	4170	4140
P_{0N} (MPa)	53.7	54.8	53.9	55.5	54.0	57.5	60.3	60.6
P_{0S} (MPa)	52.4	53.1	52.8	53.6	52.3	54.3	56.8	56.9
P_{0a} (MPa)	53.0	53.9	53.4	54.6	53.2	55.9	58.6	58.7
t_{fire} (ms)	.9	.9	.9	.9	.93	.91	.91	.9
t_{del} (ms)								
t_{Kazu} (ms)	.15	.15	.15	.12	.12	.12	.12	.12
d_{epl} (cm)	1.32	1.1	1.14	1.13	1.11	1.23	1.2	1.22
δ/d	.1	.1	.1	.1	.1	.1	.1	.1
T_O (K)	0.0	0.0	–	.00199	.00199	0.0	.0713	.0744
h_0 (MJ/kg)	8650	9020	9040	9090	9100	8940	9070	9010
T_∞ (K)	15.3	17.3	17.4	17.6	17.7	16.7	17.3	16.9
P_∞(KPa)	2328	2301	2337	2331	2346	2346	1771	1836
$\rho_\infty(kg/m^3)$	44.4	43.9	45.4	44.9	47.0	47.0	22.6	22.7
u_∞(m/s)	.0906	.0912	.0923	.0915	.0952	.0952	.0429	.0416
M_∞	3335	3305	3338	3336	3344	3344	4679	4734
$[N2]$	4.43	4.43	4.43	4.43	4.43	4.43	5.64	5.61

Data summary for condition N_2 1 (cont. 4/4)

D.2 Data summary for condition N_2 2.

Shot Number	1376	1381	1503	1528	1532	1533	1534	1536
diameter (cm)	8	8	8	4	2	2	2	2
angle(degrees)	61	65	58	66	66	63	60	70
P_{2R}(psig)	1110	1110	1110	1110	1110	1110	1110	1110
P_{CT} (KPa)	116	116	116	116	116	116	116	116
% He	85	85	85	85	85	85	85	85
P_{ST} (KPa)	85	87	90	90	90	90	90	90
dia. (in/in)	263/215	260/222?	263/223	260/216	260/218	255/216	260/217	
P_{4N} (MPa)	80.7	93.1	-	72.0	85.1	89.3	91.8	96.2
P_{4S} (MPa)	76.4	74.8	102.0	78.6	90.9	93.9	97.3	105.2
T_{amb} (K)	298	297	298	298	298	297	299	299
u_s (m/s)	3141	3243	3352	3045	3191	3209	3279	3315
P_{0N} (MPa)	51.6	56.0	47.0	44.9	44.3	46.6	47.1	49.7
P_{0S} (MPa)	55.1	58.7	58.9	57.1	56.2	57.9	58.7	61.4
P_{0a} (MPa)	53.3	57.4	56	51	50	52	53	56
t_{fire} (ms)	1.0	1.0	1.0	.95	1.0	1.0	.9	1.0
t_{del} (ms)	.2	.2	.15					
t_{Kazu} (ms)	1.56	1.50	1.38	1.64	1.52	1.52	1.46	1.44
d_{epl} (cm)	14.6	14.7	14.2	14.4	14.0	14.0	14.0	14.2
δ/d	0.0	.0149	.00671	.0357	.0482	.018	.0130	.0754
T_O (K)	7153	7389	7524	6872	7127	7198	7347	7466
h_0 (MJ/kg)	10.2	10.7	11.1	9.51	10.1	10.3	10.7	11.0
T_∞ (K)	1278	1369	1438	1179	1277	1302	1363	1410
P_∞(KPa)	17.0	18.6	18.7	15.9	16.1	16.8	17.4	18.6
$\rho_\infty(kg/m^3)$	.0447	.0459	.0438	.0455	.0425	.0436	.0431	.0443
u_∞(m/s)	4181	4290	4361	4054	4173	4204	4276	4331
M_∞	5.90	5.86	5.82	5.94	5.89	5.88	5.85	5.83
$[N2]$	.9996	.9996	.9991	.9997	.9996	.9996	.9995	.9992

Table D.2: Data summary for condition N_2 2.

Shot Number	1638	1649	1650	1651	1652	1653	1654	1668
diameter (cm)	2	4	4	4	4	4	4	2
angle(degrees)	75	56	60	63	66	70	75	56
P_{2R}(psig)	1110	1110	1110	1110	1110	1110	1110	1110
P_{CT} (KPa)	116	116	116	116	116	116	116	116
% He	85	85	85	85	85	85	85	85
P_{ST} (KPa)	90	90	90	90	90	90	90	90
dia. (in/in)	262/219	265/217	265/208	247/213	247/208	250/202	250/190	262/217
P_{4N} (MPa)	107.3	102.7	-	108.4	107.1	106.7	94.3	106.9
P_{4S} (MPa)	-	97.9	73.8	104.5	101.2	103.1	122.2	99.3
T_{amb} (K)	297	298	299	296	299	296	298	297
u_s (m/s)	3333	3352	3061	3333	3352	3333	3261	3680
P_{0N} (MPa)	55.0	56.0	52.0	55.0	55.4	55.6	53.0	62.0
P_{0S} (MPa)	55.9	56.8	53.1	55.7	56.0	56.2	54.0	61.9
P_{0a} (MPa)	55.4	56.4	52.6	55.3	55.7	55.9	53.5	62.0
t_{fire} (ms)	.95	1.0	1.0	1.0	1.0	1.0	1.0	1.0
t_{del} (ms)								
t_{Kazu} (ms)	1.43	1.4	1.63	1.40	1.39	1.4	1.46	1.0
d_{epl} (cm)	14.2	14.1	14.3	14.4	14.5	14.7	14.9	13.9
δ/d	.264	0.0	0.0142	0.0	0.0451	.0997	.171	0.0
T_O (K)	7478	7531	6940	7473	7522	7485	6250	8124
h_0 (MJ/kg)	11.0	11.1	9.65	11.0	11.1	11.0	8.26	13.0
T_∞ (K)	1417	1441	1201	1414	1436	1416	1009	1771
P_∞(KPa)	18.4	18.9	16.5	18.3	18.5	18.4	16.1	22.6
$\rho_\infty(kg/m^3)$	.0437	.01441	.0464	.0436	.0434	.0437	.0539	.0429
u_∞(m/s)	4338	4363	4082	4336	4361	4342	3787	4679
M_∞	5.83	5.81	5.93	5.83	5.82	5.83	5.98	5.64
$[N2]$	.9992	.9991	.9997	.9992	.9991	.9994	.9999	.9977

Data summary for condition N_2 2 (cont. 2/4)

Shot Number	1658	1659	1660	1903	1904	1925	1926	1927
diameter (cm)	2	2	2	8	8	16	16	16
angle(degrees)	66	70	75	61	75	70	70	63
P_{2R}(psig)	1175	1175	1175	1175	1175	1175	1175	1175
P_{CT} (KPa)	116	116	116	116	116	116	116	116
% He	97	97	97	97	97	97	97	97
P_{ST} (KPa)	40	41.5	41.5	40	40	40	45	45
dia. (in/in)	248/195	248/195	247/195	250/189	250/193	247/194	200/136	201/138
P_{4N} (MPa)	106.2	110.2	108.8	94.3	104	108	109	101
P_{4S} (MPa)	101.7	109.9	106.0	93.5	102	111	113	103
T_{amb} (K)	297	297	297	298	297	299.5	298	298.5
u_s (m/s)	4412	4412	4380	4170	4290	4320	4260	4230
P_{0N} (MPa)	54.1	55.5	54.4	52.8	54.4	56.3	54.7	54.3
P_{0S} (MPa)	53.1	54.4	53.4	53.8	55.4	53.3	52.5	52.4
P_{0a} (MPa)	53.6	54.9	53.9	53.3	54.9	54.8	53.6	53.4
t_{fire} (ms)	1.0	1.0	1.0	1.0	1.0	.9	.9	.9
t_{del} (ms)								
t_{Kazu} (ms)	1.05	1.06	1.06	.1	.1	.12	.15	.12
d_{epl} (cm)	14.3	14.4	14.3	1.16	1.12	1.1	1.12	1.13
δ/d	.0222	.0505	.0886	.1	.1	.1	.1	.1
T_O (K)	9309	9316	9264	0.0	.0595	.0221	.0268	0.0
h_0 (MJ/kg)	19.2	19.2	18.9	9060	9204	9240	9090	9050
T_∞ (K)	2968	2964	2914	17.4	18.3	18.5	17.6	17.4
P_∞(KPa)	25.0	25.5	24.9	2328	2301	2968	2964	2914
$\rho_\infty(kg/m^3)$	.0278	.0284	.0283	44.4	43.9	25.0	25.5	24.9
u_∞(m/s)	5480	5478	5447	.0906	.0912	.0278	.0284	.0283
M_∞	5.10	5.10	5.12	3335	3305	5480	5478	5447
$[N2]$	.9616	.9628	.9650	4.43	4.43	5.10	5.10	5.12

Data summary for condition N_2 2 (cont. 3/4)

Shot Number	1930	1931	1932	1933	1934	1947	1949	1951
diameter (cm)	16	16	16	16	16	8	8	8
angle(degrees)	60	60	75	56	66	61	75	75
P_{2R}(psig)	1175	1175	1175	1175	1175	1175	1175	1175
P_{CT} (KPa)	116	116	116	116	116	116	116	116
% He	97	97	97	97	97	97	97	97
P_{ST} (KPa)	44	45.5	45.5	46	46	47.5	46	48.5
dia. (in/in)	248/195	248/196	250/197	249/197	249/197	247/195	247/201	247/201
P_{4N} (MPa)	124	124	124	124	124	123	124	124
P_{4S} (MPa)	108	111	109	108	108	108	118	119
T_{amb} (K)	297	298	298	298	297.5	297	296.5	297
u_s (m/s)	3870	4200	4230	4260	4290	4110	4170	4140
P_{0N} (MPa)	53.7	54.8	53.9	55.5	54.0	57.5	60.3	60.6
P_{0S} (MPa)	52.4	53.1	52.8	53.6	52.3	54.3	56.8	56.9
P_{0a} (MPa)	53.0	53.9	53.4	54.6	53.2	55.9	58.6	58.7
t_{fire} (ms)	.9	.9	.9	.9	.93	.91	.91	.9
t_{del} (ms)								
t_{Kazu} (ms)	.15	.15	.15	.12	.12	.12	.12	.12
d_{epl} (cm)	1.32	1.1	1.14	1.13	1.11	1.23	1.2	1.22
δ/d	.1	.1	.1	.1	.1	.1	.1	.1
T_O (K)	0.0	0.0	–	.00199	.00199	0.0	.0713	.0744
h_0 (MJ/kg)	8650	9020	9040	9090	9100	8940	9070	9010
T_∞ (K)	15.3	17.3	17.4	17.6	17.7	16.7	17.3	16.9
P_∞(KPa)	2328	2301	2337	2331	2346	2346	1771	1836
$\rho_\infty(kg/m^3)$	44.4	43.9	45.4	44.9	47.0	47.0	22.6	22.7
u_∞(m/s)	.0906	.0912	.0923	.0915	.0952	.0952	.0429	.0416
M_∞	3335	3305	3338	3336	3344	3344	4679	4734
$[N2]$	4.43	4.43	4.43	4.43	4.43	4.43	5.64	5.61

Data summary for condition N_2 2 (cont. 4/4)

D.3 Data summary for condition N_2 3.

Shot Number	1371	1372	1379	1388	1484	1485	1486	1535
diameter (cm)	8	8	8	8	8	8	8	2
angle(degrees)	61	61	65	75	55	55	58	56
P_{2R}(psig)	435	435	435	435	435	435	435	435
P_{CT} (KPa)	58	58	58	58	58	58	58	58
% He	95	95	95	95	95	95	95	95
P_{ST} (KPa)	20	20	23	23	23	23	23	23
dia. (in/in)		187/133	187/133	187/131	187/130	187/134	187/135	187/133
P_{4N} (MPa)	49.1	46.2	44.4	38.9	36.9	41.0	59.8	50.8
P_{4S} (MPa)	53.7	39.9	40.8	43.7	40.0	44.3	64.6	54.2
T_{amb} (K)	297	296	294.5	297	298	298	299	297
u_s (m/s)	4380	4255	3846	3871	3390	3974	4317	4110
P_{0N} (MPa)	19.8	19.4	19.1	19.0	16.8	17.3	20.4	16.8
P_{0S} (MPa)	22.1	21.8	21.3	21.4	22.8	23.5	26.8	21.7
P_{0a} (MPa)	21.0	20.6	20.2	20.2	20	20	24	19
t_{fire} (ms)	1.0	1.0	1.0	1.0	1.0	1.0	1.0	.9
t_{del} (ms)	.1	.1	.1	.1	.2	.1	.1	
t_{Kazu} (ms)	.98	1.0	1.14	1.15	1.42	1.09	1.01	1.06
d_{epl} (cm)	11.7	12.6	13.1	13.4	11.0	11.2	11.5	12.8
δ/d	.00459	no p	0.0131	unsteady	.0179	.00492	.00464	0.0
T_O (K)	8699	8553	8067	8094	7523	8196	8703	8288
h_0 (MJ/kg)	18.3	17.1	14.5	14.4	11.8	15.2	17.6	15.9
T_∞ (K)	2602	2483	2035	2056	1632	2171	2607	2249
P_∞(KPa)	9.38	17.4	8.21	8.16	7.60	8.62	11.2	8.09
$\rho_\infty(kg/m^3)$	.0117	.0120	.0134	.0132	.0156	.0132	.0140	.0119
u_∞(m/s)	5292	5190	4849	4869	4490	4936	5256	5016
M_∞	5.21	5.24	5.44	5.44	5.63	5.36	5.19	5.34
$[N2]$	.9339	.9455	.9776	.9762	.9924	.9703	.9458	.9616

Table D.3: Data summary for condition N_2 3.

Shot Number	1629	1630	1631	1632	1633	1634	1639	1644
diameter (cm)	4	4	4	4	4	4	2	2
angle(degrees)	75	70	66	63	60	56	70	63
P_{2R}(psig)	435	435	435	435	435	435	435	435
P_{CT} (KPa)	58	58	58	58	58	58	58	58
% He	95	95	95	95	95	95	95	95
P_{ST} (KPa)	23	23	23	23	23	23	23	23
dia. (in/in)	187/117	187/117	187/117	187/119	187/119	187/119	187/119	187/119
P_{4N} (MPa)	51.1	54.5	54.2	53.3	53.4	55.4	53.6	57.2
P_{4S} (MPa)	47.1	50.2	50.0	49.1	49.1	51.0	49.5	52.4
T_{amb} (K)	297	297	298	297	298	298	300	295
u_s (m/s)	4225	4380	4317	4317	4317	4348	4054	4255
P_{0N} (MPa)	21.5	21.4	21.7	20.6	21.4	21.5	18.7	21.5
P_{0S} (MPa)	21.8	21.7	22.3	21.1	21.9	22.2	18.8	21.6
P_{0a} (MPa)	21.7	21.6	22.0	20.8	21.7	21.8	18.7	21.6
t_{fire} (ms)	.9	.9	.9	.9	.9	.9	.9	.9
t_{del} (ms)								
t_{Kazu} (ms)	1.02	.976	.99	.977	1.00	.98	1.05	1.0
d_{epl} (cm)	14.3	14.2	13.9	13.9	13.7	13.5	13.7	13.8
δ/d	.178	.0801	.0366	0.0	0.	0.	.147	0.0572
T_O (K)	8519	8664	8622	8570	8610	8643	8222	8541
h_0 (MJ/kg)	17.0	17.9	17.3	17.4	17.5	17.8	15.5	17.1
T_∞ (K)	2420	2558	2519	2481	2512	2545	2184	2447
P_∞(KPa)	9.29	9.49	9.66	9.07	9.55	9.68	7.73	9.37
$\rho_\infty(kg/m^3)$	.0126	.0121	.0126	.0120	.0125	.0125	.0117	.0126
u_∞(m/s)	5156	5261	5226	5201	5220	5242	4975	5171
M_∞	5.29	5.23	5.24	5.26	5.24	5.23	5.38	5.27
$[N2]$	.9535	.9402	.9458	.9457	.9457	.9430	.9651	.9513

Data summary for condition N_2 3 (cont. 2/4)

Shot Number	1645	1646	1647	1648	1892	1893	1894	1907
diameter (cm)	2	2	2	2	8	8	8	16
angle(degrees)	60	75	66	56	58	70	75	56
P_{2R}(psig)	435	435	435	435	435	435	435	435
P_{CT} (KPa)	58	58	58	58	58	58	58	58
% He	95	95	95	95	95	95	95	95
P_{ST} (KPa)	23	23	23	23	23	23	23	23
dia. (in/in)	187/120	187/121	187/121	187/121	202/126	203/125	203/131	200/130
P_{4N} (MPa)	50.7	53.4	49.3	49.3	48.6	44.7	52.6	54.3
P_{4S} (MPa)	46.5	48.5	45.0	44.9	46.8	43.0	51.0	52.5
T_{amb} (K)	299	295	297	296	300	300	300	297
u_s (m/s)	4255	4138	4225	4167	4030	4000	4140	4170
P_{0N} (MPa)	19.3	20.9	19.7	20.0	18.9	17.7	18.9	18.7
P_{0S} (MPa)	19.3	21.5	19.4	20.0	20.5	19.2	20.2	20.0
P_{0a} (MPa)	19.3	21.2	19.5	20.0	19.7	18.5	19.5	19.4
t_{fire} (ms)	.9	.9	.9	.9	1.0	1.0	1.0	.9
t_{del} (ms)								
t_{Kazu} (ms)	.99	1.04	.99	1.01	.05	.03	.02	.09
d_{epl} (cm)	13.5	14.1	13.8	13.7	1.02–.07	1.07	1.03	1.02
δ/d	.0286	.175	.0908	0.0	.1	.1	.1	.1
T_O (K)	8447	8409	8424	8388	.00338	.0458	.0827	.00333
h_0 (MJ/kg)	16.8	16.3	16.7	16.4	8240	8160	8340	8360
T_∞ (K)	2385	2324	2359	2321	15.2	14.9	15.9	16.0
P_∞(KPa)	8.33	8.94	8.33	8.50	2301	2337	2331	2346
$\rho_\infty(kg/m^3)$	.0115	.0127	.0116	.0121	43.9	45.4	44.9	47.0
u_∞(m/s)	5128	5081	5110	5079	.0912	.0923	.0915	.0952
M_∞	5.29	5.33	5.31	5.32	3305	3338	3336	3344
$[N2]$	.9503	.9602	.9531	.9578	4.43	4.43	4.43	4.43

Data summary for condition N_2 3 (cont. 3/4)

Shot Number	1909	1911	1916	1918	1919
diameter (cm)	16	16	16	16	16
angle(degrees)	63	75	60	70	66
P_{2R}(psig)	435	435	435	435	435
P_{CT} (KPa)	58	58	58	58	58
% He	95	95	95	95	95
P_{ST} (KPa)	23	23	24	23	23
dia. (in/in)	201/130	200/128	200/130	202/131	202/131
P_{4N} (MPa)	53.0	54.5	31.1	29.8	39.8
P_{4S} (MPa)	50.9	52.9	51.3	51.3	52.4
T_{amb} (K)	298	297.5	298.5	297.5	297
u_s (m/s)	4170	4170	4080	4170	4000
P_{0N} (MPa)	18.4	19.4	—	—	—
P_{0S} (MPa)	19.6	19.4	19.8	18.8	19.5
P_{0a} (MPa)	19.0	19.4	19.8	18.8	19.5
t_{fire} (ms)	.9	.9	.9	.9	.88
t_{del} (ms)					
t_{Kazu} (ms)	.08	.1	.09	.02	.05
d_{epl} (cm)	1.0	1.02	1.05	1.02	1.10
δ/d	.1	.1	.1	.1	.1
T_O (K)	0.0	.0706	0.0	.028	.00922
h_0 (MJ/kg)	8340	8360	8280	8340	8200
T_∞ (K)	16.0	16.0	15.4	15.9	15.0
P_∞(KPa)	1771	1836	2301	2337	2331
$\rho_\infty(kg/m^3)$	22.6	22.7	43.9	45.4	44.9
u_∞(m/s)	.0429	.0416	.0912	.0923	.0915
M_∞	4679	4734	3305	3338	3336
$[N2]$	5.64	5.61	4.43	4.43	4.43

Data summary for condition N_2 3 (cont. 4/4)

D.4 Data summary for condition N_2 4.

Shot Number	1380	1387	1488	1489	1495	1529	1530	1531
diameter (cm)	8	8	8	8	8	2	2	2
angle(degrees)	65	75	58	70	55	56	75	70
P_{2R}(psig)	550	550	611	611	611	611	611	611
P_{CT} (KPa)	74	74	82.2	82.2	82.2	82.2	82.2	82.2
% He	84	84	84	84	84	84	84	84
P_{ST} (KPa)	50	50	60	60	60	60	60	60
dia. (in/in)		187/131	187/135	187/132	187/135	187/135	187/135	187/135
P_{4N} (MPa)	46.2	49.0	53.1	53.3	50.2	49.6	52.2	53.0
P_{4S} (MPa)	46.7	45.4	55.9	57.3	54.0	52.1	54.2	56.7
T_{amb} (K)	297	296	297	298	299	299	298	299
u_s (m/s)	3061	3046	3125	3175	3141	3015	3061	3158
P_{0N} (MPa)	23.9	23.4	25.8	26.1	26.7	23.9	24.3	25.2
P_{0S} (MPa)	26.6	26.1	33.8	34.2	34.4	31.2	31.6	33.2
P_{0a} (MPa)	25.2	24.7	30	30	30	28	28	29
t_{fire} (ms)	1.0	1.0	1.0	1.0	1.0	1.0	1.0	1.0
t_{del} (ms)	.2	.2	.2	.2	.2			
t_{Kazu} (ms)	1.51	1.52	1.48	1.45	1.47	1.57	1.53	1.49
d_{epl} (cm)	13.3	13.7	12.0	13.2	11.4	13.2	14.1	13.8
δ/d	.0180	.0998	0.0	.0534	-	.0166	.119	.0674
T_O (K)	6810	6720	6821	6913	6856	6700	6786	6852
h_0 (MJ/kg)	9.63	8.90	9.28	9.82	9.67	9.32	9.53	9.68
T_∞ (K)	1211	1174	1210	1239	1227	1162	1189	1213
P_∞(KPa)	8.16	7.96	9.93	9.78	10.1	8.95	8.87	9.29
$\rho_\infty(kg/m^3)$	.0227	.0228	.0276	.0266	.0277	.0260	.0251	.0258
u_∞(m/s)	4071	4029	4062	4109	4077	4011	4053	4082
M_∞	5.89	5.92	5.88	5.88	5.87	5.92	5.92	5.90
$[N2]$	.9989	.9991	.9992	.9991	.9991	.8953	.9992	.9991

Table D.4: Data summary for condition N_2 4.

Shot Number	1545	1546	1547	1635	1636	1640	1641	1642
diameter (cm)	2	2	2	4	4	4	4	4
angle(degrees)	66	63	60	63	60	66	70	75
P_{2R}(psig)	611	611	611	611	611	611	611	611
P_{CT} (KPa)	82.2	82.2	82.2	82.2	82.2	82.2	82.2	82.2
% He	84	84	84	84	84	84	84	84
P_{ST} (KPa)	60	60	60	60	63	60	60	60
dia. (in/in)	187/134	187/133	187/134	187/119	187/119	187/119	187/119	187/119
P_{4N} (MPa)	45.7	47.4	51.7	54.4	53.0	55.4	52.9	52.4
P_{4S} (MPa)	55.3	55.4	54.5	50.0	49.3	51.5	48.8	48.9
T_{amb} (K)	300	300	299	297	297	298	300	296
u_s (m/s)	3000	3015	3000	3077	3077	3015	3077	3093
P_{0N} (MPa)	25.2	26.1	26.2	29.6	31.0	27.3	27.6	28.1
P_{0S} (MPa)	28.6	29.4	29.5	29.9	31.3	27.8	27.9	28.0
P_{0a} (MPa)	27	28	28	29.8	31.2	27.6	27.8	28.0
t_{fire} (ms)	1.01	1.0	1.00	1.0	1.0	.95	.95	.95
t_{del} (ms)								
t_{Kazu} (ms)	1.5	1.5	1.5	1.54	1.55	1.54	1.49	1.49
d_{epl} (cm)	13.9	13.6	13.7	14.5	14.3	14.3	14.7	15.0
δ/d	.0505	.0281	.00686	.0418	.0241	.0681	.1273	.2113
T_O (K)	6588	6700	6522	6726	6731	6550	6700	6700
h_0 (MJ/kg)	9.07	9.32	9.32	9.36	9.36	8.99	9.33	9.32
T_∞ (K)	1121	1160	1159	1160	1160	1104	1154	1152
P_∞(KPa)	8.43	8.88		9.29	9.76	8.52	8.63	8.64
$\rho_\infty(kg/m^3)$	.0254	.0258	.0258	.0270	.0283	.0260	.0252	.0253
u_∞(m/s)	3962	4012	4012	4021	4020	3944	4014	4014
M_∞	5.95	5.93	5.93	5.94	5.94	5.96	5.95	5.95
$[N2]$	.9994	.9993	.9993	.9993	.9993	.9994	.9992	.9993

Data summary for condition N_2 4 (cont. 2/3)

Shot Number	1643	1888	1906	1908	1910	1914	1922	1923
diameter (cm)	4	8	16	16	16	16	16	16
angle(degrees)	56	61	75	56	63	70	60	66
P_{2R}(psig)	611	611	611	611	611	611	611	611
P_{CT} (KPa)	82.2	82.2	82.2	82.2	82.2	82.2	82.2	82.2
% He	84	84	84	84	84	84	84	84
P_{ST} (KPa)	60	60	61	60	60	60	60	60
dia. (in/in)	187/119	203/123	201/129	200/130	200/131	201/130	200/136	200/137
P_{4N} (MPa)	52.8	51.9	55.5	55.3	55.7	30.3	53.2	53.5
P_{4S} (MPa)	48.5	49.6	52.4	53.6	53.2	52.4	54.3	60.4
T_{amb} (K)	299	298.5	297.5	300	299	297	298.5	296.5
u_s (m/s)	3077	2910	2970	3000	2990	2880	3020	3050
P_{0N} (MPa)	28.3	25.7	26.8	27.5	26.5	—	29.6	29.3
P_{0S} (MPa)	28.7	27.0	28.4	29.1	27.0	28.2	28.1	28.8
P_{0a} (MPa)	28.6	26.3	27.6	28.3	26.8	28.2	28.8	29.1
t_{fire} (ms)	.95	1.1	1.0	.97	.97	1.0	.95	.95
t_{del} (ms)								
t_{Kazu} (ms)	1.49	.2	.15	.15	.18	.13	.13	.15
d_{epl} (cm)	13.7	1.64	1.59	1.57	1.57	1.67	1.56	1.52
δ/d	0.	.1	.1	.1	.1	.1	.1	.1
T_O (K)	6691	.00288	.0868	0.0	.0022	.0459	0.0	.0196
h_0 (MJ/kg)	9.36	6940	6430	6540	6440	6660	6580	6640
T_∞ (K)	1165	9.39	8.42	8.65	8.47	8.92	8.74	8.87
P_∞(KPa)	9.07	2968	2331	2497	2493	2914	1771	2493
$\rho_\infty(kg/m^3)$	.0262	25.0	44.9	47.4	30.3	24.9	22.6	30.3
u_∞(m/s)	4020	.0278	.0915	.0863	.0522	.0283	.0429	.0522
M_∞	5.93	5480	3336	3539	3697	5447	4679	3697
$[N2]$	.9993	5.10	4.43	4.45	4.51	5.12	5.64	4.51

Data summary for condition N_2 4 (cont. 3/3)

D.5 Data summary for condition CO_2 2.

Shot Number	1369	1370	1383	1386	1481	1483	1490	1491
diameter (cm)	8	8	8	8	8	8	8	8
angle(degrees)	61	61	65	75	55	55	58	58
P_{2R}(psig)	550	550	550	550	550	550	550	550
P_{CT} (KPa)	74	74	74	74	74	74	74	74
% He	84	84	84	84	84	84	84	84
P_{ST} (KPa)	31.8	31.8	40	40	40	35	42	38
dia. (in/in)	187/135	187/135	187/132	187/131	187/130	187/130	187/132	187/132
P_{4N} (MPa)	50.2	51.7	42.8	46.9	40.8	41.0	47.5	48.0
P_{4S} (MPa)	47.3	47.8	39.4	44.1	43.8	43.3	50.1	51.0
T_{amb} (K)	298	297	297	294	298	298	297	296
u_s (m/s)	2844	2899	2553	2620	2666	2778	2778	2844
P_{0N} (MPa)	23.0	23.3	23.1	22.5	20.5	19.7	21.4	21.4
P_{0S} (MPa)	26.5	26.8	26.3	25.8	27.7	26.8	29.0	29.0
P_{0a} (MPa)	24.8	25.1	24.7	24.2	24	23	25	25
t_{fire} (ms)	1.0	1.0	1.0	1.0	1.0	1.0	1.1	1.0
t_{del} (ms)	.2	.2	.2	.2	.2	.2	.2	-
t_{Kazu} (ms)	1.06	1.00	1.26	1.2	1.17	1.08	1.01	1.04
d_{epl} (cm)	12.8	12.7	13.0	13.8	11.5	11.6	11.8	12.0
δ/d	no view	.00291	.00588	.0704	no p	.00236	0.0	0.0
T_O (K)	3926	3986	3588	3647	3679	3815	3808	3893
h_0 (MJ/kg)	7.05	7.29	5.5	5.72	5.87	6.55	6.45	6.88
T_∞ (K)	1858	1895	1496	1555	1601	1751	1740	1990
P_∞(KPa)	17.0	16.4	15.4	15.2	15.9	15.7	17.0	21.2
$\rho_\infty(kg/m^3)$	.0448	.0423	.0523	.0493	.0499	.0446	.0487	.0466
u_∞(m/s)	3009	3039	2766	2812	2831	2932	2921	2982
M_∞	4.48	4.48	4.64	4.61	4.57	4.50	4.51	4.48
$[O]$	.0010	.0019				.0002		.0005
$[CO2]$	.7841	.7660	.8783	.8629	.8540	.8114	.8225	.7039
$[CO]$	.1432	.1554	.0812	.0914	.0974	.1257	.1184	.1201
$[O2]$	.0711	.0768	.0496	.0457	.0487	.0628	.0591	.0597

Table D.5: Data summary for condition CO_2 2.

Shot Number	1492	1493	1494	1496	1537	1540	1542	1543
diameter (cm)	8	8	8	8	2	2	2	2
angle(degrees)	58	58	70	70	66	60	63	70
P_{2R}(psig)	550	550	550	550	550	550	550	550
P_{CT} (KPa)	74	74	74	74	74	74	74	74
% He	84	84	84	84	84	84	84	84
P_{ST} (KPa)	38	31	30	30	40	40	40	40
dia. (in/in)	187/132	187/133	187/133	187/133	187/133	187/133	187/134	187/134
P_{4N} (MPa)	48.0	48.8	48.5	48.0	50.1	50.2	41.8	38.9
P_{4S} (MPa)	50.9	51.5	50.9	50.9	53.3	53.1	50.3	49.9
T_{amb} (K)	299	298	299	297	297	297	298	299
u_s (m/s)	2871	3015	3030	3015	2778	2778	2700	2691
P_{0N} (MPa)	20.6	21.1	20.9	20.4	20.8	20.2	22.3	23.6
P_{0S} (MPa)	28.2	28.4	27.8	27.2	28.1	27.0	24.8	26.4
P_{0a} (MPa)	24	25	24	24	25	24	24	25
t_{fire} (ms)	1.0	1.0	1.0	1.0	1.1	1.1	2.105	1.1
t_{del} (ms)	.2	.2	.2	.2				
t_{Kazu} (ms)	1.02	.93	.92	.93				
d_{epl} (cm)	11.6	11.7	13.1	12.9	13.4	13.3	13.2	13.6
δ/d	.0062	0.0	0.0279	.0253	.0241	.0222	.0236	.0494
T_O (K)	3907	4107	4114	4097	3818	3825	3727	3733
h_0 (MJ/kg)	6.98	7.99	8.06	7.97	6.51	6.57	6.10	6.10
T_∞ (K)	1847	2016	2011	2000	1743	1752	1645	1648
P_∞(KPa)	16.8	17.8	16.7	16.7	16.5	15.9	15.6	16.5
$\rho_\infty(kg/m^3)$	.0446	.0423	.0396	.0400	.0472	.0452	.0456	.0491
u_∞(m/s)	2995	3133	3145	3132	2933	2940	2869	2872
M_∞	4.48	4.47	4.48	4.48	4.52	4.52	4.56	4.56
$[O]$	.0009	.0060	.0065	.0059	.0001	.0001		
$[CO2]$	.7869	.7198	.7116	.7181	.8196	.8131	.8412	.8435
$[CO]$	.1418	.1848	.1901	.1860	.1203	.1246	.1059	.1043
$[O2]$	.0705	.0894	.0918	.0901	.0601	.0622	.0529	.0522

Data summary for condition CO_2 2 (cont. 2/5)

Shot Number	1544	1548	1623	1624	1625	1626	1627	1628
diameter (cm)	2	2	4	4	4	4	4	4
angle(degrees)	75	56	56	56	70	66	63	60
P_{2R}(psig)	550	550	550	550	550	550	550	550
P_{CT} (KPa)	74	74	74	74	74	74	74	74
% He	86	84	84	84	84	84	84	84
P_{ST} (KPa)	40	40	40	40	40	40	40	40
dia. (in/in)	187/134	187/133	187/133	187/129	187/129	187/129	187/122	187/117
P_{4N} (MPa)	42.3	47.8	66.1	56.9	62.5	61.4	60.0	52.2
P_{4S} (MPa)	51.7	50.3	55.7	46.6	58.0	56.6	55.1	48.3
T_{amb} (K)	299	300	297	297	297	297	297	297
u_s (m/s)	2703	2703	2941	2765	2927	2913	2885	2804
P_{0N} (MPa)	22.9	21.9	26.8	26.3	27.3	24.9	26.5	25.4
P_{0S} (MPa)	25.9	24.9	27.5	27.3	27.6	25.1	26.9	26.3
P_{0a} (MPa)	24	23	27.1	26.8	27.5	25.0	26.7	25.8
t_{fire} (ms)	1.1	1.1	1.1	1.1	1.1	1.1	1.1	1.1
t_{del} (ms)								
t_{Kazu} (ms)			.98	1.09	.99	1.0	1.01	1.07
d_{epl} (cm)	13.7	13.2	14.0	14.6	14.5	14.4	14.3	14.1
δ/d	.0961	.0120	0.	.1395	.0612	.0213	.0168	.0168
T_O (K)	3729	3717	4010	3829	4000	3952	3948	3850
h_0 (MJ/kg)	6.10	6.08	7.40	6.51	7.35	7.18	7.10	6.64
T_∞ (K)	1644	1635	1931	1747	1920	1876	1873	1773
P_∞(KPa)	15.4	14.9	18.4	17.4	18.5	16.7	17.9	17.0
$\rho_\infty(kg/m^3)$	.0470	.0456	.0465	.0496	.0478	.0437	.0469	.0475
u_∞(m/s)	2872	2865	3064	2938	3057	3030	3022	2955
M_∞	4.57	4.57	4.48	4.53	4.49	4.50	4.49	4.52
$[O]$			.222e-2	.937e-4	.190e-2	.135e-2	.107e-2	.193e-3
$[CO2]$	.8407	.8398	.7669	.8237	.7724	.7769	.7864	.8135
$[CO]$	.1062	.1068	.1547	.1175	.1512	.1483	.1421	.1243
$[O2]$	.0531	.0534	.0762	.0587	.0746	.0735	.0705	.0621

Data summary for condition CO_2 2 (cont. 3/5)

Shot Number	1889	1890	1891	1905	1912	1913	1915	1920
diameter (cm)	8	8	8	16	16	16	16	16
angle(degrees)	75	65	70	56	63	75	60	70
P_{2R}(psig)	550	550	550	550	550	550	550	550
P_{CT} (KPa)	74	74	74	74	74	74	74	74
% He	84	84	84	84	84	84	84	84
P_{ST} (KPa)	38	40	40	42	40	41	40	40
dia. (in/in)	203/120	200/125	203/128	200/120	200/128	202/130	201/131	201/133
P_{4N} (MPa)	47.3	50.1	50.6	49.8	48.8	52.1	30.9	45.0
P_{4S} (MPa)	45.2	48.6	47.7	48.0	46.2	49.9	50.9	59.3
T_{amb} (K)	297	296	298	297	298	297.5	298	298
u_s (m/s)	2650	2730	2730	2650	2620	2670	2700	2750
P_{0N} (MPa)	21.9	23.5	23.5	23.8	22.8	24.5	—	—
P_{0S} (MPa)	23.4	25.3	25.5	25.6	23.0	24.1	24.3	23.7
P_{0a} (MPa)	22.7	24.4	24.5	24.7	22.9	24.3	24.3	23.7
t_{fire} (ms)	1.0	1.0	1.0	.85	.85	.87	.88	.87
t_{del} (ms)								
t_{Kazu} (ms)	.1	.12	.12	.1	.15	.15	.13	.1
d_{epl} (cm)	.98–1.05	.97	.97	1.02	1.04	1.00	.98	.95
δ/d	.1	.1	.1	.1	.1	.1	.1	.1
T_O (K)	.0657	.00538	.0266	0.0	0.0	.0583	0.0	.0184
h_0 (MJ/kg)	3670	3760	3760	3670	3630	3690	3760	3770
T_∞ (K)	6.47	6.79	6.80	6.43	6.28	6.51	6.68	6.88
P_∞(KPa)	2964	2914	2328	2337	2968	2964	2328	2346
$\rho_\infty(kg/m^3)$	25.5	24.9	44.4	45.4	25.0	25.5	44.4	47.0
u_∞(m/s)	.0284	.0283	.0906	.0923	.0278	.0284	.0906	.0952
M_∞	5478	5447	3335	3338	5480	5478	3335	3344
$[O]$	.9628	.9650			.9616	.9628		
$[CO2]$			.0112	.0114			.0112	.0114
$[CO]$			.7040	.7026			.7040	.7031
$[O2]$			.1936	.1945			.1936	.1941

Data summary for condition CO_2 2 (cont. 4/5)

Shot Number	1921
diameter (cm)	16
angle(degrees)	66
P_{2R}(psig)	550
P_{CT} (KPa)	74
% He	84
P_{ST} (KPa)	39
dia. (in/in)	200/133
P_{4N} (MPa)	46.2
P_{4S} (MPa)	59.0
T_{amb} (K)	298
u_s (m/s)	2700
P_{0N} (MPa)	—
P_{0S} (MPa)	23.2
P_{0a} (MPa)	23.2
t_{fire} (ms)	.88
t_{del} (ms)	
t_{Kazu} (ms)	.1
d_{epl} (cm)	.98
δ/d	.1
T_O (K)	0.0
h_0 (MJ/kg)	3720
T_∞ (K)	6.67
P_∞(KPa)	2497
$\rho_\infty(kg/m^3)$	47.4
u_∞(m/s)	.0863
M_∞	3539
$[O]$	
$[CO2]$	.0247
$[CO]$	.6015
$[O2]$	.2575

Data summary for condition CO_2 2 (cont. 5/5)

D.6 Data summary for condition CO_2 3.

Shot Number	1384	1385	1524	1525	1526	1527	1539	1549
diameter (cm)	8	8	4	4	4	4	4	4
angle(degrees)	65	75	75	66	60	70	63	56
P_{2R}(psig)	1500	1425	1425	1425	1425	1425	1425	1425
P_{CT} (KPa)	124	124	124	124	124	124	124	124
% He	86	86	86	86	86	86	86	86
P_{ST} (KPa)	60	60	60	60	60	60	60	60
dia. (in/in)	260/222	260/222	255/215	254/212	254/212	260/213	265/216	254/213
P_{4N} (MPa)	-	99.9	96.7	93.2	96.3	82.3	97.2	98.4
P_{4S} (MPa)	114.2	94.6	105.4	99.0	101.7	85.0	103.4	104.5
T_{amb} (K)	298	296	298	299	300	298	299	299
u_s (m/s)	2956	2804	3191	3141	3141	2941	3192	3158
P_{0N} (MPa)	65.8	64.4	48.2	52.9	52.5	52.7	53.0	62.2
P_{0S} (MPa)	70.8	69.7	61.7	67.9	70.4	68.4	68.7	68.8
P_{0a} (MPa)	68.3	67.1	61	64	64	63	64	66
t_{fire} (ms)	1.0	1.1	.95	.96	1.05	1.05	1.1	1.05
t_{del} (ms)	.2	.25						
t_{Kazu} (ms)	.98	1.08						
d_{epl} (cm)	15.9	16.6	15.2	15.2	14.7	15.2	15.1	14.6
δ/d	.00707	unsteady	.0799	.0161	.0134	.0393	0.	.00763
T_O (K)	4315	4133	4537	4502	4504	4263	4562	4533
h_0 (MJ/kg)	8.36	7.37	9.27	9.05	9.37	7.90	9.34	9.17
T_∞ (K)	2186	2070	2335	2319	2323	2156	2353	2342
P_∞(KPa)	45.5	47.2	42.4	44.5	44.9	43.5	44.6	46.5
$\rho_\infty(kg/m^3)$	.0102	.0114	.0858	.0915	.0921	.0993	.0895	.0942
u_∞(m/s)	3195	3106	3352	3325	3325	3171	3363	3340
M_∞	4.44	4.45	4.44	4.44	4.433	4.43	4.44	4.43
$[O]$	.0041	.0013	.0125	.0106	.0107	.0034	.0129	.0114
$[CO2]$	.7829	.8302	.6911	.7102	.7093	.7892	.6893	.7036
$[CO]$	.1434	.1128	.2018	.1897	.1903	.1394	.2029	.1938
$[O2]$	.0697	.0557	.0946	.0896	.0898	.0680	.0950	.0912

Table D.6: Data summary for condition CO_2 3.

Shot Number	1662	1663	1664	1665	1666	1667	1669	1898
diameter (cm)	2	2	2	2	2	2	2	8
angle(degrees)	75	63	60	70	66	56	56	55
P_{2R}(psig)	1425	1425	1425	1425	1425	1425	1425	1425
P_{CT} (KPa)	124	124	124	124	124	124	124	124
% He	86	86	86	86	86	86	86	86
P_{ST} (KPa)	60	60	60	60	60	60	60	60
dia. (in/in)	248/190	248/190	248/190	248/192	248/192	248/192	250/193	248/190
P_{4N} (MPa)	105.3	105.1	104.8	104.6	104.1	105.9	97.5	108
P_{4S} (MPa)	94.1	98.8	99.1	98.9	99.1	100.7	93.8	111
T_{amb} (K)	297	297	299	297	296	297	297	298
u_s (m/s)	3158	3125	3158	3158	3158	3409	3681	3130
P_{0N} (MPa)	63.9	62.2	64.6	64.0	67.3	68.1	63.7	63.3
P_{0S} (MPa)	63.4	62.9	64.7	64.5	66.5	68.0	64.3	66.2
P_{0a} (MPa)	63.6	62.5	64.6	64.2	66.9	68.1	64.0	64.8
t_{fire} (ms)	.9	.9	.9	.9	.9	.9	.9	1.0
t_{del} (ms)								
t_{Kazu} (ms)	.9	.9	.9	.9	.9	.9	.9	.15
d_{epl} (cm)	15.0	14.6	14.6	14.9	14.7	14.6	14.6	.85
δ/d	-	0.0	0.0	.105	.0241	-	-	.1
T_O (K)	4517	4470	4527	4521	4540	4856	5170	.00297
h_0 (MJ/kg)	9.13	8.92	9.16	9.14	9.19	10.7	12.2	4490
T_∞ (K)	2328	2301	2337	2331	2346	2497	2493	9.23
P_∞(KPa)	44.4	43.9	45.4	44.9	47.0	47.4	30.3	2493
$\rho_\infty(kg/m^3)$	.0906	.0912	.0923	.0915	.0952	.0863	.0522	30.3
u_∞(m/s)	3335	3305	3338	3336	3344	3539	3697	.0522
M_∞	4.43	4.43	4.43	4.43	4.43	4.45	4.51	3697
$[O]$	.0112	.974e-2	.0114	.0113	.0114	.0247	.0481	
$[CO2]$	.7040	.7178	.7026	.7039	.7031	.6015	.4820	.0481
$[CO]$	.1936	.1849	.1945	.1937	.1941	.2575	.3293	.4820
$[O2]$	.0912	.0876	.0915	.0920	.0913	.1164	.1406	.3293

Data summary for condition CO_2 3 (cont. 2/4)

Shot Number	1899	1900	1901	1902	1941	1942	1943	1944
diameter (cm)	8	8	8	8	16	16	16	16
angle(degrees)	58	70	61	75	66	63	56	60
P_{2R}(psig)	1425	1425	1425	1425	1425	1425	1425	1425
P_{CT} (KPa)	124	124	124	124	124	124	124	124
% He	86	86	86	86	86	86	86	86
P_{ST} (KPa)	60	60	60	60	60	60	60	60
dia. (in/in)	250/190	249/193	249/193	248/193	247/198	247/199	247/201	247/201
P_{4N} (MPa)	104	107	108	106	124	123	123	124
P_{4S} (MPa)	103	106	109	106	111	113	112	113
T_{amb} (K)	297	300	300	300.5	296.5	298	297	297.5
u_s (m/s)	3030	3130	3170	3130	3080	3060	3110	3130
P_{0N} (MPa)	61.7	63.5	64.8	64.4	62.9	65.6	64.6	65.3
P_{0S} (MPa)	64.5	66.5	68.0	66.8	60.2	62.8	61.2	62.3
P_{0a} (MPa)	63.1	65.0	66.4	65.6	61.6	64.2	62.9	63.8
t_{fire} (ms)	1.0	1.0	1.0	1.0	.95	.96	.97	.97
t_{del} (ms)								
t_{Kazu} (ms)	.15	.1	.15	.15	.2	.2	.2	.2
d_{epl} (cm)	.94	.79	.75	.8	.79	.79	.78	.77
δ/d	.1	.1	.1	.1	.1	.1	.1	.1
T_O (K)	.00340	.0221	.0064	.0572	.00184	0.0	.00191	0.0
h_0 (MJ/kg)	4360	4490	4560	4500	4410	4410	4450	4480
T_∞ (K)	8.71	9.24	9.52	9.25	8.92	8.89	9.11	9.21
P_∞(KPa)	1836	2968	2964	2914	2964	2914	2328	2301
$\rho_\infty(kg/m^3)$	22.7	25.0	25.5	24.9	25.5	24.9	44.4	43.9
u_∞(m/s)	.0416	.0278	.0284	.0283	.0284	.0283	.0906	.0912
M_∞	4734	5480	5478	5447	5478	5447	3335	3305
$[O]$	.9972	.9616	.9628	.9650	.9628	.9650		
$[CO2]$							.0112	.974e-2
$[CO]$							.7040	.7178
$[O2]$							.1936	.1849

Data summary for condition CO_2 3 (cont. 3/4)

Shot Number	1945	1946	1948	1950
diameter (cm)	16	16	8	8
angle(degrees)	70	75	70	75
P_{2R}(psig)	1425	1425	1425	1425
P_{CT} (KPa)	124	124	124	124
% He	86	86	86	86
P_{ST} (KPa)	60	60	60	60
dia. (in/in)	247/201	247/202	247/205	247/204
P_{4N} (MPa)	123	124	123	124
P_{4S} (MPa)	112	112	113	113
T_{amb} (K)	296	297	297	297
u_s (m/s)	3090	3090	3140	3130
P_{0N} (MPa)	66.5	68.8	67.7	67.9
P_{0S} (MPa)	63.5	65.0	63.7	63.6
P_{0a} (MPa)	65.0	66.9	65.7	65.7
t_{fire} (ms)	.98	.98	.97	.96
t_{del} (ms)				
t_{Kazu} (ms)	.2	.2	.18	.18
d_{epl} (cm)	.78	.78	.76	.77
δ/d	.1	.1	.1	.1
T_O (K)	.0184	.0461	.0264	.0680
h_0 (MJ/kg)	4450	4460	4510	4490
T_∞ (K)	9.06	9.09	9.32	9.24
P_∞(KPa)	2337	2331	2497	2493
$\rho_\infty(kg/m^3)$	45.4	44.9	47.4	30.3
u_∞(m/s)	.0923	.0915	.0863	.0522
M_∞	3338	3336	3539	3697
$[O]$				
$[CO2]$	.0114	.0113	.0247	.0481
$[CO]$	.7026	.7039	.6015	.4820
$[O2]$	.1945	.1937	.2575	.3293

Data summary for condition CO_2 3 (cont. 4/4)

Bibliography

ADAM P.H. (1997) *Enthalpy effects on hypervelocity boundary layers.* Ph.D. thesis, California Institute of Technology.

ANDERSON J.D. (1989) *Hypersonic and high temperature gas dynamics.* McGraw-Hill.

ANDERSON J.D. (1990) *Modern compressible flow with historical perspective.* McGraw-Hill.

ASTM (1993) *Manual on the use of thermocouples in temperature Measurement*, 4th edition.

BLOTTNER F.G., JOHNSON M., and ELLIS M. (1971) Chemically reacting visocus flow program for multi-component gas mixtures. Sandia Laboratories, Albuquerque, New Mexico SC-RR-70-754.

BUSEMANN A. (1929) Drücke auf kegelförmige Spitzen bei Bewegung mit Überschallgeschwingdigkeit. *Z. Angew Math. Mech.*, 9(6):496–498.

CANDLER G. (1988) *The computation of weakly ionized hypersonic flows in thermo-chemical nonequilibrium.* Ph.D. thesis, Stanford University.

CANDLER G.V. and MACCORMACK R.W. (1991) Computation of weakly ionized hypersonic flows in thermochemical nonequilibrium. *Journal of Thermophysics and Heat Transfer*, 5(3):266–273.

DAVIES L. and WILSON J.L. (1969) Influence of reflected shock and boundary-layer interaction on shock-tube flows. *The Physics of Fluids*, 12(5):37–43.

DAVIS J. (1998) *High-Enthalpy Shock/Boundary-Layer Interaction on a Double Wedge.* Ph.D. thesis, California Institute of Technology.

DORRANCE W.H. (1962) *Viscous Hypersonic Flow.* McGraw-Hill.

DROUGGE G. (1948) The flow around conical tips in the upper transonic range. The Aeronautical Research Institute of Sweden Report 25.

GUPTA R.G., YOS J.M., THOMPSON R.A., and LEE K. (1990) A review of the reaction rates and thermodynamic transport properties for an 11-species air model for chemical and thermal nonoequilibrium calculations to 30000 K. NASA RP -1232.

HEBERLE J.W., WOOD G.P., and GOODERUM P.B. (1949) Data on shape and location of detached shock waves. NACA TN 2000.

HORNUNG H. (1996) Hypersonic aerodynamics class notes. Galcit, caltech.

HORNUNG H. and BELANGER J. (1990) Role and techniques of ground testing for simulation of flows up to orbital speed. AIAA Paper 90-1377. (16th Aerodynamic Ground Testing Conference, Jun 18-20, Seattle, WA, USA.

HORNUNG H.G. and HOUWING A.F.P. (1980) Shock detachment from cones in a relaxing gas. *Journal of Fluid Mechanics*, 101:307–319.

HORNUNG H.G. and SMITH G.H. (1979) The influence of relaxation on shock detachment. *Journal of Fluid Mechanics*, 93:225–239.

JOHNSTON G.W. (1952) An investigation of the flow about cones and wedges at and beyond the critical angle. UTIA 24.

KAATTARI G.E. (1963) Shock envelopes of blunt bodies at large angles of attack. NASA TN D1980.

LEE J.H. (1985) Basic governing equations for the light regimes of aeroassisted orbital transfer vehicles. *Progress in Aeronautics and Astronautics: Thermal Design of Aeroassisted Orbital Transfer Vehicles*, 96:3–53. edited by H. F. Nelson.

LEMIEUX P. (1999) *The Instability of Shear Layers Produced by Curved Shocks*. Ph.D. thesis, California Institute of Technology.

LORDI J.A., MATES R.E., and MOSELLE J.R. (1966) Computer program for solution of nonequilibrium expansions of reacting gas mixtures. NASA CR 472.

MACCOLL J.W. (1937) The conical shock wave formed by a cone moving at a high speed. *Proc. Roy. Soc. (London)*, 159(898):459–472.

MALLINSON S.G., GAI S.L., and MUDFORD N.R. (1996) The boundary layer on a flat plate in hypervelocity flow. *Aeronautical Journal*, 100(994):135–141.

MARRONE P.V. and TREANOR C.E. (1963) Chemical relaxation with preferential dissociation from excited vibrational levels. *The Physics of Fluids*, 6(9):1215–1221.

MCINTOSH M.K. (1970) A computer program for the numerical calculation of equilibrium and perfect gas conditions in shock tunnels. Australian Defense Scientific Service TN CPD 169. Salisbury, South Australia.

MERZKIRCH W. (1987) *Flow Visualization*. Academic Press.

MOECKEL W.E. (1949) Approximate method for predicting form and location of detached shock waves ahead of plane or axially symmetric bodies. NACA TN 1921.

MOECKEL W.E. (1950) Experimental investigation of supersonic flow with detached shock waves for mach numbers between 1.8 and 2.9. NACA RM E50D05.

OLEJNICZAK J. (1997) *Computational and Experimental Study of Nonequilibrium Chemistry in Hypersonic Flows*. Ph.D. thesis, University of Minnesota.

PARK C. (1985) On convergence of computations of chemically reacting flows. AIAA Paper 85-0247.

PARK C. (1987) Assesment of a two-temperature kinetic model for dissociating a weakly ionizing nitrogen. *Journal of Thermophysics*, 2(1):8–16.

PARK C., HOWE J.T., JAFFE R.L., and CANDLER G.V. (1994) Review of chemical-kinetic problems for future nasa missions, ii: Mars entries. *AIAA Journal of Thermophysics and Heat Transfer*, 8(1).

PRESS W.H., TEUKOLSKY S.A., VETTERLING W.T., and FLANNERY B.P. (1992) *Numerical Recipes in FORTRAN: The Art of Scientific Computing*. Cambridge University Press, 2nd edition.

QUIRK J. (1998) Amrita — a computational facility (for cfd modelling). von Karman Institute 29th CFD Lecture Series ISSN 0377-8312.

REIN M. (1989) Surf: A program for calculating inviscid supersonic reacting flows in nozzles. California Institute of Technology GALCIT FM 89-1.

REYNOLDS W.C. (1986) The element potential method for chemical equilibrium analysis: implementation in the interactive program stanjan. Stanford University Department of Mechanical Engineering Report.

SANDERSON S.R. (1995) *Shock Wave Interaction in Hypervelocity Flow*. Ph.D. thesis, California Institute of Technology.

SMEETS G. (1990) Interferometry. von Karman Institute Lecture Series 05.

SOLOMON G.E. (1954) Transonic flow past cone cylinders. NACA TN 3213.

SPURK J.H. (1966) Interferometric measurement of the nonequilibrium flow field around a cone. *The Physics of Fluids*, 9(7):1278–1285.

SPURK J.H. (1970) Experimental and numerical nonequilibrium flow studies. *AIAA Journal*, 8(6):1039–1045.

STAFF A.R. (1948) Equations, tables, and charts for compressible flow. NACA R 1135.

STEWARTSON K. (1964) *The Theory of Laminar Boundary Layers in Compressible Fluids*. Oxford University Press.

SUDANI N. and HORNUNG H.G. (1997) Detection and reduction of driver gas contamination in a high-enthalpy shock tunnel. In *Proceedings of the 21st International Symposium on Shock Waves*. Fyshwick, Australia: Panther Publishing and Printing. (Jul 20–25, Great Keppel, Australia).

SUDANI N., VALIFERDOWSI B., and HORNUNG H.G. (1998) Test time increase by delaying driver gas contamination for reflected shock tunnels. AIAA Paper 98-2771. (20th Advanced Measurement and Ground Testing Technology Conference, Jun 15-18, Albuquerque, NM, USA).

TAYLOR G.I. and MACCOLL J.W. (1933) The air pressure over a cone moving at high speeds. *Proc. Roy. Soc. (London)*, 139(838):278–311.

TREANOR C.E. and MARRONE P.V. (1962) Effect of dissociation on the rate of vibrational relaxation. *The physics of fluids*, 5(9):1022–1026.

VINCENTI W.G. and KRUGER C.H. (1975) *Introduction to Physical Gas Dynamics*. Krieger Publishing.

WARD C. and PUGH P.G. (1968) Shock standoff distances of blunt and sharp cones. *AIAA Journal*, 6(10):2018–2019.

WEN C. (1994) *Hypervelocity flow over spheres*. Ph.D. thesis, California Institute of Technology.

WEN C.Y. and HORNUNG H.G. (1995) Non-equilibrium dissociating flow over spheres. *Journal of Fluid Mechanics*, 299:389–405.

WHITE F.M. (1991) *Viscous Fluid Flow*. McGraw-Hill, 2nd edition.

YOSHIHARA H. (1952) On the flow over a cone-cylinder body at mach number one. WADC TR 52-295.